

**Study on Ni/Cu Alloy Plating and Pure Nickel**

**Electrodeposition in Magnetic Fields**

by

Tianfei Wang

A thesis submitted in partial fulfillment of the requirements for the degree of

Doctor of Philosophy

in

Materials Engineering

Department of Chemical and Materials Engineering

University of Alberta

© Tianfei Wang 2015

## **Abstract**

The processes of Ni/Cu electro-co-deposition and pure nickel electroplating in magnetic field have been investigated. Various techniques such as scanning electron microscope (SEM), atomic force microscope (AFM), X-ray diffractometer (XRD), and electrochemical characterization were used to determine the characteristics of electro-deposition. A reliable method has been developed to fabricate Ni/Cu coating film with uniform composition. The color of Ni/Cu deposits was found to be related to the residual stresses in the deposits, which could be altered by adjusting the pH level of the solution. The magneto-electrolytic deposition study found that MHD stirring in the bulk electrolyte has limited influence on the coating properties; however, MHD effect in the fluid boundary layer could modify the morphology and structure of the deposits. Three new models were proposed to interpret the underlying mechanisms on morphology and texture formation during nickel deposit in both parallel and vertical magnetic fields. The effect of the alternative magnetic field generated by spinning magnets on nickel deposition was also investigated and the coatings with better surface smoothness than static magnetic field had been achieved. The micro-hardness of the deposited nickel samples made in the absence and presence of magnetic field were evaluated. The hardness of the deposits can be well correlated to the surface roughness through a Hall-Petch-type relationship.

## Acknowledgements

First and foremost, I would like to acknowledge my supervisor, Prof. Weixing Chen, for his non-stop guidance, support, and inspiration throughout my doctoral research work. I am impressed by his enthusiasm and diligence in research, and his knowledge in various aspects of materials science and research methods. The six years that I spent conducting research under his supervision have provided me with the most valuable experience in my life.

I am grateful to all my colleagues Dr. Xinwei Cui, Dr. Yongwang Kang, Dr. Fengping Hu, Dr. Hao Li, Dr. Ziqiang Dong, Dr. Abdoulmajid Eslami, Dr. Afolabi Egbewande, Dr. Donghai Lin, Mr. Mingwen Gao, Mr. Xiaotian Zhang, Mr. Mengshan Yu and Ms. Renfei Wang for their kind help with my work.

I would also like to thank the technical contributions from Shiraz Merali, Steve Launspach (XRD), Tina Barker, De-ann Rollings, George Braybrook, Nathan Gerein, Gayle Hatchard (SEM/EDX), Dr. Anqiang He (AFM), and Dr. Shenghui Wang (Nanoindenter).

Finally, I would like to acknowledge the financial support from the Natural Science and Engineering Research Council of Canada (NSERC) and the Royal Canadian Mint.

## Table of Contents

Chapter 1 Introduction and Literature Review .....	1
1.1 Introduction .....	2
1.2 Objectives.....	4
1.3 Electrodeposition .....	5
1.4 Ni/Cu Codeposition .....	6
1.4.1 Overview.....	6
1.4.2 Complexing agent .....	7
1.4.3 Solution chemistry of the citrate bath.....	7
1.4.4 Codeposition mechanism in citrate bath.....	9
1.4.5 Electrochemical behaviour in Ni/Cu co-deposition bath .....	14
1.4.6 Bath stability .....	16
1.5 Electrodeposition in magnetic field.....	17
1.5.1 Overview.....	17
1.5.2 Fundamentals of magneto-electrolytic deposition (MED).....	18
1.5.3. Magnetic field effect on electrolyte properties.....	22
1.5.4. Magnetic field effect on mass transport.....	24
1.5.5 Cathodic deposit morphology effects of the magnetic field .....	27
1.5.6 Proposed mechanisms of the deposit morphology change in magnetic field.....	31
1.5.7 Structure change of electrodeposition in the magnetic field .....	39
1.6 References.....	46
Chapter 2 Experimental.....	55
2.1 Ni-Cu Codeposition.....	56
2.1.1 Experimental setup and electrolytes.....	56
2.1.2 Sample preparation .....	57
2.1.3 Experimental procedures .....	58
2.1.4 Characterization.....	59
2.2 Nickel plating in constant magnetic field.....	59
2.2.1 Experimental setup and electrolyte .....	59
2.2.2 Sample preparation .....	61

2.2.3 Experimental procedures .....	61
2.2.4 Characterization .....	62
2.3 Nickel plating in rotating magnetic field generated by spinning magnets .....	62
2.4 Microhardness investigation of nickel electrodeposition in magnetic field .....	64
2.5 Material characterization techniques .....	64
2.5.1 Scanning electron microscope (SEM).....	64
2.5.2 Energy dispersive X-ray spectroscopy (EDX) .....	65
2.5.3 X-ray diffraction (XRD) .....	66
2.5.4 Atomic force microscope (AFM).....	69
2.6 References .....	70
Chapter 3 Composition and Colour Control of Nickel-Copper Electro-Co-deposition in Citrate Bath .....	72
3.1 Introduction .....	73
3.2. Experimental.....	75
3.3 Results and discussion .....	77
3.3.1 Control of Ni/Cu codeposition parameters in citrate bath .....	77
3.3.2 The composition control of the Ni-Cu codeposition .....	85
3.3.3 A novel method to control Cu content in Ni/Cu citrate plating bath .....	96
3.3.4 Color control of the Ni/Cu coating .....	100
3.4. Conclusions .....	109
3.5 References .....	111
Chapter 4 Mechanistic investigation of the magnetic field effects on nickel electro-deposition.....	114
4.1 Introduction .....	115
4.2 Experimental.....	117
4.3 Results and discussion .....	119
4.3.1 Characterization results .....	119
4.3.2 The mechanisms on the morphological change during deposition in magnetic fields .....	125
4.3.3 The Mechanism on the nickel texture formation under the influence of magnetic field .....	137
4.4 Conclusions .....	142
4.5 References .....	144
Chapter 5 Effects of rotating magnetic fields on nickel electro-deposition .....	148
5.1. Introduction .....	149
5.2. Experimental.....	151

5.2.1. Electrolysis system.....	151
5.2.2. Electro-deposition in the presence of an external magnetic field .....	151
5.2.3. Characterization of the nickel deposition.....	153
5.3 Results and discussion .....	153
5.3.1 Magnetic and electric fields in spinning magnets .....	153
5.3.2 Electrochemical characterization .....	156
5.3.3 Morphological examination by SEM and AFM .....	157
5.3.4 Structural investigation by XRD.....	166
5.3.5 About the outstanding results at $f=1500$ and $3000$ rpm.....	170
5.4 Conclusions .....	170
5.5 References.....	172
Chapter 6 Microhardness investigation of nickel electrodeposition in magnetic field .....	175
6.1 Introduction .....	176
6.2 Experimental.....	179
6.3 Results and discussion .....	180
6.3.1 Micro-hardness test result .....	180
6.3.2 Effect of grain size on micro-hardness.....	181
6.3.3 Effect of morphology on micro-hardness .....	184
6.3.4 Effect of crystal texture on micro-hardness .....	187
6.3.5 Identifying the dominant reason for coating strengthening .....	189
6.4 Conclusions .....	191
6.5 References.....	192
Chapter 7 Conclusions and Future Work Recommendations .....	195
7.1 Conclusions .....	196
7.1.1 Electrodeposition of Ni/Cu alloy .....	196
7.1.2 Modeling on the mechanism of the morphological and structural change of magneto-electrolytic deposition.....	197
7.1.3 Rotating magnetic field effects on nickel electrodeposition .....	199
7.1.4 Magnetic field effect on the microhardness of nickel deposit.....	200
7.2 Future work recommendations .....	200
7.2.1 Nickel-copper codeposition .....	200
7.2.2 magneto-electrolytic deposition.....	201

7.3 References.....	202
Bibliography .....	203

## List of Tables

Table 3-1 The copper content in coatings at different conditions .....	94
Table 3-2 Data from XRD patterns of Ni/Cu coating films obtained at different pH levels .....	105
Table 3-3 Calculation of the residual stress of Ni/Cu samples .....	107
Table 4-1 Parameters for calculating the body force of the field gradient on surface adatoms in equation (4-3) .....	131
Table 5-1 Surface Roughness Test Result with AFM .....	159
Table 6-1 Grain size values of the coatings from different conditions.....	181

## List of Figures

Figure 1-1 Distribution of the nickel-citrate species with the solution pH in a nickel-copper citrate solution (Fig. 5 in Ref. 19). .....	12
Figure 1-2 Distribution of the copper-citrate species with the solution pH in a nickel-copper citrate solution (Fig. 4 in Ref. 19). .....	13
Figure 1-3 Steady-state partial copper current curves in a copper-citrate bath and in a copper-nickel citrate bath at different pH values (Fig. 6 in Ref. 19). .....	14
Figure 1-4 Steady-state partial nickel current curves in a nickel-citrate bath and in a copper-nickel citrate bath at different pH values (Fig. 7 in Ref. 19). .....	15
Figure 1-5 Dependence of limiting current on magnetic field intensity (Fig. 2 in Ref. 44). .....	25
Figure 1-6 SEM micrographs and corresponding AFM images with line section analysis of layers deposited without magnetic field (a, d and g), in parallel (b, e and h) and perpendicular-to-electrode (c, f and i) configurations ( $B = 1$ T) (Fig. 4 in Ref. 46). .....	28
Figure 1-7 SEM images of copper deposited with (a) no magnetic field and (b) a parallel field of 0.5 T (Fig. 14 in Ref. 46). .....	29
Figure 1-8 AFM images of the layers of deposited NiFe alloy in the magnetic field of (A) 0 T, (B) 0.615 T, parallel (Fig. 11 in Ref. 89). .....	30
Figure 1-9 AFM images of the iron films electrodeposited in the parallel magnetic fields of (a) 0 T, (b) 0.5 T, (c) 1 T, (d) 3 T and (e) 5 T (Fig. 1 in Ref. 87). .....	30
Figure 1-10 TEM images of the cross-sections of deposited CoFe layers without (a), in parallel (b) and perpendicular (c) magnetic fields ( $B = 1$ T) (Fig. 5 in Ref. 84). .....	31

Figure 1-11 SEM cross section view of the deposited Fe layers in (a): 0T, (b) 1T, parallel and (c) 1T, perpendicular magnetic fields ( Fig. 14 in Ref. 88). ..... 31

Figure 1-12 Morphological difference between the hydrogen bubble pit on the nickel deposit surface in the (a) absence and (b) presence of the parallel magnetic field (Fig. 7 and 8 in Ref. 92). ..... 33

Figure 1-13 Schematic presentation of the formation mechanism of the morphology around a hydrogen pit in the parallel magnetic field (Fig. 10 in Ref. 92). ..... 34

Figure 1-14 Electrodeposited Fe grown in a thin cell under (a) no magnetic field and (b) a parallel magnetic field of 0.2T (Fig. 1 in Ref. 97). ..... 36

Figure 1-15 Illustration of (a) micro-MHD effect in corrosion (Fig. 4 in Ref. 99) and (b) vertical MHD effect in electrodeposition (Fig. 1 in Ref. 101). ..... 37

Figure 1-16 SEM image of Cu deposited in the vertical magnetic field of 7T, showing the “micro-mystery circles” (Reproduced from Ref. 99). ..... 38

Figure 1-17 SEM images of the Ni deposited in a magnetic field arranged at a 45° angle: (a) no field; (b) in the 1 T magnetic field; (c) higher magnification view of (b) (Fig. 2 in Ref. 48). ..... 39

Figure 1-18 Schematic view of the equilibrium of two neighbouring grains with different surface energies (Fig. 4 in Ref. 108). ..... 43

Figure 1-19 SEM image of the cross section of Fe deposit showing the coverage of grain 1 (Fig. 3 in Ref. 108). ..... 44

Figure 2-1 Experimental setup for (a) beaker plating, (b) barrel plating and (c) barrel plating device. .... 57

Figure 2-2 Schematic diagram of the electrolysis system in the presence of the magnetic field. 60

Figure 2-3 Schematic diagram of the electrolysis system in the alternating magnetic field generated from spinning magnets. ....	63
Figure 2-4 Illustration of the characteristic X-ray generation process (Fig 6.5 in Ref. 1).....	66
Figure 2-5 Graphic presentation of an XRD <sup>2</sup> system (Fig. 3 in Ref. 3). ....	67
Figure 2-6 Diffraction geometry of conventional XRD and XRD <sup>2</sup> (Fig. 3 in Ref. 4). ....	68
Figure 2-7 2D XRD diffraction pattern. ....	68
Figure 2-8 Illustration of the operation principle of the MFP-3D atomic force microscope (Fig. 5.2A in Ref. 5).....	70
Figure 3-1 Experimental setup for (a) beaker plating, (b) barrel plating, and (c) photo of barrel plating device. ....	75
Figure 3-3 Titration curves of 100ml Ni/Cu codeposition bath with different citrate concentrations and titrated with 0.01M H <sub>2</sub> SO <sub>4</sub> at 40°C.....	83
Figure 3-4 Solubility of complex precipitate Cu <sub>2</sub> H <sub>1</sub> Cit•2H <sub>2</sub> O in the electrolyte for barrel plating at different temperatures. ....	85
Figure 3-5 Back Scatter Electron (BSE) image of the cross section of the nickel-copper alloy coating.....	85
Figure 3-6 X-ray line scanning result along the cross sections of the Ni-Cu coatings in three different beaker setup plating tests with different initial copper sulphate concentrations in the bath (a) 0.0056M, (b) 0.0080M, (c) 0.0104M. ....	87
Figure 3-7 Relationship between coating composition and copper anode current ratio at different conditions in beaker setup plating experiments. ....	93
Figure 3-8 The variation of free copper ion concentration in the bath and the copper content in the coating during Ni/Cu plating in which the service time ratio of the Cu anode and Ni anode	

was 0.3. (a) the potential change of the electrode for free copper ion measurement, 112.5mV and 135.8mV correspond to  $\text{Cu}^{2+}$  concentrations of  $10^{-6}\text{M}$  and  $10^{-5}\text{M}$ , respectively. The relationship between the potential  $E$  and  $\text{Cu}^{2+}$  concentration is:  $\log [\text{Cu}^{2+}] = (E - 252.3)/23.3$  (b) Variation of copper content with the coating thickness of the Ni/Cu plating layer. .... 96

Figure 3-9 Cyclic voltammogram obtained on the copper surface in Ni/Cu citrate plating bath. 97

Figure 3-10 Potential distribution on a  $15 \times 30$  mm copper plate surface in the Ni/Cu citrate bath during electroplating. The potential values are vs SCE. (a): before electroplating, the copper plate is equipotential with a potential of -65.6 mV vs SCE. (b) when copper anode is disconnected from the power supply, a small potential difference occurred across the Cu surface. .... 98

Figure 3-11 EDX measurement result of composition distribution of two Ni/Cu samples deposited in citrate bath at pH levels of (a) 4.5 and (b) 5.1. The numbers inside the squares are Cu weight percent values. .... 101

Figure 3-12 3-12 Photo of Ni/Cu samples deposited in the citrate bath at pH levels of (a) 4.5 and (b) 5.1. For comparison, pure copper and pure nickel samples are also presented in (c) and (d). .... 101

Figure 3-13 EDX line scan result of the cross sections of two Ni/Cu samples electroplated in the citrate bath at pH levels of (a) 4.5 and (b) 5.1. .... 102

Figure 3-14 Comparison of surface morphologies of Ni/Cu coating samples fabricated at pH levels of (a) 4.5 and (b) 5.1. .... 103

Figure 3-15 patterns of Ni/Cu coating films obtained at pH 4.5 and 5.1 in the citrate bath. .... 105

Figure 3-16  $d\text{-sin}^2\psi$  curves and data fitting of XRD2 results for Ni/Cu samples. .... 107

Figure 4-1 Schematic diagram of the electrolysis system in the presence of the magnetic field. .... 118

Figure 4-2 SEM images of deposited nickel morphology in sulphate bath under various magnetic field conditions: (a) B=0; (b) B=0.18T, parallel; (c) B=0.18T, vertical; and (d) B=0 with mechanical vibration. ....	120
Figure 4-3 XRD spectra of nickel deposited in a sulphate bath under different magnetic field situations. The intensity of (111) peak has been set to 100. All the unmarked peaks are from the Cu substrate. ....	121
Figure 4-4 XRD peaks intensity comparison diagram for various experimental conditions. ....	121
Figure 4-5 Chronopotentiometry curves during Ni deposition in different experimental conditions. ....	123
Figure 4-6 Illustration of the migration route of the Ni ions from the anode to the cathode in the cell. ....	124
Figure 4-7 Schematics representing the mechanism of the parallel magnetic field affecting the deposit morphology. ....	127
Figure 4-8 Illustration of the morphological variations of the deposit in parallel magnetic field under different flow patterns. ....	128
Figure 4-9 Illustration showing the two mechanisms explaining the morphology formation during plating in the vertical magnetic field. ....	134
Figure 4-10 Schematic of the soft magnetic material deposited in vertical magnetic field and the resultant columnar morphology. ....	136
Figure 4-11 SEM images showing nickel deposition in the parallel and vertical magnetic fields for 100 seconds. ....	138
Figure 4-12 AFM observation of the nickel deposit surface in various magnetic field conditions for 50 seconds. ....	140

Figure 4-13 STM image of a Ni(111) island. (Fig. 2(A) in Ref.43) .....	140
Figure 4-14 Schematic illustration of the magnetic field changing the nickel crystal texture through levelling the pyramidal island on the deposit surface. ....	142
Figure 5-1 Schematic diagram of the electrolysis system in the alternating magnetic field generated from spinning magnets. ....	152
Figure 5-2 Schematic of the changing magnetic field and the induced eddy electric field produced by the spinning magnets. (a) the overall view; (b) the side view. ....	154
Figure 5-3 The spinning magnetic field and the induced eddy electric field around the sample. B is (a) parallel to; (b) perpendicular to; (c) oblique crossing the sample surface. ....	155
Figure 5-4 Schematic presentation of the changing process of the surface component, $E_s$ , of the induced electric field : (a) B is parallel to the electrode; (b) B is oblique over the electrode; and (c) B is perpendicular to the electrode. ....	156
Figure 5-5 Chronopotentiometry curves during Ni deposition under different magnetic field conditions. ....	157
Figure 5-6 SEM images of deposited nickel morphology in the nickel sulphate bath under various magnetic field conditions: absence, static field and spinning magnet at different rates. ....	158
Figure 5-7 AFM images of the detailed features of the nickel deposit surfaces in different conditions. ....	160
Figure 5-8 Illustration of the mechanism of the induced electric field leveling a grain: (a) different influences on various parts of the grain; and (b) the resultant growth. ....	162
Figure 5-9 AFM image of Ni coating surface under the magnetic field that is spinning at 3000rpm. ....	163

Figure 5-10 Schematic presentation of the surface components of the magnetic field and the induced electric field. ....	163
Figure 5-11 XRD spectra of nickel deposited in the nickel sulphate bath under different magnetic field situations. The intensity of (111) peak has been set to 100. All the unmarked peaks are from the Cu substrate. ....	167
Figure 5-12 XRD peak intensities (proportion to 111 peak) of 200, 220 and 311 peaks obtained in the experiments. ....	168
Figure 6-1 Vickers hardness of the deposited nickel in various magnetic field conditions. ....	180
Figure 6-2 The variations of microhardness and grain size of the coating with experimental conditions. ....	182
Figure 6-3 Variations of microhardness with $d^{-1/2}$ ( $d$ is the grain size). ....	182
Figure 6-4 SEM images of deposited nickel morphology in the nickel sulphate bath under various magnetic field conditions: absence, static field and spinning magnet at different rates. ....	185
Figure 6-5 AFM images of the detailed features of the nickel deposit surfaces under different conditions. The scanning range is $10 \times 10 \mu\text{m}$ . Due to the coarse surface of the coatings at $B=0$ and $B=0.18\text{T}$ , $f=1500$ rpm, no clear image is available for these two conditions. ....	186
Figure 6-6 Schematic diagram of correlation of coating hardness with surface roughness measurement values. (a): RMS and hardness change with the operation conditions; (b) the trend of hardness varies with RMS. ....	187
Figure 6-7 Texture coefficients of the nickel deposits from different magnetic field conditions. ....	188

Figure 6-8 Comparison of microhardness and (200) texture coefficient (Tc 200). (a): hardness and Tc 200 change with the operation conditions; (b) the trend of hardness varies with Tc 200.

..... 189

Figure 6-9 Schematic diagram of the relationship between microhardness and the inverse square root of RMS. .... 191

## **Chapter 1 Introduction and Literature Review**

## 1.1 Introduction

The present research was initiated for the purpose of developing Ni- and Ni/Cu-based electrodepositions for Canadian coins with improved performance and security. In particular, attention has been paid to developing Ni/Cu alloy coatings that have high Cu content but retain the color of Ni metal, and to exploring new approaches that could improve morphological and mechanical properties of electrodeposits. In this investigation, citrate was selected as the complexing agent due to its eminent characteristics. The electrodeposition process of Ni/Cu alloy plating in a citrate bath was thoroughly examined in order to elucidate mechanisms of electrodeposition under the special conditions being investigated.

Based on the results of the literature review, the effect of the magnetic field on electrodeposition aroused the author's interest to explore its underlying mechanisms and to work out some novel techniques that could lead to improved coating characteristics. To achieve this, the process of Ni-plating was conducted in the presence of static and rotating magnetic fields. The coatings obtained under varied magnetic conditions were extensively characterized using various techniques including SEM/EDX, XRD, AFM, electrochemical characterization, and microhardness testing. The unique characteristics of the coatings were rationalized on the basis of the magnetohydrodynamic (MHD) effect.

The thesis is composed of seven chapters. In Chapter 1, after a brief introduction to the thesis, a detailed literature review will provide an overview of the latest progress achieved in the field of Ni/Cu alloy plating and electrodeposition in magnetic fields. Various techniques to control the coating composition and bath chemistries ensuring the sustainability of the codeposition have been critically reviewed. The chapter introduces potential options to adjust the coating color, and discusses, extensively, the effect of the magnetic field on nickel electrodeposition.

Chapter 2 provides a brief summary of various experimental and analytical approaches/methodologies involved in the investigation. It includes the description of an innovative electrochemical setup that makes it possible to apply rotating magnetic fields during electrodeposition.

Chapter 3 identifies various engineering challenges in the deposition of Ni/Cu alloy coatings. These challenges include the bath instability, composition control and coating color adjustment. Solutions for solving the above challenges were developed. The plating bath was stabilized by the appropriate choice of the electrolyte ingredients, solution pH and deposition temperature; the uniformity of the coating composition was achieved by employing two anodes and correctly determining their areas, and keeping the bath pH stable; the coating color was adjusted by varying the electrolyte pH, which, according to the experimental results of this research, affected the residual stress and optical properties of the deposition.

The investigation on the electrodeposition in the presence of static magnet fields was reported in Chapter 4. It has been found that the MHD convection in the fluid boundary layer plays the dominant role in modifying the morphology and crystal texture of the deposit. Two new models were established for the static parallel and vertical magnetic fields, respectively, to elucidate the MHD effect in the boundary layer. The two models are able to rationalize the leveling effect of the magnetic field in electrodeposition, and the formation of elongated and columnar grains of soft magnetic materials deposited in parallel and vertical magnetic fields, respectively. Based on the AFM characterization of the surface morphology during the nucleation stage of nickel deposition, it has been found that the magnetic field increases the (200) texture by levelling the pyramidal islands formed in the nucleation of Ni.

Chapter 5 introduced a new engineering approach of fabricating high quality coating, which involved using rotating magnets to produce alternative magnetic fields. The main difference between the spinning magnetic fields and the static magnetic fields is the generation of the induced electric field under the rotating magnetic fields, which have yielded a very different coating surface roughness and (200) texture coefficient.

The micro-hardness of the nickel deposits formed under various magnetic conditions was characterized in Chapter 6. The highest hardness value was recorded when electrodeposition was conducted in the rotating magnetic field with a spinning rate of 2500 rpm. It has also been determined that the hardness of the deposits can be correlated to the coating roughness by a relationship similar to the Hall-Petch relationship for grain-boundary strengthening.

Chapter 7 summarizes the concluding remarks of this research.

## **1.2 Objectives**

This research project was initiated to investigate some theoretical and technical problems in electrodeposition. The primary motivation was to develop deposits with varied physical, chemical and mechanical properties. The emphases of the investigation were placed on both engineering applications and the fundamental understanding of plating mechanisms.

In the area of engineering application, particular attention was paid to the co-deposition of Cu/Ni coatings and nickel coating in the presence of magnetic field. Efforts were made to deposit Ni-Cu alloy films containing high concentrations of Cu but retaining the color of metal nickel, and to develop a novel engineering technique that would use a superimposed magnetic field to fabricate high quality metal film.

In the aspect of fundamental research, extensive efforts were made to understand the effect of magnetic fields on electrodeposition, to reveal the details of the Lorentz force acting on the electrodeposition process that modifies both the coating morphology and crystal texture, and to explain experimental phenomena in this research field that have not been clearly understood so far.

It is hoped that this research will facilitate the generation of new knowledge and techniques in the future development of electroplating technology.

### **1.3 Electrodeposition**

Numerous deposition techniques to fabricate metallic films have been developed, such as chemical vapor deposition, spin coating, atomic layer deposition, electrodeposition, physical vapor deposition, sputtering, and molecular beam epitaxy. Among them, electrodeposition stands out for its inexpensiveness, simplicity and flexibility to produce material films of variable thickness and area, multilayers, pure metal, alloy, oxide, or semiconductor like GaAs<sup>1</sup>, thus makes it the most commercially important deposition process. So far, enormous effort has been made in theoretical and practical studies of the electrodeposition process and countless results have been reported. On the other hand, many issues still need to be addressed both in the theoretical study and industrial practice. The scenario can best be illustrated with the example of nickel plating, which is one of the most popular deposition techniques. Though the study of nickel plating can be traced back to the 19th century<sup>1</sup>, the exploration for the related underlying mechanisms under various conditions still proceeds nowadays<sup>2-7</sup>.

## 1.4 Ni/Cu Codeposition

### 1.4.1 Overview

In recent decades, growing interest has been paid to nickel–copper alloys, not only for decorative purposes, but also due to their attractive features of enhanced wear and corrosion resistance, high thermal and electrical conductivity<sup>2,8</sup>, and desirable magnetic properties such as giant magnetoresistance (GMR) effect in multilayered Ni-Cu/Cu coatings<sup>8</sup>. Ni/Cu films have found extensive industrial applications in polluted or salt water environments for ships, pipelines, fittings condenser, valves, heat exchanger tubes and other marine applications, as well as in hydrogenation and dehydrogenation catalysts<sup>9</sup>.

The in-depth research on Ni-Cu codeposition commenced in the early 20<sup>th</sup> century. In 1959, Priscott<sup>10</sup> conducted a systematic study of this alloy deposition, in which the dependence of coating composition and current efficiency on the deposition conditions of cathodic current density, bath temperature, and agitation were examined. Also, the recorded hardness of the Ni-Cu film was larger than that of the pure Ni obtained from a Watts bath.

Later, the early research work on Ni-Cu electroplating was summarized by Brenner<sup>11</sup> in 1963 and Roos<sup>12</sup> in 1984. However, the current efficiencies to obtain Ni-Cu alloys with high Ni content in the early experiments were low, until 1984, Roos *et al*<sup>12</sup> and Chaissang *et al*.<sup>13</sup> developed nickel-rich alloys more readily and citrate was employed as complexing agent. In 1993, Madore<sup>14</sup> enhanced the current efficiency to approximately 100% in fabricating high quality Cu-Ni alloys. In addition, pulse plating was also investigated and employed to produce multilayer Ni-Cu films<sup>15</sup>.

The mechanism of Ni-Cu codeposition has been intensively studied especially for the complexing agent containing electrolytes. Some theoretical models have been proposed to explain the codeposition process in detail such as for citrate solution<sup>16-19</sup>.

Furthermore, many other aspects of deposited Ni-Cu film including corrosion resistance<sup>20</sup>, approaches to produce the nano-structured deposition layer<sup>21,22</sup>, the effect of additives<sup>23</sup>, and the stability of the plating bath<sup>24</sup>, have also been investigated.

#### **1.4.2 Complexing agent**

Copper and nickel have standard reduction potentials of +0.34V and -0.25V vs. standard hydrogen electrode (SHE)<sup>25</sup>, respectively. Because of the potential disparity, either low nickel content or low current efficiency will occur if nickel and copper salt are simply added together into the bath (e.g., adding CuSO<sub>4</sub> in the traditional Watt bath). Therefore a complex agent is needed to narrow the reduction potential gap to improve the codeposition quality. Electrolytes containing citrate<sup>10</sup>, cyanide<sup>26</sup>, sulfamate<sup>27</sup>, glycine<sup>28</sup>, sulphate-oxalate<sup>29</sup>, tartrate<sup>30</sup> and pyrophosphate<sup>31</sup> have been tested in Ni-Cu electrodeposition. Among these complexing agents, citrate and pyrophosphate have been most frequently employed<sup>2</sup>, and citrate is specifically attractive for its advantages of being inherently low toxic, low cost, and acting as brightening, levelling and buffering agent in electrodeposition<sup>32-34</sup>. For this reason, the present work is focused on the sodium citrate bath.

#### **1.4.3 Solution chemistry of the citrate bath**

To discuss the mechanism of Ni-Cu codeposition in the citrate bath, it is necessary to understand the solution chemistry of the citrate electrolyte.

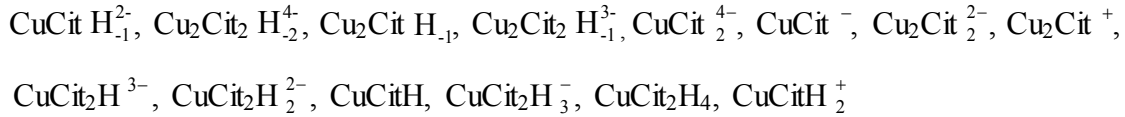
Citric acid, CitH<sub>3</sub>, is an organic acid with the formula of COOH-CH<sub>2</sub>-COH(COOH)-CH<sub>2</sub>-COOH, with three carboxylic functional groups and a hydroxyl group. The general equation for the formation of copper-citrate complexed species can be represented as<sup>35</sup> :



The formation constant is given by

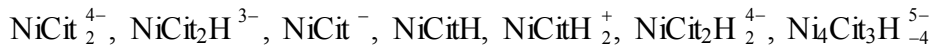
$$\beta_{pqr} = \frac{[\text{Cu}_p\text{Cit}_q\text{H}_r^{(2p-3q+r)+}]}{[\text{Cu}^{2+}]^p[\text{Cit}^{3-}]^q[\text{H}^+]^r} \quad 1- (2)$$

There are 14 different copper-citrate complex species being considered in the solution chemistry<sup>35</sup> :



Where the negative subscript denotes the citrate ion to be quadruply ionized in the presence of cupric ions, under which the hydrogen atom of the hydroxyl group is labile and can be deprotonated.

Similarly, the nickel-citrate complex species considered in the solution chemistry are listed below<sup>19</sup> :

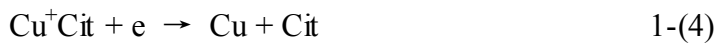


Both copper-citrate and nickel-citrate solution chemistry can be computed with the pK values and complexation constants suggested by Daniele et al.<sup>36</sup>

#### 1.4.4 Codeposition mechanism in citrate bath

Several attempts have been made so far to develop a model to understand the mechanism of nickel and copper codeposition in the citrate bath. In 1987, Chassaing *et al.*<sup>16</sup> designed a model with two steps for the parallel discharge of the nickel ion  $\text{Ni}^{2+}$  and the complexed cupric species  $\text{Cu}^{2+}\text{Cit}$ , respectively.

For copper reduction:



For nickel reduction, the two-step reduction process is thought to involve an adsorbed intermediate species  $(\text{Ni}^+)_{\text{ads}}$ .



Also, the nickel reduction is considered to occur on catalytic active sites,  $s$ , which nucleates from the  $(\text{Ni}^+)_{\text{ads}}$  on the surface of the alloy deposit.

According to the authors, the active site  $s$  is probably formed by some special bonds and /or arrangements between nickel and copper atoms, associating one nickel atom with several copper atoms, on the cathode surface which gives them a particular activity.



The active sites are continuously renewed by being consumed by Cu and  $\text{Ni}_{(\text{ads})}^+$ . The reactions are:



Also, based on the experimental result, a catalyzing effect of the copper on the nickel reduction was put forward.

In 1988, Ying *et al.*<sup>17</sup> proposed another model for Ni/Cu codeposition. In their model, the following nine reactions were considered:



By calculating and comparing the concentrations of various metal species in the bath, the dominant reactant species in the bulk solution were determined to be the metal complexes  $\text{CuCit}^-$  and  $\text{NiCit}^-$ , and only the following reactions are taken into account for the model of the diffusion layer:



On the electrode surface, the following reactions are assumed to occur:



The calculated result based on this model was not satisfactorily consistent with the experiment.

In 1994, Podlaha *et al.*<sup>18</sup> modeled the Ni/Cu codeposition in citrate bath containing a large excess of nickel. They considered the deposition of both complexed species of  $\text{CuCit}^-$ ,  $\text{NiCit}^-$  and uncomplexed species  $\text{Cu}^{2+}$ ,  $\text{Ni}^{2+}$ , and the distribution of them in the diffusion boundary layer. This model obtained a better result than that of Ying *et al.* in fitting the diffusion coefficients of the complexed species.

In 2005, Sabine Rode, *et al.*<sup>19</sup> suggested another kinetic model on the basis of the above research work. They believed that all the complexed species in the solution, not just CuCit<sup>-</sup> and NiCit, should be considered in the reduction process of nickel and copper.

Using the formation constants determined by Daniele *et al.*<sup>36</sup>, the authors calculated the chelate species distribution for a nickel-copper citrate bath. The nickel-citrate complex species and copper-citrate complex species distribution are shown in Fig. 1-1 and Fig. 1-2, respectively.

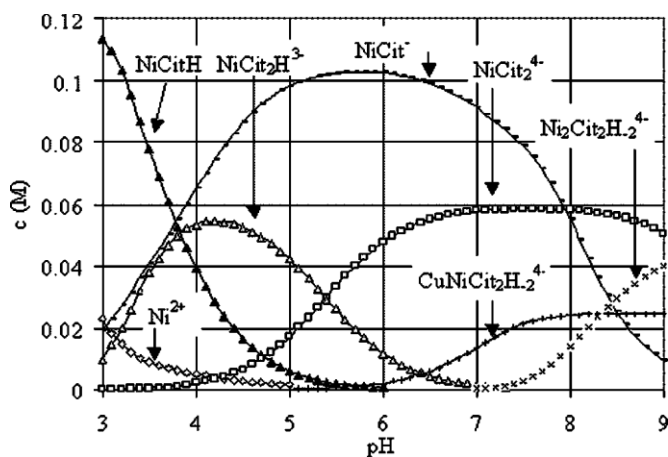


Figure 1-1 Distribution of the nickel-citrate species with the solution pH in a nickel-copper citrate solution (Fig. 5 in Ref. 19).

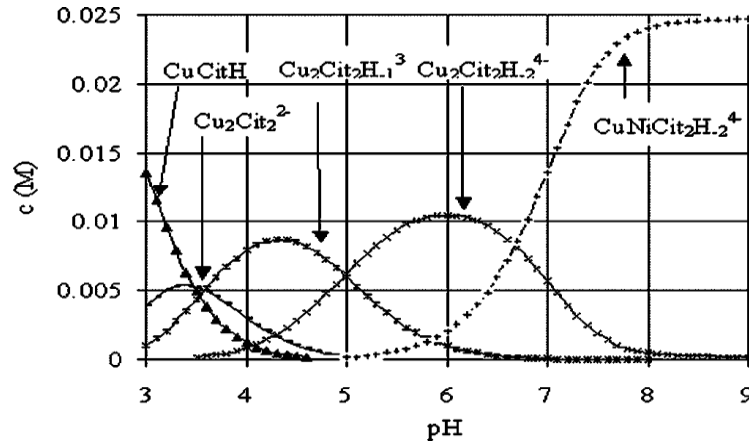


Figure 1-2 Distribution of the copper-citrate species with the solution pH in a nickel-copper citrate solution (Fig. 4 in Ref. 19).

In the model of Sabine Rode, *et al.*<sup>19</sup>, the nickel deposition is assumed to proceed through a one-step direct discharge of a hypothetical pseudo-species,  $\text{NiCit}^-$  (p), which includes all complexed nickel species except the binuclear species of  $\text{Ni}_2\text{Cit}_2\text{H}_{-2}^{4-}$  and  $\text{NiCuCit}_2\text{H}_{-2}^{4-}$ . Fig. 1-1 shows that  $\text{NiCit}^-$  (p) is the dominate species in the pH range from 4 to 8.

The reactions considered in the nickel-copper codeposition are:

Copper deposition:





Nickel deposition:



This model gave results that are fairly consistent with the experimental measurement.

### 1.4.5 Electrochemical behaviour in Ni/Cu co-deposition bath

Some variations in the reduction features of nickel and copper occur in the nickel-copper citrate bath, compared to the nickel-citrate bath or copper-citrate bath.

Chassaing *et al.*<sup>16</sup> pointed out in their paper that the existence of copper catalyzes the reduction of nickel. This point was supported by Sabine Rode *et al.*<sup>19</sup>. The experimental results of Rode *et al.* are shown in Fig. 1-3 and Fig. 1-4.

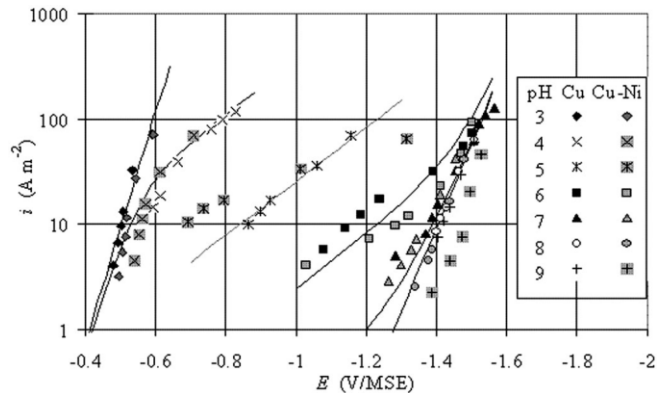


Figure 1-3 Steady-state partial copper current curves in a copper-citrate bath and in a copper-nickel citrate bath at different pH values (Fig. 6 in Ref. 19).

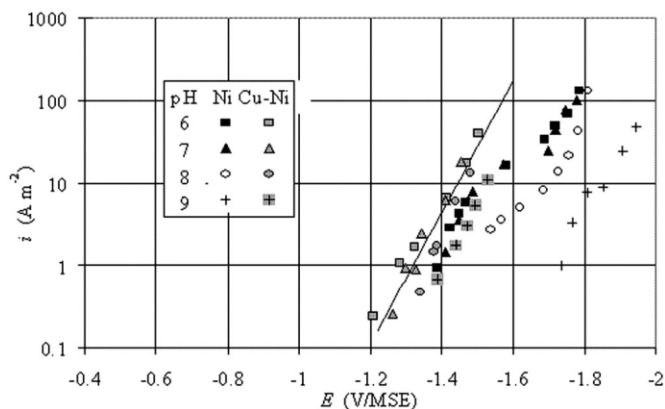


Figure 1-4 Steady-state partial nickel current curves in a nickel-citrate bath and in a copper-nickel citrate bath at different pH values (Fig. 7 in Ref. 19).

Fig. 1-4 shows that the partial copper-current curves with and without nickel when the pH is lower than 9 are practically identical. Thus the copper reduction is almost unchanged in the mixed-metal solution at  $\text{pH} < 9$ . For  $\text{pH} = 9$ , the partial copper current curve shifts slightly to the negative range in the mixed-metal solution, indicating an inhibition effect because of the existence of nickel. It is also implied from Fig. 1-4 that the copper deposition behavior is strongly dependent on the bath pH. The pH increase shifts the copper partial reduction curve to a more negative potential, making the copper reduction more difficult.

A remarkable feature in Fig. 1-4 is that in the presence of copper, the partial deposition curve of Ni is shifted to more positive potential ranges, and the slopes become larger. This result has revealed the catalyzing effect of the copper on the nickel reduction.

Besides, according to Sabine Rode *et al.*<sup>19</sup>, the current efficiencies for a nickel-copper codeposition bath are much higher than those for single nickel citrate plating baths. The reason for this may be due to the shift to more a positive range of the partial deposition curve for nickel which has suppressed the side reaction of the hydrogen reduction.

#### 1.4.6 Bath stability

One major problem concerning the application of the citrate as complexing agent in Ni-Cu codeposition is the instability of the bath, i.e., the generation of blue-colored precipitates in the bulk solution occurred for many plating solutions in research after a few days of use<sup>12,13</sup>. This has limited the industrial use of this codeposition technique. The precipitate was generally assumed to be an insoluble copper citrate complex at first, usually formulated as  $\text{Cu}_2\text{C}_6\text{H}_4\text{O}_7 \cdot 2\text{H}_2\text{O}$  or  $\text{Cu}_2\text{H}_1\text{Cit} \cdot 2\text{H}_2\text{O}$ <sup>37,38</sup>.

In 1998, Green *et al.*<sup>24</sup> confirmed that the  $\text{Cu}_2\text{H}_1\text{Cit}$  was indeed the precursor of the precipitate by means of inductively coupled plasma atomic emission spectroscopy (ICP-AES), carbon-hydrogen-nitrogen analyzer and infrared spectroscopy. Their subsequent investigation revealed a more complex process that after the precursor complex  $\text{Cu}_2\text{H}_1\text{Cit}$  was generated in the bath, some of the  $\text{Cu}^{2+}$  ions were slowly replaced with  $\text{Ni}^{2+}$  ions, resulting in the eventual insoluble heteronuclear citrate complex, with a suggested formula of  $\text{Cu}_{1.5}\text{Ni}_{0.5}\text{H}_1\text{Cit}_6 \cdot \text{H}_2\text{O}$ .

Calculation was performed by Green *et al.*<sup>24</sup> to determine the concentration distribution of Ni and Cu complex species as the function of pH in an electrolyte containing 0.025M  $\text{CuSO}_4$ , 0.7 M  $\text{NiSO}_4$  and 0.26 M sodium citrate, which had been reported unstable<sup>39</sup>. The result shows clearly that the concentration of  $\text{Cu}_2\text{H}_1\text{Cit}$  is negligible when  $\text{pH} > 2$  or  $< 6$ . At  $\text{pH} > 6.5$ , another insoluble inorganic precipitate  $\text{Ni}_4(\text{OH})_6\text{SO}_4$  begins to appear. Therefore, pH 6 was recommended as the favorable condition to keep the electrolyte stable.

Green *et al.* developed a useful technique of speciation modeling to design and optimize the electrodeposition bath. However, two aspects were neglected in their research. First, only the bulk solution was examined. Also, the surface regions of electrodes, both anode and cathode,

were not considered. In fact, the pH on the electrodes' surface differs from that of bulk solution<sup>40</sup> due to the side reactions of oxygen and hydrogen evolution on the anode and cathode respectively. For Ni-Cu codeposition, if the bath pH is 6, the local pH on cathode surface will be higher; therefore, the green colored precipitate  $\text{Ni}_4(\text{OH})_6\text{SO}_4$  will potentially develop on the cathode surface and diffuse into bath, which has been observed in our experiment. Second, the investigation was conducted at room temperature. The situation will be different for higher temperatures which are often employed in experimental research and industry. The present work will examine the suitable conditions of temperature and pH in the following section.

## **1.5 Electrodeposition in magnetic field**

### **1.5.1 Overview**

The electrodeposition in the presence of an applied magnetic field, known as magnetoelectrolysis (ME) or magneto-electrolytic deposition (MED)<sup>41,42</sup>, has drawn considerable attention in the past years because it has been established that the magnetic field could significantly affect the electrodeposition process by yielding some unique phenomena, such as magnetohydrodynamic effect (MHE) and magnetocrystalline anisotropy effect, etc., which bring about the altered structure and quality of the deposited films, as well as changes in physical properties and transport features of the electrolyte<sup>43</sup>. Although MED is not industrially employed at present, its potential applications are considered promising<sup>44</sup>.

The examination of magnetic fields on metal deposition started at the end of the 19<sup>th</sup> century<sup>45</sup> and the first observation is believed to have come from Faraday. However, because of the low

magnitude of the magnetic field available at that time, limited interest was paid to this technique<sup>44</sup>.

It was not until the end of the 20<sup>th</sup> century that systematic investigations arose. Since then, numerous results have been reported<sup>42</sup>.

It is generally accepted that the influence of the magnetic field on the electrodeposition process can be roughly classified into three main categories: the physical properties of the electrolyte, the mass transport process and the quality and structure of the deposits. In addition, the magnetic field effect on the electrode kinetics is subject to controversy. Experimental results tend to prove it is ineffective<sup>44,46</sup> because the detected changes in charge transfer might be ascribed to indirectly altered mass transport<sup>47</sup>.

Furthermore, the investigations of MED are normally performed in two different kinds of arrangement: the magnetic field is either parallel or perpendicular to the electrode surface. The former is designed to maximize the magnetic field induced convection in the ion transport, while the latter is applied to eliminate the convection due to the magnetic field and study the paramagnetic force and field gradient effects<sup>48</sup>.

## **1.5.2 Fundamentals of magneto-electrolytic deposition (MED)**

### **a. Magnetically induced forces**

Several possible forces are believed to be related to the observed magnetic field effects in electrodeposition<sup>49</sup>. They are either due to the movement of charged particles or are related to the magnetic properties of the electrolyte.

The first one is the Lorentz force,  $\vec{F}_L$ :

$$\vec{F}_L = \vec{j} \times \vec{B} \quad 1-(32)$$

Here  $\vec{j}$  and  $\vec{B}$  are current density and magnetic flux density, respectively.  $\vec{F}_L$  originates from the motion of the electric charge across the magnetic field lines. In electrodeposition, the charged particles moving in the electrolyte under the superposition of the magnetic field will experience this force and change their trajectories into spiral lines. This results in an enhanced convection in the electrolyte, which is referred to as the MHD effect<sup>50</sup>.

If an electrolyte contains paramagnetic ions such as  $\text{Cu}^{2+}$ ,  $\text{Fe}^{2+}$ ,  $\text{Ni}^{2+}$ , etc., the field gradient force,  $\vec{F}_B$ , is generated.

$$\vec{F}_B = \frac{\chi_m c B \nabla B}{\mu_0} \quad 1-(33)$$

Where  $\chi_m$  is the molar susceptibility of paramagnetic species,  $c$  is the concentration and  $\mu_0$  is the vacuum permeability, ( $\mu_0 = 4\pi \times 10^{-7} \text{ Hm}^{-1}$ ).

$\vec{F}_B$  corresponds to the field gradient in the electrolyte if the magnetic field is not uniform. According to 1-(33), it drives the paramagnetic ions in the direction of magnetic field gradient.

When the concentration distribution of the paramagnetic ions is non-uniform in the electrolyte, another force called the paramagnetic gradient force  $\vec{F}_P$  should be taken into account.

$$\vec{F}_P = \frac{\chi_m B^2 \nabla c}{2\mu_0} \quad 1-(34)$$

$\vec{F}_P$  is expected to be significant inside the diffusion layer where an ion concentration gradient exists.

Actually, the  $\vec{F}_B$  and  $\vec{F}_P$  can be derived by differentiating the energy density  $E$  of the electrolyte,

$$E = -\chi_m \frac{B^2}{2\mu_0} c \quad 1-(35)$$

And  $\vec{F} = -\nabla E$  yields two terms,  $\vec{F}_P$  and  $\vec{F}_B$ .

Furthermore, the last force which is also correlated to the magnetic field effect is the magnetic damping force  $\vec{F}_M$ <sup>51</sup>.

$$\vec{F}_M = \sigma \vec{v} \times \vec{B} \times \vec{B} \quad 1-(36)$$

In which  $\sigma$  is the solution conductivity, and  $\vec{v}$  is the velocity of the solution flow.

This force arises from the magnetic field induced by the eddy electric current of the moving ions as a result of the Lorentz force in the solution, and is negligible in the aqueous electrolyte due to the low solution conductivity<sup>49</sup>.

Among the four different forces introduced above, the Lorentz force is well established as having a significant effect on the electrodeposition process, e.g., the mass transport in the bath<sup>42</sup>. The paramagnetic force which is only significant in the diffusion layer, acts in the direction of concentration gradient. It aligns with the thermodynamic driving force for diffusion. Estimation has been made by G. Hinds *et al.*<sup>49</sup> that the ratio of these two forces is of the order of  $10^{-6}$ , indicating the negligibility of the paramagnetic force compared to the thermodynamic driving force in mass transport.

On the other hand, the field gradient force is absent in the uniform magnetic field, but may play an important role in electrodeposition when an inhomogeneous magnetic field is applied, and has been employed to fabricate some specially intended film morphologies<sup>52,53</sup>. However, unless in deliberately designed experimental conditions so that  $\nabla B \gg 1\text{T/m}$ , the field gradient force is on the order of  $10\text{ N/m}^3$ , which is only about 1% of the Lorentz force in electrolyte<sup>49,54,55</sup>.

In summary, in the various kinds of magnetic field-related forces being discussed, the Lorentz force is dominant in the aqueous electrolyte. Thus, the Lorentz force is mainly responsible for the magnetic field influences occurring in the electrodeposition when the deposition is carried out in aqueous bath.

### **b. Magnetohydrodynamics**

Magnetohydrodynamics<sup>56</sup> studies the dynamics of electrically conducting fluids in magnetic field.

Because of the conductivity of the fluid, it generates an electric current and the induced magnetic field, which in turn impact the fluid motion.

The basic magnetohydrodynamic equations for a Newtonian, constant property fluid flow include the Navier-Stokes equation (i.e., momentum equation), Maxwell equations, mass continuity equation, and Ohm's Law. In differential form they are as follows:

$$\vec{j} = \sigma(\vec{E} + \vec{v} \times \vec{B}) \quad 1-(37)$$

$$\frac{\partial \rho}{\partial t} + \nabla \cdot \rho \vec{v} = 0 \quad 1-(38)$$

$$\rho \left[ \frac{\partial \vec{u}}{\partial t} + (\vec{u} \cdot \nabla) \vec{u} \right] = -\nabla p + \vec{j} \times \vec{B} + \nu \nabla^2 \vec{v} + \rho \vec{F}_i \quad 1-(39)$$

$$\nabla \times \vec{E} = -\frac{\partial \vec{B}}{\partial t} \quad 1-(40)$$

$$\nabla \times \vec{B} = \mu_m \vec{j} \quad 1-(41)$$

Equation 1-(37) is Ohm's law; Eq. 1-(38) expresses mass continuity; Eq. 1-(40) and Eq. 1-(41) are Maxwell equations; and Eq. 1-(39) is the Navier-Stokes equation.

The Navier-Stokes Eq. 1-(39) is Newton's second law for the incompressible fluid. The left side of Eq. 1-(39) represents the acceleration of the fluid element, and the right side of Eq. 1-(39) is the sum of external volume forces on the fluid element. On the right side, the first term refers to the force from the pressure gradient through the system; the second term is the Lorentz force; the third term is due to the effect of viscous forces, and  $\nu$  is the kinematic viscosity of the fluid; and the fourth term accounts for any other external volume forces, including gravity, and electric force.

Generally, the differential equations derived from the Navier-Stokes equation are nonlinear. Thus there is no complete analytical solution, and usually numerical methods are employed.

### 1.5.3. Magnetic field effect on electrolyte properties

The electrolyte contains charged particles. Thus when exposed to an superimposed magnetic field, the charged particles, the ions, will experience the impact of both the electric field and magnetic field. The total force is:

$$\vec{F} = q(\vec{E} + \vec{V}_p \times \vec{B}) \quad 1-(42)$$

The second term on the right side of Eq. 1-(42) makes the trajectories of the ions in the bath varied and the changes in the electrolyte properties are expected.

### **Hall effect**

Similar in the case of metals or semiconductors, the existence of the Lorentz force on moving ions in the solution (the second term in Eq. 1-(42)) generates Hall effect in the electrolyte. In equilibrium conditions, the total electric field intensity can be derived as<sup>41</sup>:

$$\vec{E} = \frac{\vec{j}}{\sigma} - R_H(\vec{j} \times \vec{B}) \quad 1-(43)$$

Where  $\vec{j}$  is the current density,  $\sigma$  the electrolyte conductivity and  $R_H$  the Hall constant.

A theoretical estimation of  $R_H$  was carried out by some researches. Different kinds of formulae have been developed. This work was introduced in the reviewing paper of T. Z. Fahidy<sup>41</sup>.

### **Conductivity**

Early studies on the electrolyte conductivity under magnetic field observed an increase by a factor of 1.04-1.2 compared to the conventional conductivity<sup>44</sup>. A theoretical interpretation was proposed using plasma theory<sup>57</sup>. However, the effect is still not well understood<sup>41</sup>.

### **Temperature**

Thermal effects were reported in the work of Tronel-Peyroz *et al*<sup>58-60</sup> and Olivier<sup>61</sup>. When the DC current flowed through an electrolyte under a homogeneous magnetic field, a higher solution temperature with magnitude of a fraction of one degree after a transient period was recorded. Olivier explained the phenomenon in terms of the kinetic energy of ions and the ionic relaxation time<sup>61</sup>.

## Viscosity and diffusivity

Also, the electrolyte viscosity was found to increase under magnetic field. Lielmezs *et al.*<sup>62,63</sup> measured the viscosity of aqueous KCl and observed the relative increase at  $B = 1.2\text{T}$  compared to the absence of the magnetic field, and, the viscosity increase dropped and diminished when the KCl concentration increased. At a lower magnetic field, the relative increase of viscosity is lower. A similar result was recorded for the diffusivity of certain monovalent halides<sup>63,64</sup>.

### 1.5.4. Magnetic field effect on mass transport

Under an external magnetic field, the mass transport process in the electrolyte can be significantly modified compared to the relatively weak influence on physical properties discussed above, especially when the system is under diffusion control<sup>44</sup>. This effect has been most intensively studied. Measurements have revealed that increasing the magnetic field intensity gives rise to the limiting current increase<sup>44,46,65,66</sup>, as shown in Fig. 1-5 (from Ref. 46). In addition, the existence of the critical value of the magnetic field flux density beyond which the diffusion limit disappeared was also observed<sup>44</sup>.

In 1973, Fahidy<sup>67</sup> studied the MHD effect in mass transport and proposed a semi-empirical model. The relationship between the limiting current density and the magnetic flux density was established as power dependence:

$$i_L = i_L^o + aB^m \quad 1-(44)$$

where:  $i_L^o$  and  $i_L$  are limiting current densities without and with the magnetic field, respectively;  $a$  and  $m$  are empirical constants.

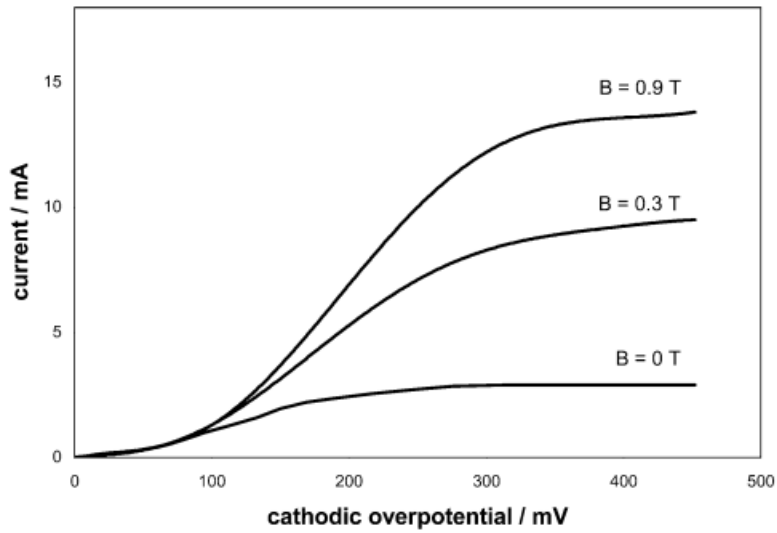


Figure 1-5 Dependence of limiting current on magnetic field intensity (Fig. 2 in Ref. 44).

Later in 1975, Aogaki *et al.*<sup>68,69</sup> investigated the convective effect of an applied magnetic field on the limiting current density in Cu electrodeposition, with the field oriented parallel to the electrode surface. They approximately solved the Navier-Stokes equation and showed that the limiting current density was proportional to  $c^{4/3}$  and  $B^b$ , and the exponent  $b$  varies between 0.3 and 0.5, depending on the cell and electrode geometry. In 1987, A. Oliver *et al.*<sup>70</sup> studied the I-E curve of the ferri-ferrocyanide redox couple and discovered the following relationship:

$$i_L = kB^{1/3}c_0^{4/3} \quad 1-(45)$$

$c_0$  is the concentration of the electroactive species in the bulk electrolyte.

The proportional correlation of the limiting current with  $c^{4/3}B^{1/3}$  has subsequently been confirmed by numerous researchers<sup>71-74</sup>.

More recently, the relationship between the limiting current and the magnetic flux density has been identified in terms of the field arrangement, that if  $B$  is parallel to the electrode surface,  $i_L$  is proportional to  $c_0^{4/3} B^{1/3}$ ; while in a perpendicular magnetic field situation, due to the influence of the magnetic properties of the electroactive species and paramagnetic gradient force<sup>75,76</sup>, the relation becomes  $i_L \propto c_0^{4/3} B^{2/3}$ .

In addition, apart from the contribution of  $B$  to the limiting current, other parameters, such as the kinematic viscosity, the number of electrons involved in the electrochemical reaction, and the dimension of the electrode, the dielectric constant of the electrolyte, were also specified as reasons for the limiting current change<sup>77,78</sup>, e.g., in ref. 78, a quantified empirical expression was established as:

$$i_B = Kc^{4/3} Dd^{5/3} \nu^{-2/3} \varepsilon^{-7/4} B^{1/3} n \quad 1-(46)$$

In which  $C$  denotes the electroactive species concentration,  $D$  the diffusion coefficient,  $d$  the working electrode diameter,  $\nu$  the kinematic viscosity of the electrolyte,  $\varepsilon$  the dielectric constant of the solution,  $n$  the number of electrons involved in the redox process and  $K$  the proportionality constant.

Regarding the physical mechanism of the limiting current change resulting from the superimposition of the magnetic field, the consensus is that the MHD flow induced by the Lorentz force on the moving ions is responsible for the observed effects. Researchers believe that the Lorentz force induced convection creates a fluid flow parallel to the electrolyte surface<sup>79</sup>. Hinds *et al.*<sup>46</sup> suggested that this tangential flow in the bulk solution generates a hydrodynamic boundary layer (a hydrodynamic boundary layer is defined as the fluid region immediately adjacent to the solid surface where the flow velocity changes rapidly from zero to its value in the

bulk stream<sup>46</sup>), which has a velocity gradient that gives rise to the mixing in the diffusion layer and thus reduces its thickness. As a result, the diffusion rate of ions toward the electrode increases and, thus, the limiting current is enhanced.

### **1.5.5 Cathodic deposit morphology effects of the magnetic field**

Many authors have reported morphological changes of coatings while conducting electrodeposition in the external magnetic field<sup>46, 80-84</sup>.

Fig. 1-6 shows the experimental result from Ref. 84 of the SEM and AFM images of the CoFe alloy deposition in the magnetic field.

It is clear from Fig. 1-6 that the parallel applied magnetic field produced a smoother coating with a reduced grain size and surface roughness than the absence of the field; conversely, in the perpendicular field configuration, the deposited layer is rough and diverse with a tendency of columnar grain growth along the magnetic field direction. In fact, the data from the AFM line section analysis result shows that the perpendicular magnetic field resulted in the highest surface roughness in those three cases.

In addition, the inhibition of dendrite growth by the superimposed magnetic field in electrodeposition was also reported<sup>85,86</sup>. For example, in Ref. 85, the growth of dendrites zinc deposition from alkaline zincate baths was effectively inhibited by the magnetic field.

In summary, according to the literature survey, the smoother coating films generally result from the parallel applied magnetic field, while the magnetic field perpendicular to the electrode tends to roughen the coating surface. However, researchers have occasionally observed that the

parallel magnetic field has increased the deposit roughness. For example, Ref. 46 reported that Cu film became rougher under parallel field, as seen in Fig. 1-7.

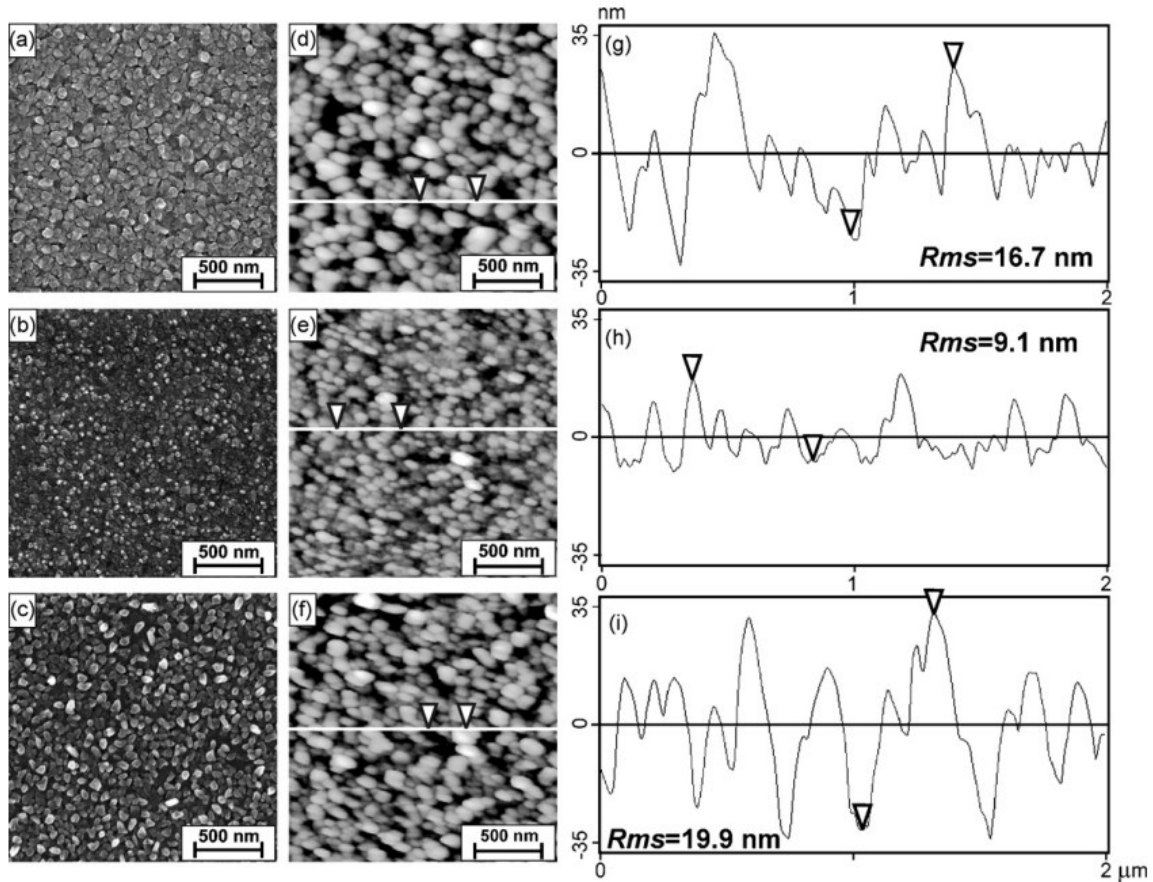


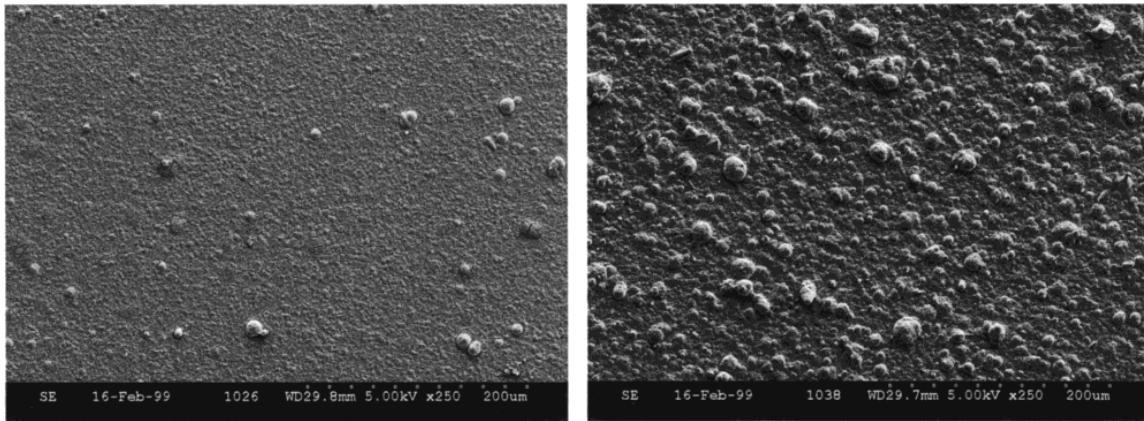
Figure 1-6 SEM micrographs and corresponding AFM images with line section analysis of layers deposited without magnetic field (a, d and g), in parallel (b, e and h) and perpendicular-to-electrode (c, f and i) configurations ( $B = 1\text{T}$ ) (Fig. 4 in Ref. 46).

On the other hand, many research groups have reported a noticeable phenomenon in the MED process<sup>82,84,87-89</sup>, i.e., the occurrence of the elongated grains growing in the direction of the

external magnetic field, both in parallel and vertical magnetic fields, which is, to date, not well understood.

Fig. 1-8 to Fig. 1-11 display the elongated grains or columnar structures that have appeared in MED in parallel or perpendicular magnetic fields. These figures are from the references denoted.

Fig. 1-9 shows that the grain size of the Fe deposit tends to decrease with the increase of magnetic flux density.



(a)

(b)

Figure 1-7 SEM images of copper deposited with (a) no magnetic field and (b) a parallel field of 0.5 T (Fig. 14 in Ref 46).

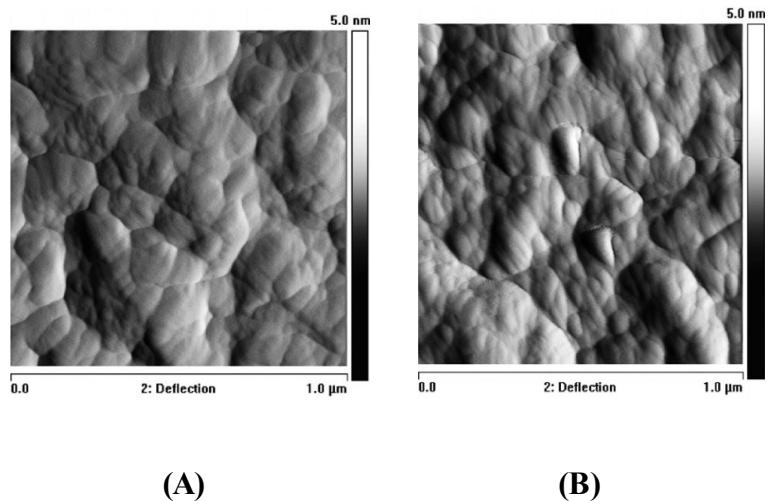


Figure 1-8 AFM images of the layers of deposited NiFe alloy in the magnetic field of (A) 0 T, (B) 0.615 T, parallel (Fig. 11 in Ref. 89).

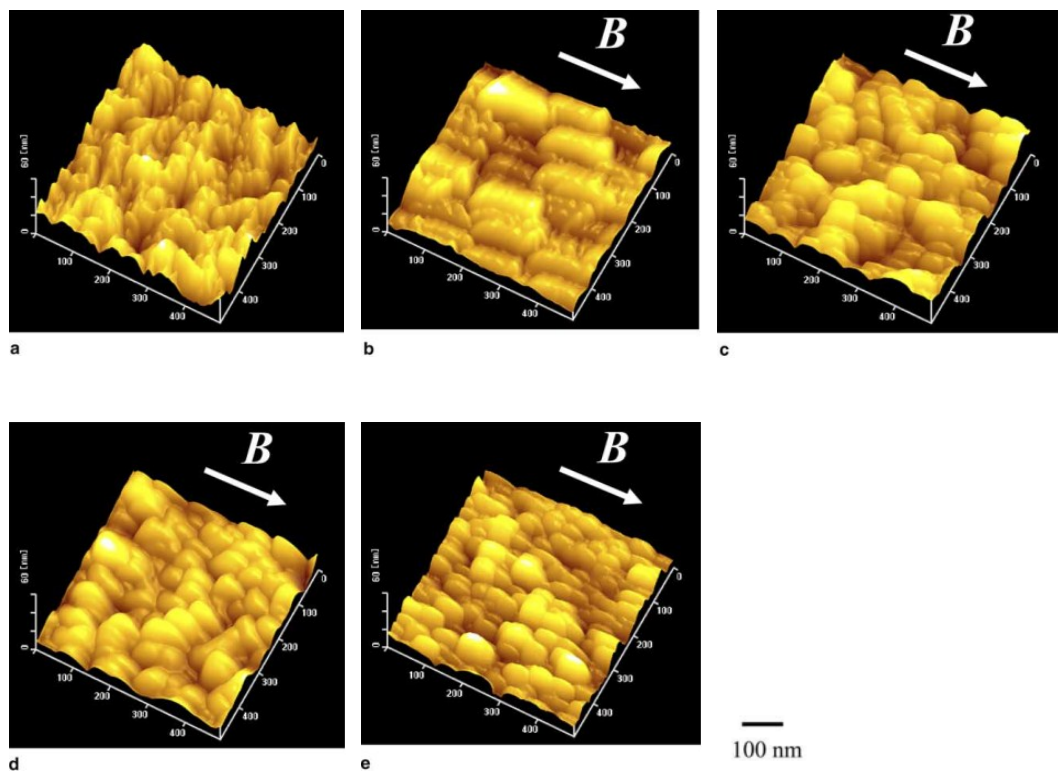


Figure 1-9 AFM images of the iron films electrodeposited in the parallel magnetic fields of (a) 0 T, (b) 0.5 T, (c) 1 T, (d) 3 T and (e) 5 T (Fig. 1 in Ref. 87).

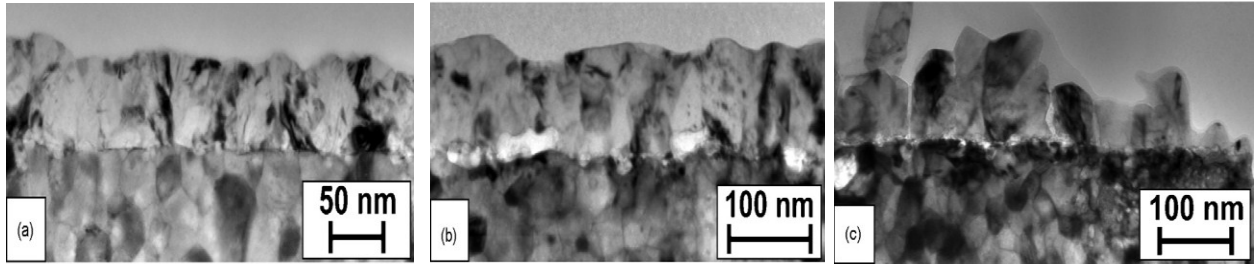


Figure 1-10 TEM images of the cross-sections of deposited CoFe layers without (a), in parallel (b) and perpendicular (c) magnetic fields ( $B = 1$  T) (Fig. 5 in Ref. 84).

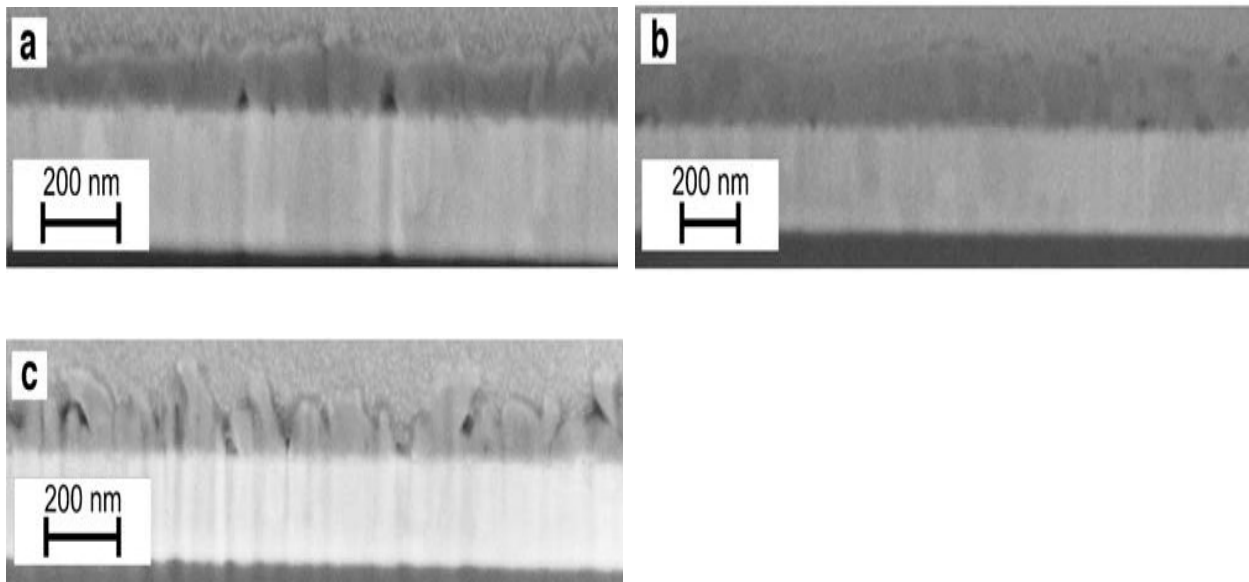


Figure 1-11 SEM cross section view of the deposited Fe layers in (a): 0T, (b) 1T, parallel and (c) 1T, perpendicular magnetic fields (Fig. 14 in Ref. 88).

### 1.5.6 Proposed mechanisms of the deposit morphology change in magnetic field

So far, much effort has been devoted to understanding the mechanism governing the morphological change of the deposit obtained in the magnetic field. Various theories have been

proposed. In a homogeneous field, it is well established that the origin of this change is the MHD effect, which introduces additional convection in the electrolyte. The investigations are approximately classified into two cases: parallel and vertical magnetic fields to the electrode surface.

### **Parallel field configuration**

The parallel magnetic field is generally believed to reduce the deposit roughness. Several mechanisms have been put forward.

In 2003, Bund *et al.*<sup>90</sup> studied Ni and Cu deposition in the presence of the parallel magnetic field and reported that the MHD forced convection flow occurred when the electrolysis process is under diffusion control, resulting in a higher limiting current density that leads to an increase in the deposition rate and thus modifies the surface morphology of the coating by forming finer-grained deposit. Their explanation was based on the electrodeposition theory<sup>91</sup> that the crystal sizes of some metals decrease as the deposition rate increases.

When the electrolysis system is under kinetics or mix control, in 1998, O. Devos *et al.*<sup>81,92</sup> experimented on a Ni deposition in the parallel magnetic field with a pure Watts bath and a modified Watts bath with 2-butyne-1,4-diol (BD). For the pure Watts bath, no significant morphological change was found, while in the BD-added bath, when the magnetic flux density was higher than 0.6T, a significant grain size reduction, accompanied by an obvious current density decrease, resulted in a bright surface. The current density decrease and the consequent grain refinement were attributed to the increase in the convective flow, caused by the MHD effect, of the inhibitor BD which was under diffusion control. Furthermore, the hydrogenation catalyzed by BD on the cathode surface caused the local pH increase and the generation of base

salts as inhibitors, which also contributed to the grain size decrease. In addition, the authors observed that the morphology of the pits on the coating surface caused by the attachment of hydrogen bubbles changed dramatically in the simultaneous presence of the inhibitor BD and the parallel magnetic field, as depicted in Fig. 1-12. The phenomenon was explained by means of the interaction between natural convection and the magnetic field-induced convective flow of BD in the neighborhood of the hydrogen bubble. The BD inhibition was smaller in the front side of the bubble and was facilitated by turbulent drag behind the bubble. Fig. 1-13 schematically describes this formation process.

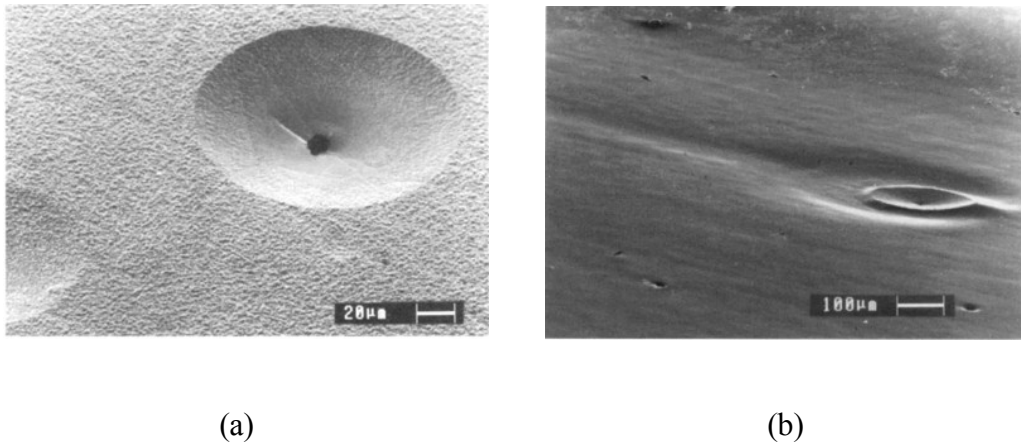


Figure 1-12 Morphological difference between the hydrogen bubble pit on the nickel deposit surface in the (a) absence and (b) presence of the parallel magnetic field (Fig. 7 and 8 in Ref. 92).

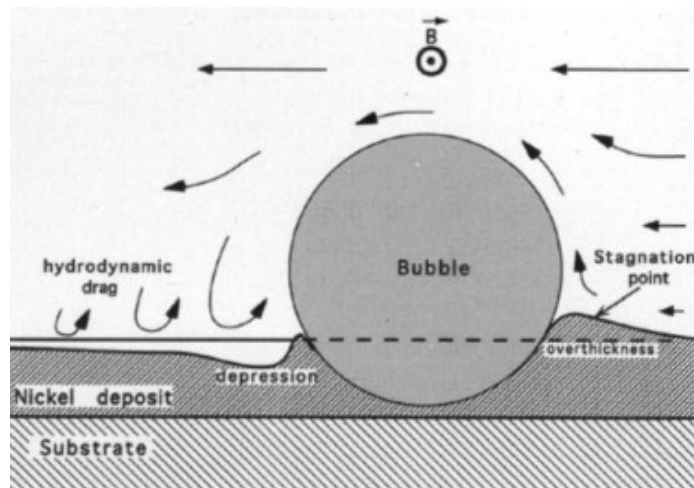


Figure 1-13 Schematic presentation of the formation mechanism of the morphology around a hydrogen pit in the parallel magnetic field (Fig. 10 in Ref. 92).

Also in 2003, Tabakovic *et al.*<sup>93</sup> explained the surface roughness decrease of the NiFe plating in the magnetic field and suggested two reasons: first, the faster additive (saccharin) adsorption and/or faster  $H^+$  discharge due to the induced magnetic convection at the protrusions on the electrode surface blocked them and therefore promoted the metal deposition in the valleys. This produced a levelling effect to lower the surface roughness; second, the enhanced adsorption of the inhibitors shortened the diffusion length of the surface adatoms and lead to a higher nucleation density and smaller grains.

In 2004 and 2005, Krause *et al.*<sup>94,95</sup> studied Co deposition in the magnetic field and reported that the surface holes left by hydrogen evolution disappeared in the presence of the magnetic field. They assumed that the MHD convection supported the removal of the hydrogen bubbles from the cathode so as to avoid the holes forming on the deposit and thus smoothed the coating.

Also, Aogaki introduced the concept of “micro-MHD effect”<sup>96</sup> (to be discussed in the next section) to interpret the morphology change in the magnetic field. He demonstrated that in the parallel magnetic field, the Lorentz force induced local micro-MHD convection flows on the electrode surface and the convection flows rolled inside the diffusion layer to blow off the concentration fluctuation. Thus, the crystal formation was blocked and the deposit surface was levelled.

Furthermore, in 1999, Bodea *et al.*<sup>97</sup> investigated the electrodeposition of Zn and the ferromagnetic metal, Fe, in a thin cell and found the symmetry breaking phenomenon for Fe deposition: when the magnetic field is applied parallel to the plane of the growth, the dense circular structures, which formed when without magnetic field, became a rectangular envelope parallel under the magnetic field, as shown in Fig. 1-14. However, no such magnetic field effect was found for Zn.

Bodea *et al.*<sup>97</sup> argued that the Fe deposit is ferromagnetic and that Fe ions have a magnetic moment. In the external magnetic field, the Fe deposit acquired a macroscopic magnetization which in turn produced an induced magnetic field that originated from the magnetic dipolars of Fe atoms. This induced magnetic dipolar effect exerts a remarkable influence on the deposit morphology.

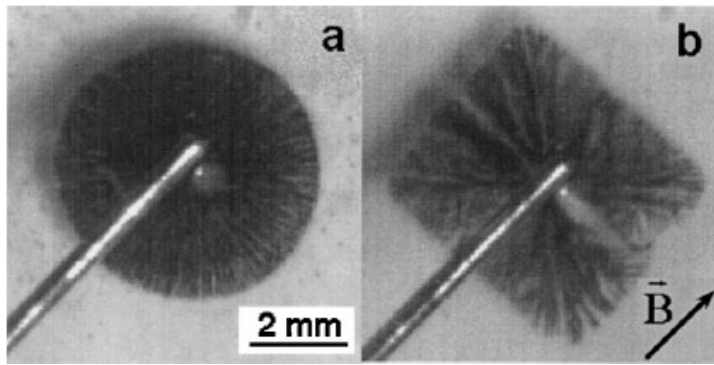


Figure 1-14 Electrodeposited Fe grown in a thin cell under (a) no magnetic field and (b) a parallel magnetic field of 0.2T (Fig. 1 in Ref. 97).

### Vertical field configuration

A magnetic field applied perpendicular to an electrode surface is believed to exert minimum MHD convection in the electrolyte and is thus expected to have negligible influence on the coating morphology<sup>98</sup>. However, as introduced in Section 1.3.5, the vertical magnetic field actually yields remarkable influence on the deposit morphology.

In 1999, when studying the metal corrosion in the perpendicular magnetic field, Aogaki<sup>96,99,100</sup> introduced the concept of the “micro-MHD effect.” He found that during the chemical dissolution, local galvanic cells are formed, which resulted in localized current flows that were subjected to the Lorentz force and brought about localized MHD convection. In consequence, microscopic vortices and macroscopic fluid rotation were induced, as demonstrated in Fig. 1-15(a).

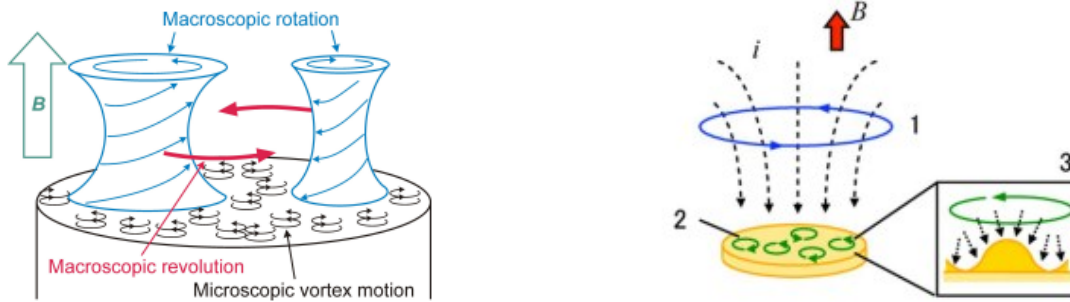


Figure 1-15 Illustration of (a) micro-MHD effect in corrosion (Fig. 4 in Ref. 99) and (b) vertical MHD effect in electrodeposition (Fig. 1 in Ref. 101).

The micro-MHD effect also exists in electrodeposition performed in the vertical magnetic field, as schematically depicted in Fig.1-15(b); non-equilibrium fluctuations on the electrode surface result in humps which produce micro-vortices near the surface above them<sup>101</sup> (No. 3 in Fig. 1-15(b)). The micro-MHD effect was claimed to have been indirectly observed as circular or network structures of the deposits<sup>101</sup>.

In addition, according to Aogaki<sup>99,101</sup>, the current direction on the electrode edge is not normal to the surface; the component of the current parallel to the surface interacts with magnetic field and causes a macroscopic flow around the electrode edge and gives rise to a rotating stream over the electrode (No. 1 in Fig. 1-16). This process is called the vertical MHD effect.

Aogaki *et al.*<sup>100</sup> showed by theoretical calculation that the micro-MHD effect was generated when the electrodeposition was conducted in the vertical magnetic field by forming numerous macroscopic and microscopic vortices parallel to the electrode surface. The micro-vortices interacted with the nonequilibrium fluctuations on the deposit surface and partially suppressed their nucleation process<sup>102</sup>. Consequently, a honeycomb-like pattern called ‘micro-mystery

circles' was predicted and experimentally ascertained in copper electrodeposition, as described in Fig.1-16.

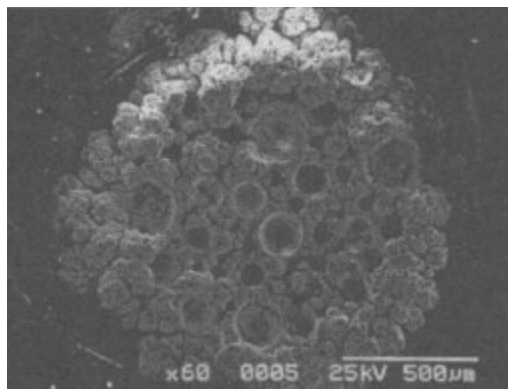


Figure 1-16 SEM image of Cu deposited in the vertical magnetic field of 7T, showing the “micro-mystery circles” (Reproduced from Ref. 99).

Matsushima *et al.*<sup>103</sup> explained the suppression of the nucleation on the electrode that the spiraling adatom flux around the nucleus generated from the vertical magnetic field prolonged the residence time of the adatoms on the deposit surface and thus inhibited the crystal growth.

#### **Other field arrangement and results**

Ganesh *et al.*<sup>48</sup> electrodeposited Ni from a sulphamate bath in the magnetic field of 1T applied at a 45° angle to the cathode surface. These authors observed a modified deposit surface with a fine grain structure, as pictured in Fig. 1-17. In Fig. 1-17(b), the deposited Ni obtained in the magnetic field consisted of some micro-scaled domains, which in turn are made of smaller domains. Furthermore, tiny nano-sized spherical particles gathered in the domain boundaries. The authors concluded from a closer view of the deposit (shown in Fig. 1-17(c)) that fresh nucleation and growth happened predominantly at the domain boundaries, and they believed that

these fine grains were resulted from the increased mass transfer rate and reduced concentration polarization induced by the external magnetic field.

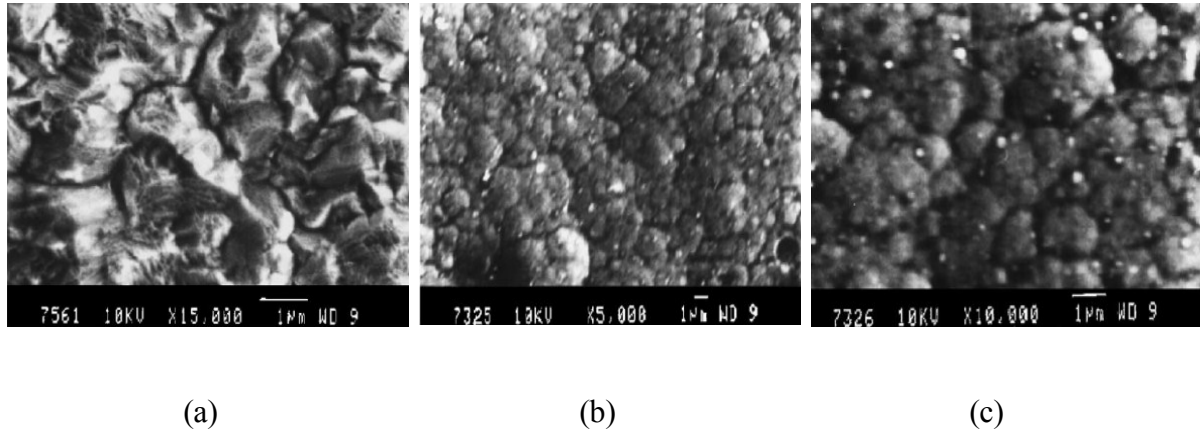


Figure 1-17 SEM images of the Ni deposited in a magnetic field arranged at a 45° angle: (a) no field; (b) in the 1T magnetic field; (c) higher magnification view of (b) (Fig. 2 in Ref. 48).

### 1.5.7 Structure change of electrodeposition in the magnetic field

#### 1.5.7.1. Magnetic anisotropy

Magnetic anisotropy means that the magnetic properties differ from the directions in which they are measured<sup>104</sup>.

For ferromagnetic materials, several types of magnetic anisotropy have been discovered: crystal anisotropy or magneto-crystalline anisotropy, shape anisotropy, stress anisotropy, induced anisotropy and exchange anisotropy.

Among all the anisotropies mentioned above, only the crystal anisotropy is intrinsic to the material, and each anisotropy can be predominant in material under certain circumstances<sup>104</sup>. In the present review, only the crystal and shape anisotropy are introduced as follows.

### a. Magneto-crystalline anisotropy

Most of the magnetism of a material is from its electrons. The electron has two distinct sources of magnetic moment, an orbital magnetic moment and a spin magnetic moment.

The physical origin of crystal anisotropy is believed to be the spin-orbit coupling<sup>104-106</sup>. When an external magnetic field was applied to ferromagnetic material, both orbital and spin moment of the electron tend to reorient. However, the orbital magnetic moment is firmly related to the crystal lattice and the resistance to orbiting direction alternation is strong. On the other hand, the spin moment of the electron, only coupled with orbital moment, can be reoriented more easily because only the resisting force from the spin-orbit coupling is required to be overcome. For different magnetic field directions relative to the lattice structure, the resisting force of the spin-orbit coupling to oppose the spin moment direction rotation varies, and there exists a direction along which the magnetization is the easiest. This direction is termed the easy magnetic axis. For example,  $\langle 100 \rangle$  and  $\langle 111 \rangle$  directions are easy magnetic axes for Fe and Ni, respectively.

The crystal anisotropy energy for cubic crystal is expressed as<sup>104</sup>:

$$E = K_0 + K_1(\alpha_1^2\alpha_2^2 + \alpha_2^2\alpha_3^2 + \alpha_3^2\alpha_1^2) + K_2(\alpha_1^2\alpha_2^2\alpha_3^2) + \dots \quad 1-(47)$$

Where  $K_0, K_1, K_2 \dots$  are constants that vary with material and temperature. At 20 °C, for Fe,  $K_1 > 0$  and for Ni,  $K_1 < 0$ .

Form 1-(47) it can be shown that  $\langle 100 \rangle$  is the easy magnetic axis for Fe and for Ni the easy axis is  $\langle 111 \rangle$ .

## **b. shape anisotropy**

For a polycrystalline material, even though there is no crystal anisotropy, its shape alone can be a source of magnetic anisotropy, i.e., the magnetization along long axis is easier than that along a short axis<sup>104</sup>.

According to magnetization theory<sup>104-106</sup>, the shape anisotropy is attributed to the dipole-dipole interaction. The sum of the magnetic energy of all the dipoles from a specimen depends on its shape.

### **1.5.7.2 Results of structure change in magnetic field and the proposed mechanisms**

Much research has been performed on the deposit structure in magnetic field. In 1954, Yang<sup>107</sup> studied the magnetic field influence on the Ni, Fe and Co. He concluded that the magnetic field had no significant effect on the preferential orientations of these metals. In 1986, Chiba *et al.*<sup>85</sup> observed the texture variation of Ni deposited under the magnetic field. The effect appeared to be most pronounced at low current densities, where the influence of the magnetic field would be larger than that of the electric field. These authors suggested that the magnetic field could modify the crystal growth orientations in relation to the easy magnetic axis. Many other research groups also reported structure changes when electrodeposition was carried out in magnetic field<sup>43,48,81,89,92,108</sup>. For instance, Devos *et al.*<sup>81,92</sup> observed that in Ni deposition with a pure Watts bath at a low cathodic potential, the <211> preferred orientation became dominant as compared to the <100> texture. When the additive BD was added into the Watts bath, the <110> texture turned increasingly intense as the magnetic flux density raised from 0 to 0.9T.

Several mechanisms have been proposed to describe the structure evolution of electrodeposition in the external magnetic field.

In 1965, Pangarov<sup>109</sup> put forward the competitive nucleation theory to explain the texture formation in electrodeposition. The theory posited that the overpotential to form two-dimensional nuclei was different for various planes. This gave rise to different nucleation rates of the planes, and the planes having the higher rates could dominate the texture evolution. However, due to the fact that the overpotential for nucleation is much lower compared to that for deposition operating<sup>110</sup>, nucleation could happen to different planes in similar probabilities under the high operating overpotential. Thus the nucleation rate is unlikely to be the reason for the texture formation. Also, experimental results reported disagreement with the model<sup>111</sup>.

In 1963, Reddy suggested another model named geometrical selection<sup>112</sup>. The main point of this theory is that the texture formation is determined by both the different growth rates of different planes and the deposit's surface morphology. This theory still cannot explain some experimental observations, e.g., the surface morphology of the Fe deposit<sup>110</sup>.

In 1993, Li and Szpunar<sup>108</sup> developed another model to explain the texture development during Fe electrodeposition. These authors had demonstrated with experimental results that the electrodeposited iron without the external magnetic field had  $\{110\}\langle uvw \rangle$  texture, and they used the opinion of Walter and Dunn<sup>113</sup> that had interpreted the grain growth in terms of surface energy.

According to Walter and Dunn<sup>113</sup>, when two neighboring grains grow together, the equilibrium condition is given by the following equation:

$$\cos \varphi = \frac{\gamma_B - \gamma_A}{\gamma_{AB}} \quad 1-(48)$$

Where  $\gamma_A$  and  $\gamma_B$  are surface energies of two neighbouring grains A and B,  $\gamma_{AB}$  is the grain boundary energy between them, as illustrated in Fig. 1-18.

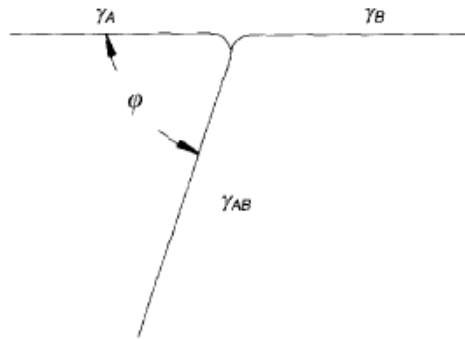


Figure 1-18 Schematic view of the equilibrium of two neighbouring grains with different surface energies (Fig. 4 in Ref. 108).

If  $\gamma_A < \gamma_B$ , Equation 1-(48) yields  $\varphi < 90^\circ$ , which means grain A grows preferentially. If grain B grows between two similar grains with surface energy  $\gamma_A$ , it will be covered by them as the growing process proceeds. Therefore, in the electrodeposition process, grains with the lower surface energy grow preferentially. Fig. 1-19, which clearly shows that grain 1 was covered by grain 2 and 3, is an example of this conclusion.

In Ref. 114 and 115, the surface energies of different crystallographical planes and the interfacial energy of the grain boundaries of iron have been estimated. The result implied that of all the crystallographic planes of iron, the  $\{110\}$  planes have the lowest surface energy. Based on

this work, Li and Szpunar deduced that the surface energy is responsible for the formation of the  $\{110\}\langle uvw \rangle$  texture of Fe in the electrodeposition when the magnetic field is absent<sup>108</sup>.

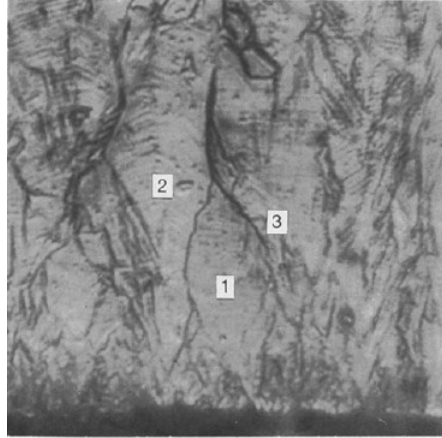


Figure 1-19 SEM image of the cross section of Fe deposit showing the coverage of grain 1 (Fig. 3 in Ref. 108).

When the magnetic field parallel to the electrode surface was applied, a  $\{110\}\langle 001 \rangle$  texture was recorded in Fe deposition<sup>108</sup>. Li and Szpunar explained this phenomenon with the magnetic energy of the grains. They maintained that the Fe grain in the magnetic field gained the magnetic energy because of its magnetic anisotropy. The magnetic anisotropy energy is expressed in Eq. 1-(47). As was mentioned above, from Eq. 1-(47), for Fe, the easy magnetic axis is  $\langle 001 \rangle$ , i.e., the magnetic anisotropy energy is the lowest along  $\langle 001 \rangle$  direction. Hence, in the presence of the parallel magnetic field, both the surface energy and the magnetic energy determined the development of the Fe deposit texture<sup>108</sup>.

Later in 1997, Li and Szpunar<sup>110, 116</sup> made Monte Carlo simulations as well as experiments, assuming that the crystalline growth process kept minimizing the system's free energy (the sum

of the grains' surface energy and the magnetic anisotropy energy) and created the lattice texture. The simulation result demonstrated that for Fe deposited in the magnetic field, the  $\{110\}\langle 00\rangle$  texture has the highest proportion among all the  $\{110\}\langle uvw\rangle$  components, i.e., the grains of the ferromagnetic material Fe tend to grow along the easy axis of magnetization. This result was in agreement with the experiment investigation.

Furthermore, the effects of other deposition parameters, current density, solution pH and bath temperature, were also examined by Li and Szpunar<sup>110,116</sup> based on the work of Petch<sup>117</sup> and Okamoto et al<sup>118</sup>. According to Petch<sup>117</sup>, iron's surface energy can be significantly lowered by the hydrogen adsorption, and this drop in surface energy may differ from crystallographic planes. Okamoto *et al.*<sup>118</sup> theoretically showed that loosely packed planes possess higher hydrogen adsorption abilities than closely-packed planes, i.e., the surface energy can be lowered by hydrogen adsorption at different rates for different crystal planes. Using Monte Carlo simulation method, Li and Szpunar<sup>116</sup> demonstrated that as the hydrogen concentration increased, the lowest surface energy plane of iron changed from  $\{110\}$ , through  $\{111\}$ , to  $\{311\}$  plane, and the axis of fibre texture varied in the sequence of  $\langle 110\rangle$ ,  $\langle 111\rangle$  and  $\langle 311\rangle$ . With this result, it is reasonable to infer that because the current density affects the cathodic overpotential for hydrogen discharge (increasing current density raises the hydrogen adsorption), the fibre texture is expected to evolve during the current density increase in the following order:  $\langle 110\rangle$   $\langle 111\rangle$   $\langle 311\rangle$ . Similarly, the solution pH and temperature change can also influence the axis of the fibre texture because pH is related to the hydrogen ion concentration and the hydrogen adsorption, and temperature can alter the hydrogen discharge overpotential: an increase in temperature lowers the hydrogen overpotential.

Li and Szpunar also conducted experimental tests to confirm their simulation results, and a positive correlation between the experiment and simulation was obtained<sup>116</sup>.

On the other hand, in the investigations of Ni deposition in the magnetic field, Devos *et al.*<sup>92</sup> explained the <110> texture intensity increase as the magnetic field turned stronger and maintained that the magnetic field had provoked an increase of the diffusion flux of definite inhibiting species, such as BD (additive), which produced Ni(OH)<sub>2</sub> in close proximity to the cathode surface and facilitated specific modes of growth. This explanation is consistent with Li and Szpunar's model<sup>110,116</sup> if considering that the Ni(OH)<sub>2</sub> acts similar to hydrogen to block the electrode surface and change the surface energy.

Also, Ganesh *et al.*<sup>48</sup> carried out an XRD test in nickel deposition in sulphamate bath under a 45° placed magnetic field and found that though the (111) plane was still predominant, the intensity of the (200) plane increased in the presence of the magnetic field. The explanation for this result was that the (111) plane dominance corresponded to the dictatorship of the electric field, while the increase in the diffraction intensity of the (200) plane indicated the influence of the magnetic field on the preferred orientation.

## 1.6 References

- 1 M. Schlesinger, M. Paunovic, Modern Electroplating, John Wiley & Sons, Inc. 2010.
- 2 R. Orinakova, A. Turonova, D. Kladekova, M. Galova and R. M. Smith, Journal of Applied Electrochemistry (2006) 36:957–972.
- 3 E.M. Oliveira, G.A. Finazzi, I.A. Carlos, Surface & Coatings Technology 200 (2006) 5978 –

5985.

4 M. Moharana, A. Mallik, *Electrochimica Acta* 98 (2013) 1–10.

5 L. M. Graham, S. Cho, S. K. Kim, M. N. and S. B. Lee, *Chem. Commun.*, 2014, 50, 527—  
529.

6 N. V. Sotskaya, L. V. Saprionova, and O. V. Dolgikh, *Protection of Metal and Physical  
Chemistry of Surfaces*, Vol. 50 No. 1 2014.

7 S. Hartwig and C. Klages, *Journal of The Electrochemical Society*, 161 (5) D243-D247 (2014).

8 E. Tóth-Kádár, L. Péter, T. Becsei, J. Tóth, L. Pogány, T. Tarnóczy, P. Kamasa, I. Bakonyi,  
G. Láng, Á. Cziráki, and W. Schwarzacher, *Journal of The Electrochemical Society*, 147,  
(9) 3311-3318 (2000).

9 I. Milošev and M. Metikoš-Huković, *J. Appl. Electrochem.* 29 (1999) 393.

10 B. H. Prescott, *Trans. Inst. Met. Finish.*, 36, 93 (1959).

11 A. Brenner, *Electrodeposition of Alloys I* (Academic Press, New York, 1963).

12 J.R. Roos, J.P. Celis, C. Buelens and D. Goris, *Proc. Metall.* 3 (1984) 177.

13 K. Vu Quang, E. Chassaing, B. Le Viet, J. P. Celis, J. R. Roos, *Met. Finish.*, 10, 25(1985).

14 C. Madore, Ph.D. Dissertation, *Ecole Polytechnique Federale de Lausanne, Switzerland*  
(1993).

15 J. Toth, L.F. Kiss, E. Toth-Kadar, A. Dinić, V. Pierron-Bohnes, I. Bakonyi, *Journal of*

- Magnetism and Magnetic Materials 198-199 (1999) 243-245.
- 16 E. Chassaing, K. VU Quang, *J. of App. Electrochem.* 17 (1987) 1267-1280.
  - 17 R. Y. Ying, P. K. Ng, *J. Electrochem. Soc.* 135, 2964 (1988).
  - 18 E. J. Podlaha, C. Bonhôte, and D. Landolt, *Electrochim. Acta*, 39, 2649 (1994).
  - 19 S. Rode, C. Henminot, and M. Matlosz, *J. of Electrochem. Soc.*, 152 (4) C248-C254 (2005).
  - 20 L. Bonou, Y. Massiani, J. Crousier, *British Corrosion Journal*, 29, 201 (1994).
  - 21 L. P. Bicelli, B. B., C. Mele, L. D'Urzo, *Int. J. Electrochem. Sci.*, 3 (2008) 356 – 408.
  - 22 S.K. Ghosh, A.K. Grover, G.K. Dey, M.K. Totlani, *Surface & Coatings Technology* 126  
2000. 48-63.
  - 23 X. Cui, W. Chen *J. Electrochem. Soc.*, 155 (9) K133-K139 (2008).
  - 24 T. A. Green, A. E. Russell, S. Roy, *J. Electrochem. Soc.*, Vol. 145, No. 3, March 1998.
  - 25 A. J. Bard, L. R. Faulkner, *Electrochemical Methods*, 2<sup>nd</sup> edition, p45.
  - 26 H. D. Hine, W. B. Cooley, *Transactions of the American Electrochemical Society*, 61,  
48 (1925).
  - 27 P. Bradley, S. Roy, D. Landolt, *Journal of the Chemical Society, Faraday Transactions*,  
92, 4015 (1996).
  - 28 I. Mizushima, M. Chikazawa and T. Watanabe, *J. Electrochem. Soc.* 143 (1996) 1978.
  - 29 R. B. P. Crawford, R. D. Snyder, U.S. Patent Number 1,750,092 (1930).
  - 30 L. C. Melo, P. de Lima-Neto, A. N. Correia, DOI 10.1007/s10800-010-0251-2.
  - 31 S. K. Pannikar, T. L. Char, *Journal of the Electrochemical Society, Japan*, 25, E121, (1957).

- 32 A. R.Despic, V. D. Jovic, S. Spaic, Journal of the Electrochemical Society, 136, 6 (1989).
- 33 M. Ishikawa, H. Enomoto, M. Matsuoaka, C. Iwakura, Electrochimica Acta, 40, 1663 (1995).
- 34 M. Pushpavanam, K. Balakrishnan, Journal of Applied Electrochemistry, 26, 1065 (1996).
- 35 S. Rode, C. Henninot, and M. Matlosz, J. of Electrochem. Soc., 151 (6) C405-C411 (2004).
- 36 P. G. Daniele, G. Ostacoli, O. Zerbinati, S. Sammartano, and A. D. Robertis, Trans. Met. Chem., 13, 87 (1988).
- 37 B. W. Parry and F. W. Dubois, J. Am. Chem. Soc., 74, 3749 (1952).
- 38 D. Mastropaolo, D. A. Powers, J. A. Potenza, and H. J. Schugar, Inorg. Chem., 15, 1444 (1976).
- 39 S. Roy, M. Matlosz, and P. Landolt, This Journal, 141, 1509 (1994).
- 40 K. Murase, T. Honda, T. Hirato, and Y. Awakura, Metallurgical and Materials Transactions B, 29B, DECEMBER 1998-1197.
- 41 T.Z. Fahidy, J. Appl. Electrochem. 13 (1983) 553.
- 42 T. Z. Fahidy, Progress in Surface Science 68 (2001) 155-188.
- 43 H. Matsushima, T. Nohira, I. Mogi, Y. Ito, Surface and Coatings Technology 179 (2004) 245–251.
- 44 S. Molokov, R. Moreau, H.K. Moffatt (eds.), Magnetohydrodynamics – Historical Evolution and Trends, 391-407. 2007 Springer.

- 45 M. Uhlemann, K. Tschulik, A. Gebert, G. Mutschke, J. Frohlich, A. Bund, X. Yang, and K. Eckert, *Eur. Phys. J. Special Topics* 220 , 287–302 (2013).
- 46 G. Hinds, F. E. Spada, J. M. D. Coey, T. R. Ni Mhiochain, and M. E. G. Lyons, *J. Phys. Chem. B* 2001, 105, 9487-9502.
- 47 O. Devos, O. Aaboubi, J.P. Chopart, C. Gabrielli, B. Tribollet, *J. Phys. Chemistry A* 104 , 1544 (2000).
- 48 V. Ganesh, D. Vijayaraghavan, V. Lakshminarayanan, *Applied Surface Science* 240 (2005) 286–295.
- 49 G. Hinds, J. M. D. Coey, M. E. G. Lyons, *Electrochemistry Communications* 3(2001) 215-218.
- 50 M. S. Tillack and N. B. Morley, *MAGNETOHYDRODYNAMICS*, McGraw Hill, 14th Edition, 1998.
- 51 D. T. J. Hurle, R. W. Series, in: D. T. J. Hurle (Ed.), *Handbook of Crystal Growth*, North Holland, Amsterdam, vol. 2A, 1994, Chapter 5.
- 52 O. Y. Gorobets, V. Y. Gorobets, D. O. Derecha, and O. M. Brukva, *J. Phys. Chem. C* 2008, 112, 3373 – 3375.
- 53 K. Tschulik , J. A. Koza, M. Uhlemann, A. Gebert, L. Schultz, *Electrochemistry Communications* 11 (2009) 2241–2244.
- 54 K. M. Grant, J. W. Hemmet, H. S. White, *Electrochem. Commun.* 1 (1999) 39.
- 55 Y. Tanimoto, H. Yano, S. Watanabe, A. Katsuki, W. Duan, M. Fujiwara, *Bull. Chem. Soc. Jpn.* 73 (2000) 867.
- 56 M. S. Tillack and N. B. Morley, *Magnetohydrodynamics*, McGraw Hill, 14<sup>th</sup> Edition, 1998.
- 57 S. Mohanta and T. Z. Fahidy, *Electrochim. Acta* 21 (1976) 25.

- 58 E. Tronel-Peyroz and A. Olivier, *Compt. Rendus Acad. Sci.* 278 (1974) 997.
- 59 E. Tronel-Payroz, Thesis Doctorat d'Etat, Rheims (1978).
- 60 E. Tronel-Payroz, A. Olivier, T. Z. Fahidy and D. Laforgue-Kantzer, *Electrochim. Acta* 25 (1980) 441.
- 61 A. Olivier, Thesis Doctorat d'Etat, Rheims (1979).
- 62 J. Lielmezs and H. Aleman, *Thermochim. Acta* 18 (1977) 315.
- 63 J. Lielmezs, *Techn. Apskats* 79 (1977) 2.
- 64 Idem, *Bioelectrochem. Bioenerg.* 5 (1978) 285.
- 65 O. Lioubashevski, E. Katz, I. Willner, *J. Phys. Chem. B* 108 (2004) 5778.
- 66 M. Uhlemann, A. Krause, J.P. Chopart, A. Gebert, *J. Electrochem. Soc.* 152 (2005) C817.
- 67 T. Z. Fahidy, *Electrochim. Acta* 1973, 18, 607.
- 68 R. Aogaki, K. Fueki, and T. Mukaibo, *Denki Kagaku*, 43, 509 (1975).
- 69 R. Aogaki, K. Fueki, and T. Mukaibo *Denki Kagaku*, 44, 89 (1976).
- 70 A. OLIVIER, J.P. CHOPART and J. DOUGLADE, *J. Electroanal. Chem.*, 217 (1987) 443-452.
- 71 O. Aaboubi, J. P. Chopart, J. Douglade, A. Olivier, C. Gabrielli and B. Tribollet *J. Electrochem. Soc.*, 137, 1796, 1990.
- 72 L. N, Gao *J Phys Chem B* (1999) 103:5832.
- 73 Lioubashevski O, Katz E, Willner I (2004) *J Phys Chem B* 108: 5778.
- 74 Uhlemann M, Krause A, Chopart JP, Gebert A (2005) *J Electro-chem Soc* 152:C817.
- 75 O. Aaboubi & J.-P. Chopart, *ECS Transactions*, 25 (32) 27-34 (2010).
- 76 O. Aaboubi, Jacques Douglade, *Journal of Electroanalytical Chemistry* 693 (2013) 42–50.
- 77 P. Fricoteaux, B. Jonvel, and J.-P. Chopart, *J. Phys. Chem. B* 2003, 107, 9459 – 9464.

- 78 S. Legeai, M. Chatelut, O. Vittori, J. Chopart, O. Aaboubi, *Electrochimica Acta* 50 (2004) 51–57.
- 79 J.-P. Chopart, O. Aaboubi, E. Merienne, A. Olivier, J. Amblard, *Energy Conversion and Management* 43 (2002) 365.
- 80 P. Fricoteaux, A. Olivier and R. Delmas, *J. Electrochem. Soc.* 139 (1992) 1096.
- 81 O. Devos, O. Aaboubi, J.-P. Chopart, E. Merienne, A. Olivier, and J. Amblard, *J. Electrochem. Soc.*, Vol. 145, No.12, 4135, 1998.
- 82 H. Matsushima, T. Nohira and Y. Ito, *Electrochemical and Solid-State Letters*, 7 (8) C81-C83 (2004).
- 83 A. Krause, C. Hamann, M. Uhlemann, A. Gebert, L. Schultz, *Journal of Magnetism and Magnetic Materials* 290–291 (2005) 261–264
- 84 J. A. Koza, F. K., M. Uhlemann, J. McCord, C. Mickel, A. Gebert, S. Baunack, L. Schultz, *Electrochimica Acta* 55 (2010) 819–831.
- 85 A. Chiba, T. Niimi, H. Kitayama and T. Ogawa, *Surf Coat. Tech.* 29 (1986) 347.
- 86 A. Chiba and T. Ogawa, *Chem. Abstr.* 108 (1988) 175888.
- 87 H. Matsushima, Y. Fukunaka, Y. Ito, A. Bund, W. Plieth, *Journal of Electroanalytical Chemistry* 587 (2006) 93-98.
- 88 J. Koza, M. Uhlemann, A. Gebert, L. Schultz, *J Solid State Electrochem* (2008) 12:181-192.
- 89 A. Ispas, H. Matsushima, W. Plieth, A. Bund, *Electrochimica Acta* 52 (2007) 2785-2795.
- 90 A. Bund, S. Koehler, H.H. Kuehnlein, W. Plieth, *Electrochimica Acta* 49 (2003) 147–152.
- 91 M. Paunovic, M. Schlesinger (Eds.), *Fundamentals of Electrochemical Deposition*, Wiley, New York, 1998.
- 92 O. Devos, A. Olivier, J. P. Chopart, a . Aaboubi and G. Maurin, *J. Electrochem. Soc.*, Vol.

- 145 (2) 1998, 401.
- 93 I. Tabakovic, S. Riemer, V. Vas'ko, V. Sapozhnikov, and M. Kief, *Journal of The Electrochemical Society*, 150 (9) C635-C640 (2003).
- 94 A. Krause, M. Uhlemann, A. Gebert, L. Schultz, *Electrochimica Acta* 49 (2004) 4127–4134.
- 95 M. Uhlemann, A. Krause, J. P. Chopart, and A. Gebert, *Journal of The Electrochemical Society*, 152 12 C817-C826 2005.
- 96 K. Shinohara, R. Aogaki, *Electrochemistry* 67 (1999) 126.
- 97 S. Bodea, L. Vignon, R. Ballou, P. Molho, *Phys. Rev. Lett.* 83 (1999) 2612.
- 98 M. Yamaguchi, Y. Tamimoto, *Magneto-Science*, Kodansha Ltd. and Springer-Verlag Berlin Heidelberg 2006.
- 99 R. Aogaki, *Magnetohydrodynamics* 37, 143–150 (2001).
- 100 R. Aogaki, *Magnetohydrodynamics* 39, 453–460 (2003).
- 101 I. Mogi, R. Morimoto, R. Aogaki & K. Watanabe, *Scientific Reports* | 3 : 2574 | DOI: 10.1038/srep02574, 2013.
- 102 A. Sugiyama, M. Hashirideb, R. Morimotob, Y. Nagaib, R. Aogakic, *Electrochimica Acta* 49 (2004) 5115–5124.
- 103 H. Matsushima, A. Ispas, A. Bund, B. Bozzini, *Journal of Electroanalytical Chemistry* 615 (2008) 191–196.
- 104 B. D. Cullity, C. D. Graham, *Introduction to Magnetic Materials*, John Wiley & Sons, 2<sup>nd</sup>

- edition, 2009.
- 105 S. Chikazumi, *Physics of Ferromagnetism*, second edition, Clarendon Press, Oxford, 1997.
  - 106 J. M. D. Coey, *Magnetism and Magnetic Materials*, Cambridge University Press, 2009.
  - 107 L. Yang, *J. Electrochem. Soc.*, 101, 456 (1954).
  - 108 D. Y. Li, J. A. Szpunar, *J. Matt. Sci.* 28 (1993) 5554-5559.
  - 109 N. A. Pangarov, *J. Electroanal. Chem.* 9 (1965) 70-85.
  - 110 D. Y. Li and J. A. Szpunar, *Electrochimica Acta*, Vol. 42, No. 1, 37-45, pp. 1997.
  - 111 G. C. Ye and D. N. Lee, *Plating and Surface Finishing*, A, 60 (1981).
  - 112 A. K. N. Reddy, *J. Electroanal. Chem.* 6, 141 (1963).
  - 113 J.L. WALTER and C. G. DUNN, *Acta. Metall.* 8 (1960) 497.
  - 114 L. E. Murr, *Interfacial Phenomena in Metals and Alloys*, Addison-Wesley, 1975.
  - 115 J. K. MACKENZIE, A. J. W. MOORE and J. F. NICHOLAS, *J. Phys. Chem. Solids* 23 (1962) 185.
  - 116 D.Y.LI and J. A. SZPUNAR, *Electrochimico Acta*, Vol. 42, No. 1, 47-60, 1997.
  - 117 N. J. Petch, *Phil. Mag.* 1, 331 (1956).
  - 118 G. Okamoto, J. Horiuti and K. Hirota, *Sci. Papers Inst. Company*, New York (1977). *Phys. Chem. Res. (Tokyo)* 29, 223 (1936).

## **Chapter 2 Experimental**

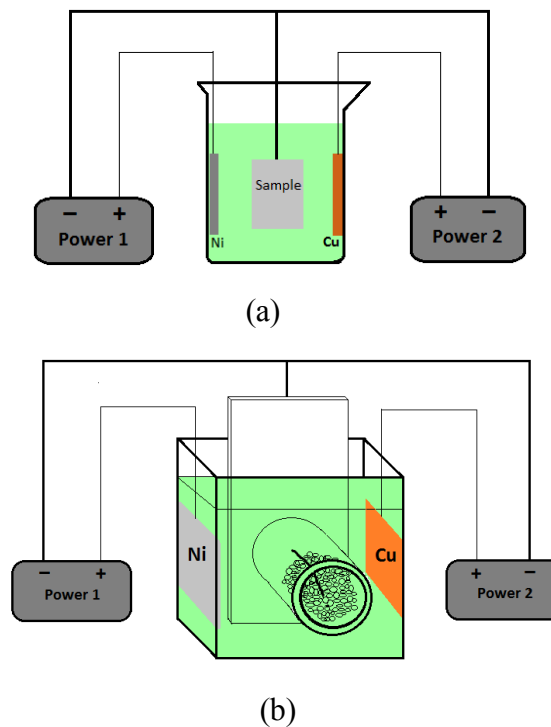
## 2.1 Ni-Cu Codeposition

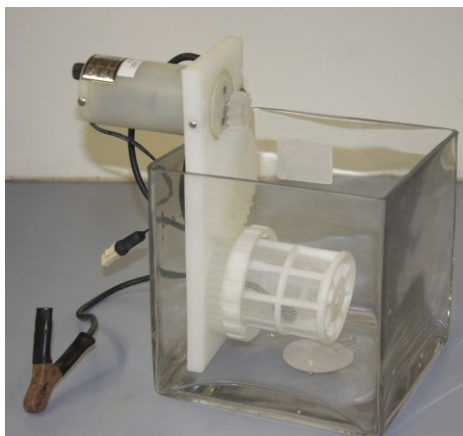
### 2.1.1 Experimental setup and electrolytes

#### Experimental setup

Nickel-copper coating layers were electroplated galvanostatically with two DC power suppliers under the constant current mode. Plates of nickel and copper were connected to the positive ends of the power suppliers to serve as anodes.

The electroplating experiments included beaker setup plating and barrel plating. In the beaker plating, the deposition tests were conducted in a 300 ml beaker; in the barrel plating, the electrolyte was filled in a 3-liter glass tank, and a plastic barrel with a diameter of 6 cm was driven by a motor to rotate at 8 rpm. Fig. 2-1 depicts the experimental setup for the two kinds of plating tests.





(c)

Figure 2-1 Experimental setup for (a) beaker plating, (b) barrel plating and (c) barrel plating device.

### **Electrolytes**

The electrolyte solution in the beaker setup plating contained 0.4M  $\text{NiSO}_4 \cdot 6\text{H}_2\text{O}$ , 0.008M  $\text{CuSO}_4$ , 0.3M tri-sodium citrate ( $\text{Na}_3\text{C}_6\text{H}_5\text{O}_7 \cdot 2\text{H}_2\text{O}$ ), 0.00069M dodecyl sulfate (SDS), 0.0027M saccharin and 0.005M  $\text{NiCl}_2$ .

In barrel plating, there were 0.3M  $\text{NiSO}_4 \cdot 6\text{H}_2\text{O}$ , 0.006M  $\text{CuSO}_4$ , 0.3M tri-sodium citrate ( $\text{Na}_3\text{C}_6\text{H}_5\text{O}_7 \cdot 2\text{H}_2\text{O}$ ), 0.00069M dodecyl sulfate (SDS), 0.0027M saccharin and 0.005M  $\text{NiCl}_2$ . All chemicals were analytical reagent-grade. Deionized water was used to prepare the electroplating solutions.

### **2.1.2 Sample preparation**

In the beaker plating setup, low-carbon steel discs with a diameter of 23.5 mm were used as the plating substrate, the backs of which were sealed using insulating glue.

In the barrel plating setup, the samples were  $1 \times 10 \times 0.5$  mm low-carbon steel squares. Also, the 40 pieces of low carbon steel discs mentioned above were used for the beaker plating setup. Each was further cut into four small pieces and filled into the barrel to ensure good random electric contact with the cathode tip inside the barrel.

All the plating substrates were mechanically polished before deposition, first with 1200-grit SiC sandpaper, then with the slurry of  $0.05 \mu\text{m}$   $\text{Al}_2\text{O}_3$  powder on a polishing cloth. After polishing but before plating, the substrates for the deposition were pre-treated through degreasing and activation processes.

In degreasing, samples after mechanical polishing were cleaned by ultrasonication in acetone. In the activation process, the degreased samples were soaked in 15%  $\text{H}_2\text{SO}_4$  solution for 2 minutes.

### **2.1.3 Experimental procedures**

In beaker plating, the bath temperature was maintained at two different values,  $40 \pm 2^\circ\text{C}$  or  $56 \pm 2^\circ\text{C}$ , to test the temperature dependence of the coating composition. The current density was controlled at  $3.92 \text{ mA/cm}^2$ . The ratio of the current densities on the Ni and Cu anode was controlled to adjust the coating composition. The electrolyte pH was 4.60, agitation was provided by a magnet stirring bar at a rate of 350 rpm, and the plating time was set at 12 hours.

In barrel plating, the plating temperature was  $30 \pm 2^\circ\text{C}$ , and the electrolyte pH was controlled at two different values, 4.5 and 5.1. Plating time was 5 to 12 hours, respectively. The current density was controlled to be at  $2.13$  and  $2.66 \text{ mA/cm}^2$ , respectively, during plating.

The different current density ratios on the Ni and Cu anode could yield different compositions in the deposits.

#### **2.1.4 Characterization**

After the deposition, the samples were characterized on a JEOL (JSM-6301FXV) field emission scanning electron microscope (SEM) for morphology observation; on the ZEISS (EVO –MA15) SEM with energy dispersive X-ray spectroscopy (EDX) to determine chemical compositions; on a Rigaku-UltimaIV X-ray diffractometer (XRD) for structure determination using Cu K $\alpha$  radiation with a wavelength of 1.54059Å and 2 $\theta$  range of 10° to 110°; on Bruker D8 Discover 2-dimensional XRD equipment with 2-dimensional detector Vantec200 for residual stress measurement; on a nanoindenter (Fischerscope H100 Micro Hardness Tester with Berkovich tip) to measure the Yong's modulus; and on a Gamry Reference 600 electrochemical work station for electrochemical characterization.

## **2.2 Nickel plating in constant magnetic field**

### **2.2.1 Experimental setup and electrolyte**

#### **Experimental setup**

Nickel was electrodeposited galvanostatically in a constant current mode with a 3-electrode system. A nickel foil of 4×8 mm was employed as the counter electrode. The reference electrode was a standard calomel electrode (SCE). The working electrode (electroplating substrate) was a 3×3 ×0.7 mm copper square. The experiment setup is shown in Fig. 2-2. A

specially designed nylon cup was used in the experiment. The sample was placed in the middle of a hole in the nylon cup. A pair of permanent magnet sets was mounted onto an austenitic stainless steel frame, which was installed around the sample and the hole in the nylon cup. The diameter of the hole was 6 mm and the distance between the pair of magnet sets was 15 mm. Each magnet set consisted of four cylindrical magnets which were magnetized parallel to their axes. With such an arrangement, the magnetic field inside the hole was measured to be 0.18T.

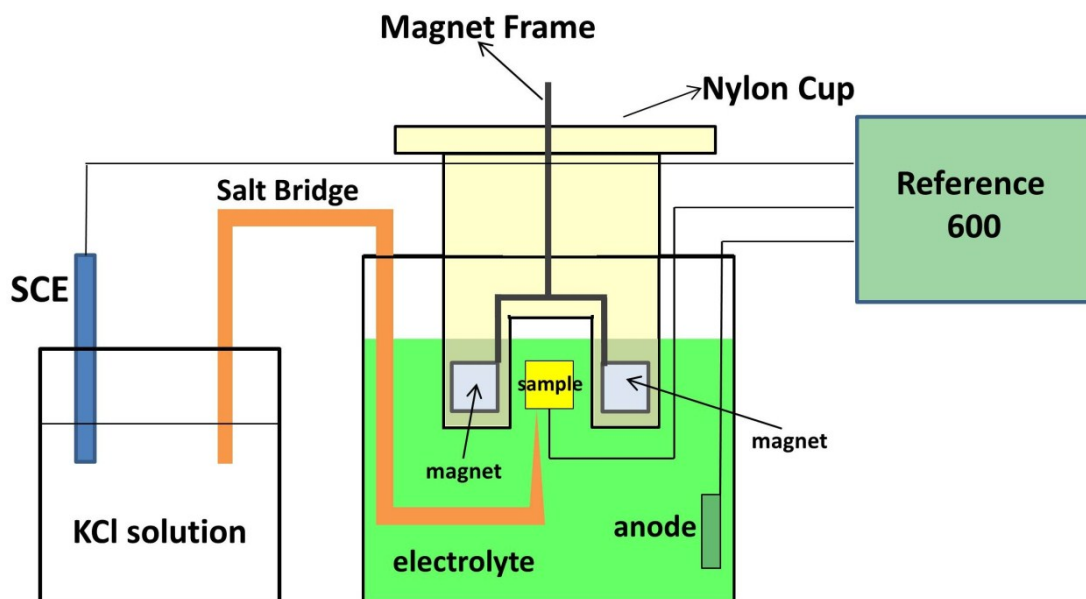


Figure 2-2 Schematic diagram of the electrolysis system in the presence of the magnetic field.

## **Electrolyte**

The electrolyte solution contained 0.05M NiSO<sub>4</sub>·6H<sub>2</sub>O, 0.1M boric acid and 0.1M sodium sulfate anhydrate as the supporting electrolyte. The solution pH was maintained at 4.00. All chemicals were analytical reagent-grade. Deionized water was used in preparing the electroplating solutions.

### **2.2.2 Sample preparation**

The copper plate of 0.7 mm thickness was cut into 3×3 mm squares. The squares were mechanically polished, first with 1200-grit SiC sandpapers, then with the slurry of 0.05 μm Al<sub>2</sub>O<sub>3</sub> powders on polishing cloth. The square-shaped Cu sheet after polishing was glued on the conductive sample frame as shown in Fig. 2-2.

### **2.2.3 Experimental procedures**

The electroplating experiments were conducted at 22±2°C. No agitation was provided except for one experiment that was performed to determine the influence of forced convection on the deposit structure and morphology, in which a 9.3Hz mechanical vibration was introduced during the plating.

The electrodeposition experiments were performed under the current density of 6.7 mA/cm<sup>2</sup>. The deposition time varied from 100 seconds to 40 minutes. The chronopotentiometry curves were recorded during the deposition.

#### **2.2.4 Characterization**

The surface morphologies of the samples were observed with a JEOL (JSM-6301FXV) field emission SEM and AFM (MFP-3D, Asylum Research); the crystal structures of the deposits were detected with a Rigaku-UltimaIV X-ray diffractometer (XRD) using Cu K $\alpha$  radiation with a wavelength of 1.54059Å. The 2 $\theta$  value was from 10° to 110°. The electrochemical characterization was done with a Gamry Reference 600 electrochemical workstation.

#### **2.3 Nickel plating in rotating magnetic field generated by spinning magnets**

In this part of experiment, the electrolyte formula, the electrodeposition parameters (current density and temperature) and the sample preparation process are the same as the Ni plating in constant magnetic field (Section 2.2). The experimental setup is similar to that in Section 2.2, except that the austenitic stainless frame fixed with the magnets was driven to spin around the sample by a drill press, as schematically demonstrated in Fig. 2-3.

The Ni deposition experiments were performed with the drill press rotating between 1000rpm and 3000 rpm to produce an alternative magnetic field which had the same magnitude and constantly changed its direction.

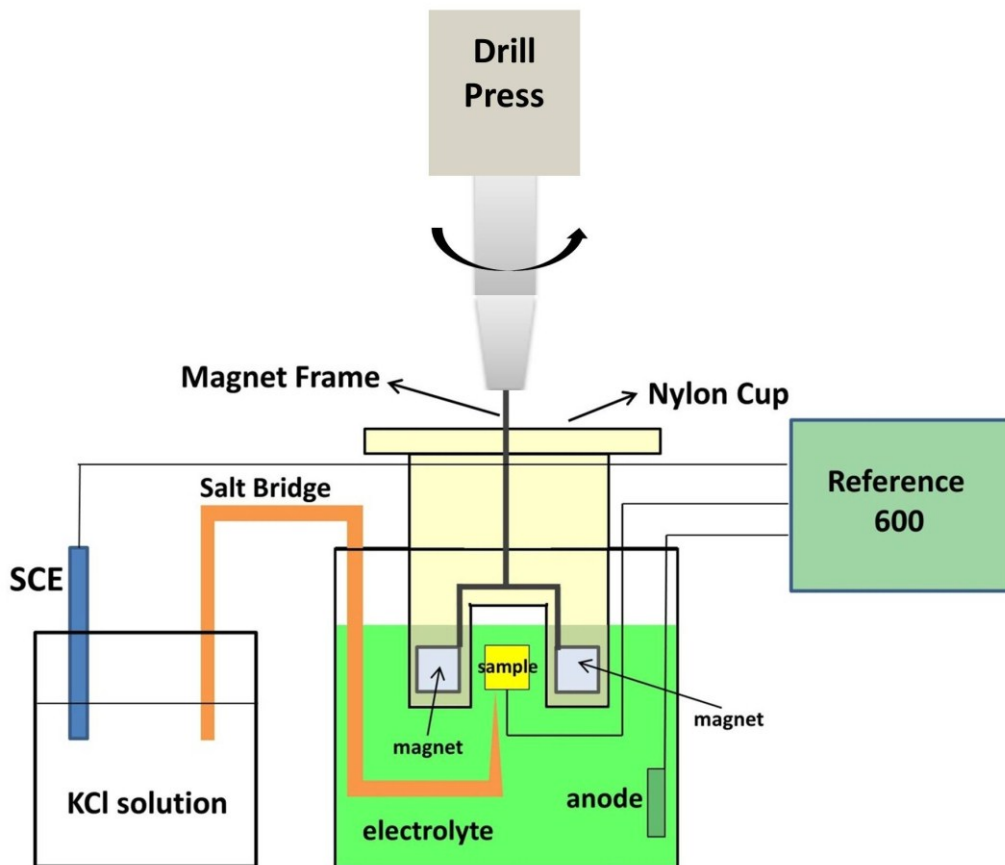


Figure 2-3 Schematic diagram of the electrolysis system in the alternating magnetic field generated from spinning magnets.

Also similar to Section 2.2, the surface morphologies of the samples were examined on a JEOL (JSM-6301FXV) field emission scanning electron microscope (SEM) and atomic force microscope (AFM) (MFP-3D, Asylum Research); the crystal structures of the deposits were analyzed by a Rigaku-UltimaIV X-ray diffractometer(XRD) using Cu  $K\alpha$  radiation with a wavelength of 1.54059Å. The  $2\theta$  value was from  $10^\circ$  to  $110^\circ$ . The electrochemical characterization was done with a Gamry Reference 600 electrochemical work station.

## **2.4 Microhardness investigation of nickel electrodeposition in magnetic field**

Nickel was electrodeposited galvanostatically in the absence of the magnetic field, and in the presence of static magnetic fields, and spinning magnets. The experimental conditions are the same as in sections 2.2 and 2.3. The deposition experiments were conducted at  $B=0$ , 0.18T parallel magnetic field, 0.18T vertical magnetic field,  $B=0.18T$  and spinning magnets' rates of 1000, 1500, 2000, 2500 and 3000rpm.

An additional test of the micro-hardness was done with a BUEHLER IndentaMet 1100 Series Hardness tester under a load of 50 grams for 15s.

## **2.5 Material characterization techniques**

### **2.5.1 Scanning electron microscope (SEM)**

An SEM is an imaging technique which permits observation and characterization of materials on a nanometer to micrometer scale. It operates on the principle that a highly focused electron beam strikes the specimen surface, the electrons enter the specimen and interact with the specimen atoms, generating various types of signals including backscattered electrons (BSE), secondary electrons (SE), characteristic X-rays and other photons of various energies. The signals generated are employed to examine the specimen's properties: surface morphology, crystallography, composition, etc. The size of the interaction volume of the electron beam and the sample is about  $1\mu\text{m}$  in diameter. The quantitation for each measurement is an average over this area.

The backscattered electrons and secondary electrons are the two most commonly used modes in SEM imaging. The former is sensitive to the element difference and is used to reveal the composition or phase distribution within the sample, while the latter is highly dependent on the morphological features of the sample and is primarily used to observe the surface topography.

Also, the electron bombardment yields EDX, which are characteristic X-rays that can be used to obtain both qualitative and quantitative elemental information about the sample.

The major advantage of SEM in imaging is the high resolution of the nanometer scale when examining bulk objects. Another important characteristic of SEM is the large depth of field which allows the appearance of a three-dimensional image of the sample surface<sup>1</sup>.

### **2.5.2 Energy dispersive X-ray spectroscopy (EDX)**

EDX is used to analyse the elements of a specimen in the SEM. The generation mechanism of the characteristic X-ray signal can be simply interpreted as follows. A beam of a high energy electron is focused onto and interacts with the tightly bound inner shell electrons of sample atoms, ejecting them from the atoms and leaving the atoms in an excited state with a missing inner shell electron. The relaxation of the excited atoms to their ground level proceeds through a limited set of allowed transitions of the outer shell electrons filling the inner shell vacancies. The energy released in these transitions can be either transmitted into the energy to eject some other outer shell electrons out of the atoms with a specific kinetic energy, called Auger electrons, or generate characteristic X-ray photons, which have sharply defined energy values characteristic of a specific element. The process is presented in Fig. 2-4.

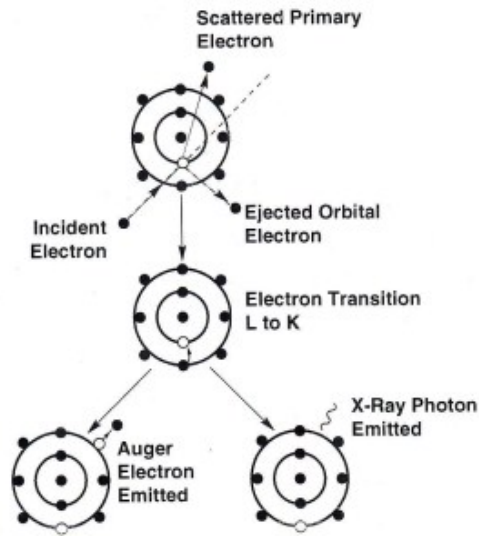


Figure 2-4 Illustration of the characteristic X-ray generation process (Fig 6.5 in Ref. 1).

The X-ray photons are collected by an EDX spectrometer and transferred into electric signals. The specific energies are used to identify the element(s) present. The relative intensities of different elements are employed to determine the composition of the specimen<sup>1</sup>.

### 2.5.3 X-ray diffraction (XRD)

X-ray diffraction (XRD) is a powerful nondestructive technique for characterizing crystalline materials. It uses a monochromatic X-ray beam to project onto the crystalline material surface. The incident X-ray is diffracted by the specimen's crystalline atoms. The diffraction process follows Bragg's law. The diffracted pattern provides information for structure and phase identification (for example, lattice structure, preferred crystal orientation (texture), average grain size, lattice parameter, and residual stress) because the number of observed peaks is related to the symmetry of the unit cell (higher symmetry generally

corresponds to fewer peaks). The positions of the diffraction peaks are determined by the distance between the parallel planes of the atoms, and the intensities of the peaks are determined by the arrangement of atoms in the entire crystal.<sup>2</sup>

In the XRD test, powder and thin film are the two most commonly used operation modes. In powder diffraction mode, the large diffraction angle range ( $0^{\circ}$ - $90^{\circ}$ ) is employed. In thin film diffraction mode, the incident beam is fixed at a small angle (normally between  $1^{\circ}$  and  $4^{\circ}$ ), allowing the X-ray interaction depth on the scale of hundreds of nanometers to several microns, thus preventing the overlapping of the diffraction signals of the coating sample and the substrate. Hence, this mode is suitable for examining the thin film specimens.

In recent years, two-dimensional (2D) X-ray diffraction (XRD<sup>2</sup>) has been extensively used in material analysis. It employs a two-dimensional detector (area detector) which obtains far more information than a conventional one-dimensional detector (point detector). Fig. 2-5 shows a typical XRD<sup>2</sup> system, which contains a 2D detector, X-ray source, X-ray optics,

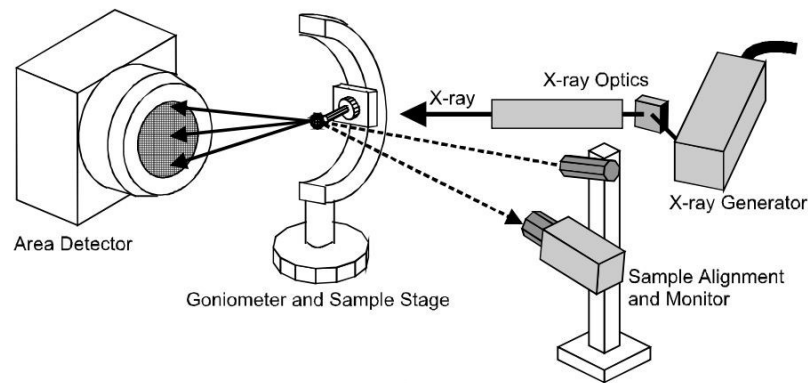


Figure 2-5 Graphic presentation of an XRD<sup>2</sup> system (Fig. 3 in Ref. 3).

sample positioning stage, sample alignment, monitoring device and computer control and data analysis software.

The diffraction geometry of XRD and XRD<sup>2</sup> is schematically presented in Fig. 2-6. For a conventional XRD test, the measurement is confined within the diffractometer plane and the structure information out of the plane is ignored. For 2D XRD, a large portion of the diffraction rings can be measured simultaneously. Fig. 2-7 shows the diffraction pattern of a sample in this research using the XRD<sup>2</sup> device.

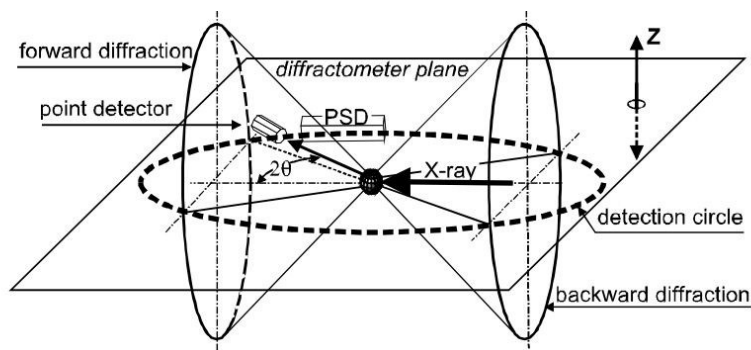


Figure 2-6 Diffraction geometry of conventional XRD and XRD<sup>2</sup> (Fig. 3 in Ref. 4).

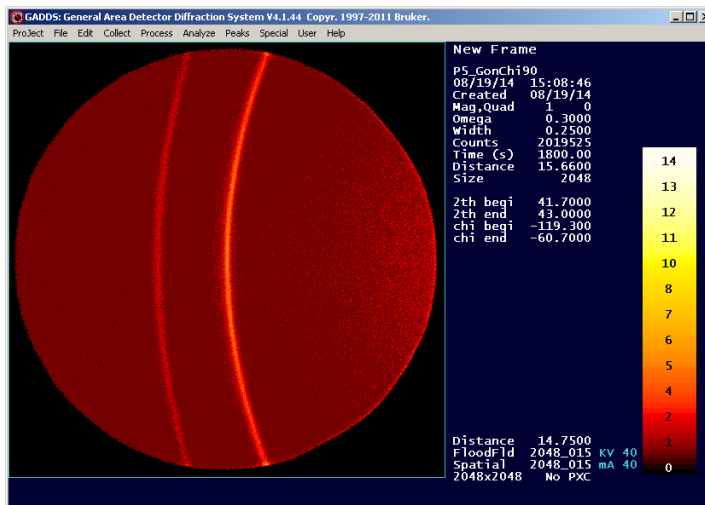


Figure 2-7 2D XRD diffraction pattern.

#### **2.5.4 Atomic force microscope (AFM)**

The AFM is a popular imaging device that can be used to detect the surface of both conductive and non-conductive samples. In principle, AFM is based on the interaction between the tip of a cantilever and the sample atoms, as schematically illustrated in Fig. 2-8. A sharpened pyramidal-shaped tip (around 2 nm in size) that is made of silicon nitride is fixed at the end of the cantilever; the interaction forces between the cantilever tip and the sample atoms are smaller than the interatomic forces, guaranteeing that the atoms are not displaced while the tip is moving across the sample surface.

In the testing process, the cantilever tip holds the position. The X-Y Piezo stage on which the sample is placed moves the sample back and forth underneath the tip in the high resolution raster scan pattern. A laser beam is focused on the upper part of the cantilever tip, and the reflected beam is directed by a mirror towards the segmented photodiode which contains four photodiodes.

When the cantilever interacts with the atoms in the sample surface, the reflected laser correspondingly changes its position on the segmented photodiode and a differential signal between the four photodiodes is generated, which is subsequently transferred into the deflection image. Meanwhile, the Z LVDT is used to measure the height change of the light source-cantilever assembly that moves up and down because of the interaction of the cantilever tip and the sample atoms, and the obtained data is displayed as a height image.

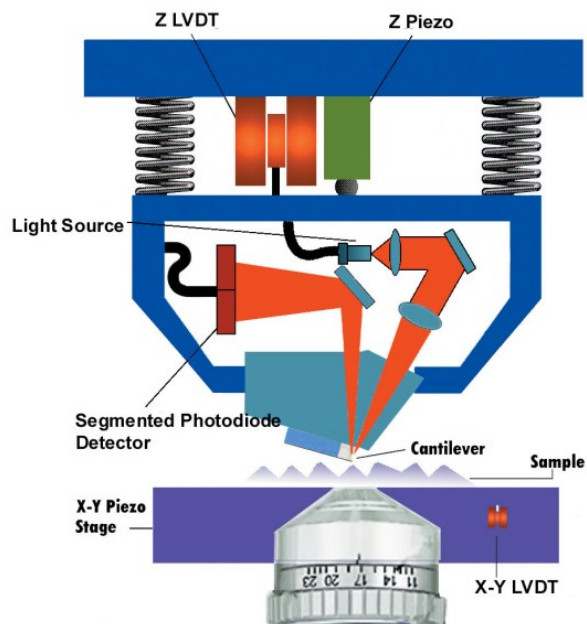


Figure 2-8 Illustration of the operation principle of the MFP-3D atomic force microscope (Fig. 5.2A in Ref. 5).

## 2.6 References

- 1 G. J. I. Newbury, D. E. Joy, D. C. Lyman, C. E. Echlin, P. Lifshin, E. Sawyer, L. Michael, J. R. Scanning electron microscopy and X-ray microanalysis, 3rd edition, (Springer, New York, 2007).
- 2 Cullity, B. D.; Stock, S. R. in Elements of X-ray diffraction, 3rd edition, (Prentice Hall, New Jersey, 2001).
- 3 B. B. He, Powder Diffraction 18 (2), June 2003.
- 4 B. B. He, U. Preckwinkel and K. L. Smith, JCPDS-International Centre for Diffraction Data 2000, Advances in X-ray Analysis, Vol.43.

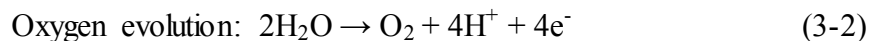
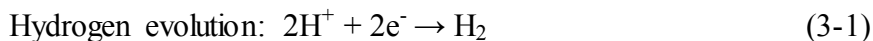
5 MFP-3D™ Atomic Force Microscope Installation and Operation Manual from Asylum Research, Inc. 2003-2004.

**Chapter 3 Composition and Colour Control of Nickel-Copper Electro-Co-  
deposition in Citrate Bath**

### 3.1 Introduction

Although Ni-Cu codeposition in a citrate bath has drawn considerable interest and has been extensively studied for decades, some challenges still exist prior to its commercialization. First, the solution was reported to be chemically unstable and tended to form precipitates. For example, when sulfate was used, the precipitates were identified to be complex species of  $\text{Cu}_2\text{H}_1\text{Cit}\cdot 2\text{H}_2\text{O}$  and  $\text{Ni}_4(\text{OH})_6\text{SO}_4$ <sup>1</sup>. Also, the coating composition is sensitive to the pH level in the citrate bath. Rode *et al.*<sup>2</sup> have demonstrated that varying the pH in the citrate bath for Ni/Cu codeposition will lead to a distributional variation in concentrations of nickel and copper citrate complex species (14 copper complex species and 7 nickel citrate complex species). This causes the shift of the nickel and copper partial steady-state polarization curves: the partial copper current curve moves significantly toward more negative potentials, while the partial nickel current curve is not obviously altered as pH increases. As a result, the reduction of copper becomes more difficult at a higher solution pH, resulting in a deposit with higher nickel content. Therefore, a constant pH value is a prerequisite for achieving chemical stability in the plating solution and the film.

It has been well studied<sup>3-6</sup> that neither hydrogen ions nor hydroxyl ions are involved in the dominant metal reduction reactions on the cathode, and the change in pH value during electroplating is mainly caused by hydrogen and oxygen evolution reactions on the cathode and anode surface, respectively. The corresponding electrochemical reactions are:<sup>7</sup>



By controlling hydrogen and oxygen evolution reactions, the pH variation can be controlled within the buffer capacity of the solution and a stable coating composition profile can be achieved.

In addition, the apparent color of the Ni/Cu alloy is important for its application. The color of the Ni/Cu alloy varies in appearance from white nickel to red copper. The composition of the nickel-copper plating layer is believed to be the most important factor in determining the color of the coating. The dependence of the Ni/Cu alloy coating color on other electroplating parameters has not been reported. However, this dependence is also meaningful to the application of such a codeposition technique to the modulation of the coating color in industrial production.

Finally, the coating temperature is also critical to the quality of the deposition. It has been well established that a higher temperature generally yields a higher surface irregularity and larger grain size<sup>8</sup>. On the other hand, for alloy plating, increasing the temperature promotes the uniformity of the coating composition. For nickel and copper codeposition in citrate bath, the specific influence of temperature, in our opinion, is linked with the solution chemistry of the citrate bath. However, this linkage has yet to be determined.

In the present work, a method of controlling the composition of Ni/Cu coating in the citrate bath by stabilizing the solution pH value of the electrolyte has been developed. Our investigation also found that in addition to the coating composition, the bath pH level can affect the color of the Ni/Cu alloy deposition in the citrate bath.

### 3.2. Experimental

Nickel-copper coating layers were electroplated galvanostatically with two DC power supplies under constant current mode. Plates of nickel and copper were employed, which were connected to the positive ends of the power supplies, to serve as anodes.

The electroplating experiments include beaker setup plating and barrel plating. Fig. 3-1 depicts the experimental setup for the two kinds of plating test.

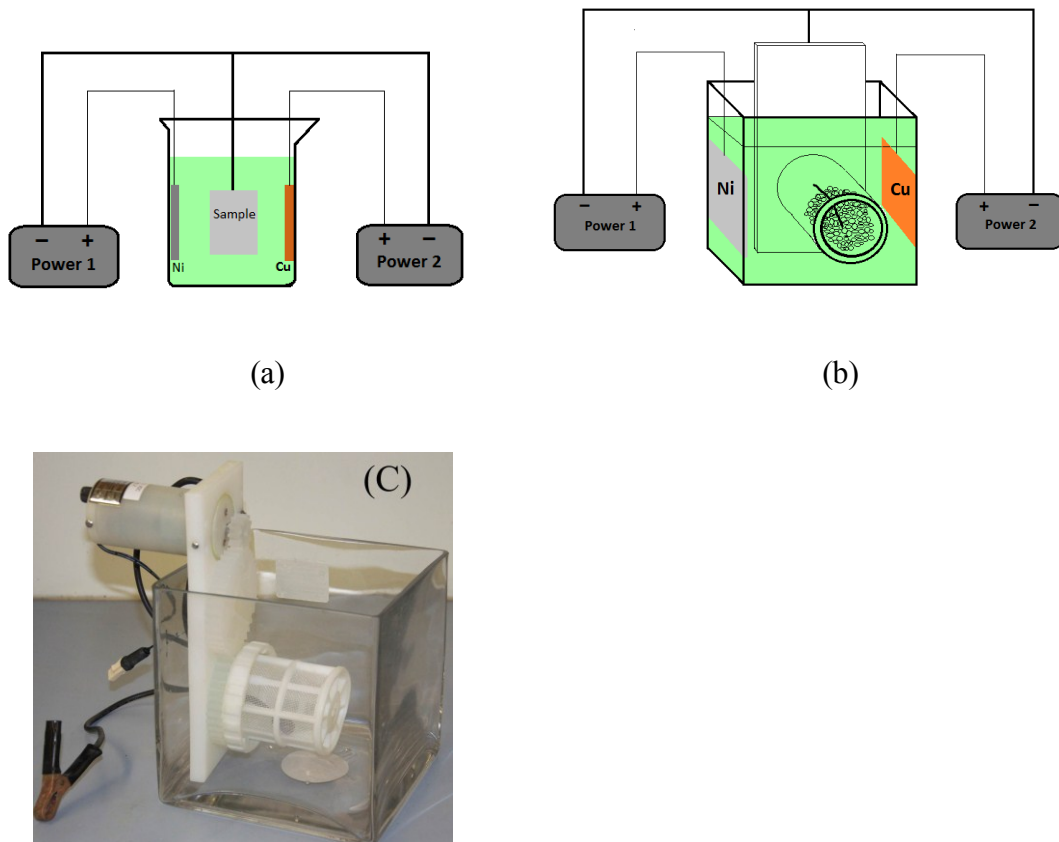


Figure 3-1 Experimental setup for (a) beaker plating, (b) barrel plating, and (c) photo of barrel plating device.

In the beaker plating, low-carbon steel discs with a diameter of 2.35 cm were used as the plating substrates. The back of each disc was sealed using insulating glue. The electroplating experiments were conducted in a 300 ml beaker. The electrolyte pH was at 4.60. The bath temperature was maintained at two values,  $40\pm 2$  and  $56\pm 2^\circ\text{C}$ , to test the temperature dependence of the coating composition. Agitation was provided by a magnet stirring bar at a rate of 350 rpm.

In the barrel plating, the electrolyte was filled in a 3-liter glass tank; a barrel with a diameter of 6 cm was driven by a motor to rotate at the speed of 8 rpm. The samples were 1-cm squares made from low-carbon steel. In addition, 40 pieces of steel discs with the same dimensions given above were used. They were cut into four small pieces and filled into the barrel to ensure good random electric contacts with the cathode tip inside the barrel. The plating temperature was  $30\pm 2^\circ\text{C}$ , and the electrolyte pH was controlled at two different values, 4.5 and 5.1.

All samples were mechanically polished with 1200-grit SiC sandpaper and  $0.05\ \mu\text{m}\ \text{Al}_2\text{O}_3$  slurry on a polishing cloth. This was followed by degreasing treatment and activation processes. The electrolyte solution in beaker plating contained 0.4M  $\text{NiSO}_4\cdot 6\text{H}_2\text{O}$ , 0.008M  $\text{CuSO}_4$ , 0.3M tri-sodium citrate ( $\text{Na}_3\text{C}_6\text{H}_5\text{O}_7\cdot 2\text{H}_2\text{O}$ ), 0.00069M sodium dodecyl sulfate (SDS), 0.0027M saccharin and 0.005M  $\text{NiCl}_2$ . The barrel plating electrolyte was composed of 0.3M  $\text{NiSO}_4\cdot 6\text{H}_2\text{O}$ , 0.006M  $\text{CuSO}_4$ , 0.3M tri-sodium citrate ( $\text{Na}_3\text{C}_6\text{H}_5\text{O}_7\cdot 2\text{H}_2\text{O}$ ), 0.00069M sodium dodecyl sulfate (SDS), 0.0027M saccharin and 0.005M  $\text{NiCl}_2$ . All chemicals were analytical reagent-grade. Deionized water was used to prepare the electroplating solutions.

An Accumet 13-620-547 electrode for free copper ion measurement was employed to measure the free copper ion concentration in the bath. The cyclic voltammogram was measured by a Gamry Reference 600 electrochemical work station.

Characterization of the plating layers was conducted using a JEOL (JSM-6301FXV) field emission scanning electron microscope (SEM) for morphology observation, a ZEISS (EVO – MA15) SEM with energy dispersive X-ray spectroscopy (EDX) to determine the chemical compositions, a Rigaku-UltimaIV X-ray diffractometer for structure determination using Cu  $K\alpha$  radiation with a wavelength of 1.54 Å and  $2\theta$  range of  $10^\circ$  to  $110^\circ$ , Bruker D8 Discover 2-dimensional XRD equipment with a 2-dimensional detector Vantec200 for residual stress measurement, and a nanoindenter (Fischerscope H100 Micro Hardness Tester with Berkovich tip) to measure the Yong's modulus.

### **3.3 Results and discussion**

#### **3.3.1 Control of Ni/Cu codeposition parameters in citrate bath**

##### **3.3.1.1 Approach for replenishing metal ions in plating bath during plating**

Replenishing metal ions in the plating bath during plating is essential to maintain a constant nickel and copper content in the bath and to control the composition in the coatings. Several methods have been considered to provide Ni and Cu ions into the solution. These methods include:

**Adding copper salt during plating:** This option has the merit of being easy to operate, as well as being able to predict and control the copper content in the bath, thus controlling the

composition of the coating. However, adding Cu salt would also introduce additional anions such as sulphate ions into the bath, if  $\text{CuSO}_4$  is used. If the copper content is low in the coating, the amount of added  $\text{SO}_4^{2-}$  is very limited and there can be little effect. In copper-dominated plating, however, with large amount of copper needed, the influence of excessive  $\text{SO}_4^{2-}$  cannot be neglected. Although the solution pH is 4.60 in this research, the possibility of this  $\text{SO}_4^{2-}$  contained complex precipitating increases if a large amount of  $\text{SO}_4^{2-}$  is added into the bath, especially in the vicinity of the cathode surface where the local pH is higher than that in the bulk solution<sup>9</sup>. Also, according to electrochemistry theory<sup>10</sup>, increasing the anion concentration in the solution could lead to an increase of ionic strength, which may reduce the thickness of electric double layer on the cathode, and potentially alter the adsorption and diffusion processes of the metal ions on the cathode surface, and thus changing the coating composition.

**Employing one anode made of nickel-copper alloy:** Using an alloy anode might not be very practical as the composition of the alloy is fixed and can be quite different from that of coatings because the current efficiencies of nickel and copper species in reduction are different. Therefore it is difficult to control the coating composition by using an alloy anode with a fixed composition.

**Connecting both nickel anode and copper anode to one power supply and controlling the area ratio:** This option may cause an un-matched rate of dissolution of the nickel and copper anodes. The ratio of current distribution on these two anodes is affected by the factors including the surface area of metal anodes, the thickness and shape. All of these factors could affect the rate of dissolution of individual anodes and may change during dissolution.

Therefore the current ratio between the nickel and copper anodes may not be equal to its initial value.

**Using nickel anode and copper anode alternatively and controlling the ratio of their**

**service times**: This method seems feasible with its simplicity in controlling coating composition by adjusting the ratio of service time of the nickel and copper anodes. However, our experiment showed that both the copper content in coating and free copper ion concentration in the bath increased continuously during plating, and no stable composition could be achieved. The reason for this phenomenon will be further discussed in Section 3.3.3. In fact, the investigation of this unusual result has led to the discovery of a new method in modulating the ion concentration in the alloy deposition bath.

**Connecting nickel anode and copper anode to two separate power supplies and**

**controlling the current ratio**: This method was finally selected as a potential approach for compositional control. It will control the nickel and copper ion provision by modulating the current ratio between the nickel and copper anodes, and avoid the problems associated with the previously discussed approaches. Our experimental results both in beaker setup plating and in barrel plating with this method have proved that the composition distribution along the cross section of the coating is quite uniform. The following sections will report details of the results achieved by this method.

**3.3.1.2 Stability of the pH value of the bath**

As was reviewed in the introduction, in order to achieve uniform composition in the coating, a constant pH of the plating bath is a prerequisite. If the pH value in the citrate bath changes

significantly during plating, the stability of the plating bath as well as the deposition behaviour and the coating composition will be affected.

In this research, the citrate plating bath was proven to be stable when the pH is lower than 5.5 both in free standing and in electroplating. And the pH value was set to be and kept at 4.60 in beaker plating experiments. The following three factors were identified as critical in maintaining the stability of the solution pH during electroplating.

- 1) It is important to avoid anodic passivation, which can result in severe oxygen evolution and a pH drop. The anodic passivation has been realized by adding nickel chloride into the solution because chloride ions can destabilize passive film on the anode surface and ensure the dissolution of the metal.
- 2) The areas of Ni and Cu anodes have to be properly selected so that the current densities and thus the oxygen development on the anodes can be controlled and balance the hydrogen evolution on the cathode. Three steps can be taken to achieve the goal.

**Step 1:** Decide both anodic and cathodic current efficiencies which are measured and depicted in Fig. 3-2.

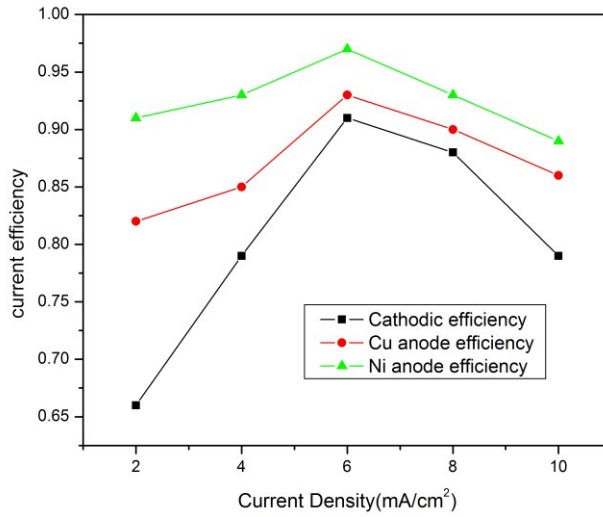


Figure 3-2 Current efficiencies for Cu and Ni anodes, and Ni/Cu codeposition on cathode in citrate bath.

**Step 2:** Determine the relations between the anodic and cathodic areas and current efficiencies. Assuming that oxygen development on the anodes can exactly balance the hydrogen evolution on the cathode to keep the pH of the bath constant, we can obtain the following equations:

$$\frac{I_{Cu}}{S_{Cu}}(1 - \eta_{ac}) + \frac{I_{Ni}}{S_{Ni}}(1 - \eta_{an}) = \frac{I_C}{S_C}(1 - \eta_c) \quad (3-3)$$

$$I_{Cu} + I_{Ni} = I_C \quad (3-4)$$

$$\frac{I_{Cu}}{I_{Ni}} = R \quad (3-5)$$

Where  $I_{Cu}$ ,  $I_{Ni}$  and  $I_C$ ,  $\eta_{ac}$ ,  $\eta_{an}$  and  $\eta_c$ ,  $S_{Cu}$ ,  $S_{Ni}$  and  $S_C$  are currents on, current efficiencies and areas of Cu anode, Ni anode and cathode, respectively;  $R$  is the desired Cu and Ni anode current ratio. Equation (3-3) denotes the balance of the hydrogen and oxygen evolution on cathode and anodes.

**Step 3:**  $\eta_c$  and  $\eta_{ac}$  can be chosen from Fig. 3.2 to have relatively high values (e.g., around their highest points when the current density is 6 mA/cm<sup>2</sup>), leaving  $\eta_{an}$  to be calculated by the equations. Because the current efficiency for the Ni anode is normally close to 100%, even when calculated by Equations (3-3), (3-4) and (3-5), the Ni anode efficiency is still above 90% if the current density is less than 9 Am/cm<sup>2</sup>, according to Fig. 3.2. The corresponding cathode current density as well as  $I_C$  is also determined because  $S_C$  is the area of the sample which has been given in the experimental section. Also, the copper anode current density  $I_{Cu}/S_{Cu}$  can be determined from the Cu anode current efficiency curve in Fig 3.2 once  $\eta_{ac}$  is chosen.

When the values of  $I_C$  and  $R$  are known,  $I_{Cu}$  and  $I_{Ni}$  can be calculated using Equation (3-4) and (3-5). And because  $I_{Cu}/S_{Cu}$  has already been determined,  $S_{Cu}$  can be calculated.

Next, Equation (3-3) can be solved numerically to obtain  $I_{Ni}/S_{Ni}$  and  $S_{Ni}$ , since  $\eta_{an}$  is the function of current density  $I_{Ni}/S_{Ni}$ , and is presented in Fig. 3-2.

The above process can be used to determine Cu and Ni anode areas, but also enable the electroplating to be conducted at high current efficiency.

3) Sufficient citrate is required in the bath to provide an adequate buffer effect. Fig. 3-3 shows the titration test result of the citrate bath in which 0.01M H<sub>2</sub>SO<sub>4</sub> was titrated into three solutions with different citrate concentrations. Sodium citrate was employed as a buffering

agent. When its concentration is above 0.2M, the solution has a high buffering capacity in a pH region below 5.0. Therefore it is concluded that the concentration of citrate in the bath should exceed 0.20M. In the experiments for this work, the citrate concentration was set to be 0.26M for beaker plating and 0.3M for barrel plating.

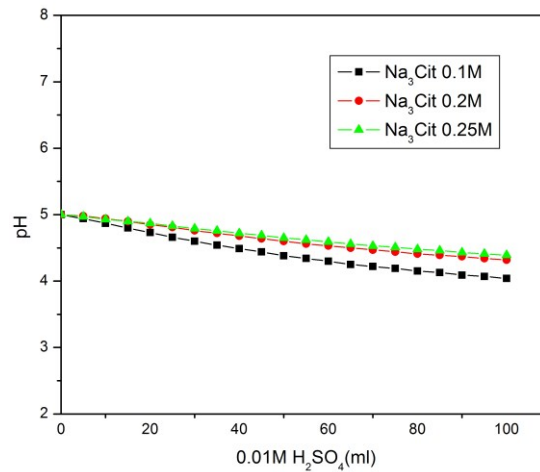


Figure 3-3 Titration curves of 100ml Ni/Cu codeposition bath with different citrate concentrations and titrated with 0.01M H<sub>2</sub>SO<sub>4</sub> at 40°C.

The procedure described in 2) was applied to beaker setup plating where the cathodic current was 17mA (current density = 3.92mA/cm<sup>2</sup>), corresponding to the cathodic current efficiency  $\eta_c = 79\%$ ,  $\eta_{ac}$  was chosen to be 89%, the related copper anode current density was 5mA/cm<sup>2</sup>.  $S_{Cu}$  and  $S_{Ni}$  were then determined to be 1.0 cm<sup>2</sup> and 2.9 cm<sup>2</sup>. After 12 hours of electroplating, the pH changed from 4.60 to 4.62. A similar process was performed during barrel plating with the apparent current density being 1.73mA/cm<sup>2</sup>. After 10 hours plating, the pH increased slightly from 4.60 to 4.65.

### 3.3.1.3 Temperature selection for Ni/Cu codeposition in citrate bath

To sustain the codeposition in Ni/Cu citrate bath with sulfate for an extended period, the blue colored complex precipitate  $\text{Cu}_2\text{H}_1\text{Cit}\cdot 2\text{H}_2\text{O}$  has to be under control. However, even when its generation in the bulk solution has been well prevented by appropriately designing the electrolyte formula and controlling the solution pH, the precipitate can be formed on the copper anode surface and migrated into the bath, due to the relatively low local pH and high cupric ion concentration.

In our opinion, one way to avoid the accumulation of the precipitate from the anodic process is to increase its solubility in the plating bath. For this purpose, a solubility measurement of this kind of precipitate in the electrolyte used for barrel plating was performed. Fig. 3-4 shows the solubility variation as a function of the bath temperature. The solubility gradually increases when the temperature is below 56 °C, then abruptly jumps up from 56 °C to 60 °C and remains almost constant at higher temperatures, like a typical solubility curve of surfactant with a Krafft point.

According to the results in Fig. 3-4, it is desirable to select the plating temperature to be 60°C in order to remove the precipitate of  $\text{Cu}_2\text{H}_1\text{Cit}\cdot 2\text{H}_2\text{O}$  from the electrolyte because of its elevated solubility. A period of 20 hours barrel plating operation was carried out to confirm the effectiveness of this temperature selection. No precipitate was found in the bath either during the plating or in the subsequent free standing.

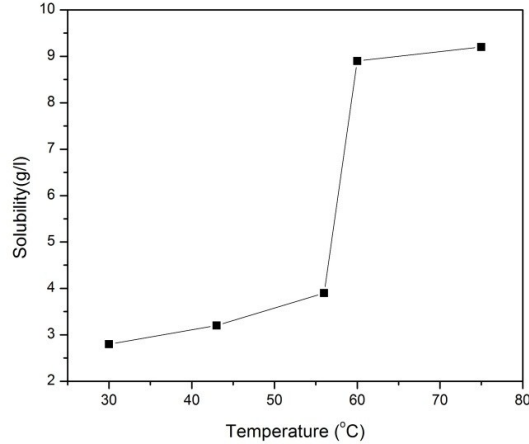


Figure 3-4 Solubility of complex precipitate  $\text{Cu}_2\text{H}_1\text{Cit}\cdot 2\text{H}_2\text{O}$  in the electrolyte for barrel plating at different temperatures.

### 3.3.2 The composition control of the Ni-Cu codeposition

#### 3.3.2.1 The dependence of the coating composition on the nickel and copper anode current ratio

Fig. 3-5 shows the cross-section of the Ni-Cu coating plated on the steel substrate. The coated layer appears uniform and has a good adhesion to the steel substrate.

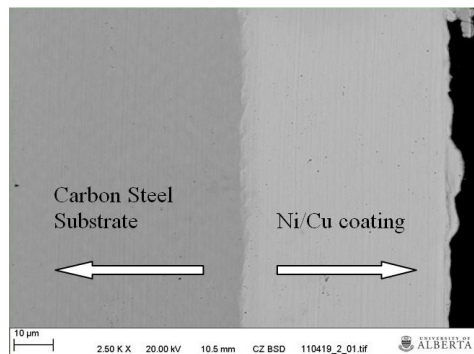
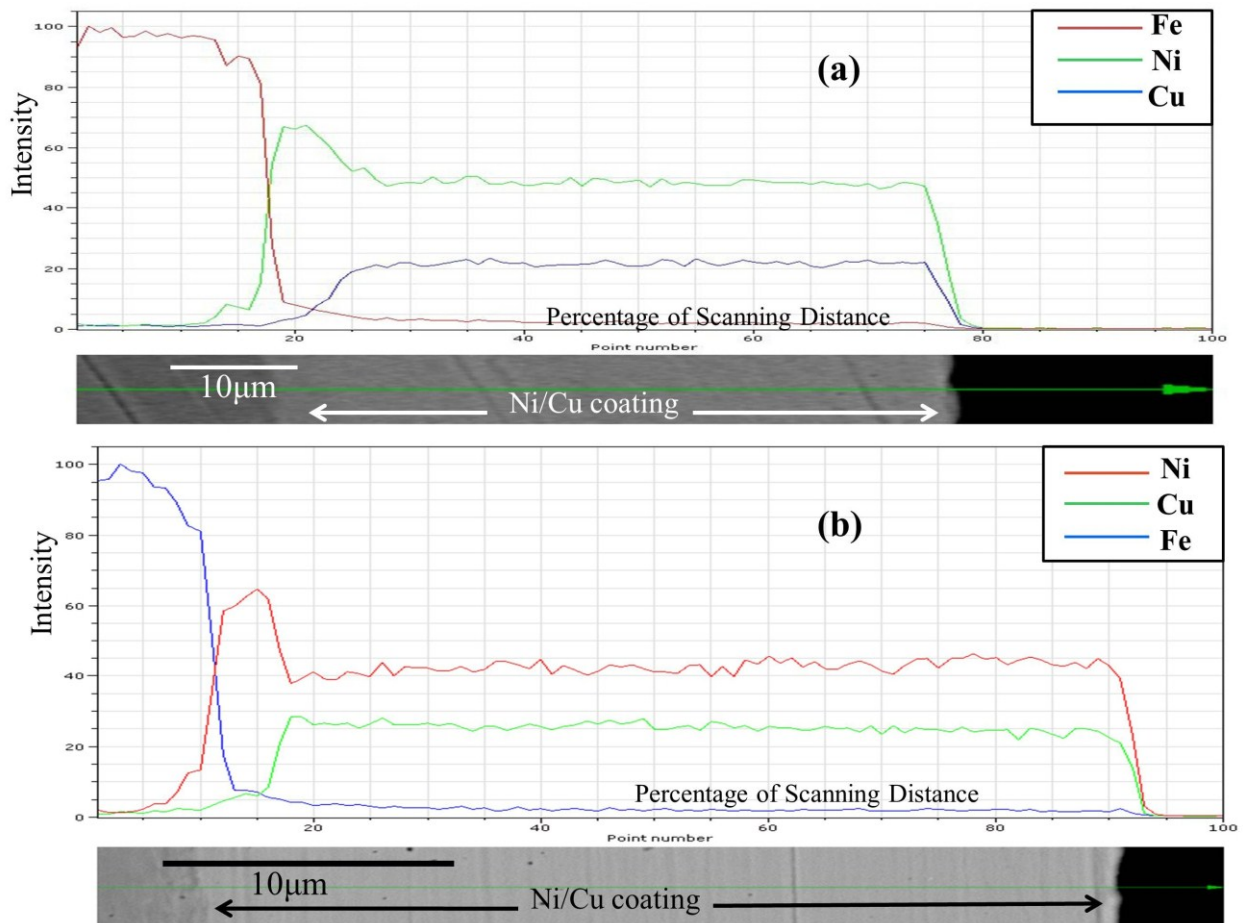


Figure 3-5 Back Scatter Electron (BSE) image of the cross section of the nickel-copper alloy coating.

Figure. 3-6 shows X-ray line scanning analysis along the cross sections of the Ni-Cu coatings in three different beaker setup plating tests. The initial copper sulphate concentrations in the bath were 0.0056M, 0.0080M, and 0.0104M, respectively. In these tests, the current density on the cathode was kept the same at  $3.92\text{mA/cm}^2$ ; the ratio of the Cu anode current over the total anodic current was 0.3; the temperature was maintained at  $56^\circ\text{C}$ ; the plating time was 12 hours and the thickness of these plating layers was about  $50\ \mu\text{m}$ .



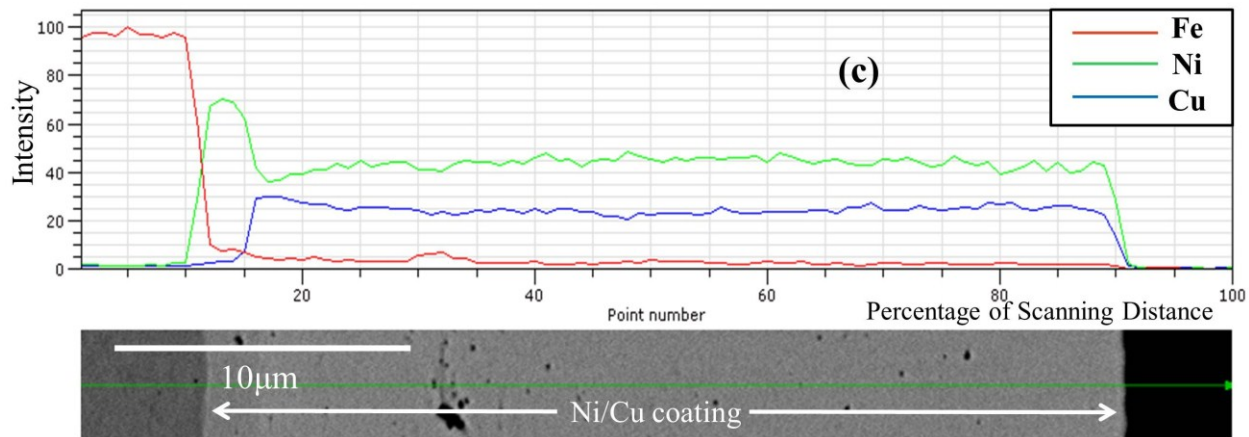


Figure 3-6 X-ray line scanning result along the cross sections of the Ni-Cu coatings in three different beaker setup plating tests with different initial copper sulphate concentrations in the bath (a) 0.0056M, (b) 0.0080M, (c) 0.0104M.

The results in Fig. 3.6 show that despite the different initial  $\text{CuSO}_4$  concentrations in the bath, the coating composition tends to be stable and can remain identical after plating for long time. For the low  $\text{CuSO}_4$  concentration bath, the copper content was low at the beginning of the plating, but increased with time and reached a relatively stable level; for the medium  $\text{CuSO}_4$  concentration bath, the copper content was almost constant throughout the plating; and for the high  $\text{CuSO}_4$  concentration bath, the copper content decreased in the initial stage but became stable after plating for a few hours. The initial  $\text{CuSO}_4$  concentration in the plating bath appears only to affect the time period required to achieve the stable composition.

The average copper content on the surface of the samples from these three tests was analyzed by EXD and was determined to be 33.5 wt%, 32.2 wt%, 34.3 wt%, respectively, indicating the dependence of the Cu content on the anode current ratio, regardless of the initial  $\text{CuSO}_4$  content in the plating bath.

To explain this result, we first consider the current efficiencies for both the cathode and anode to be 100%. The nickel and copper ions are released from these two anodes, which react immediately with the citrate solution and form copper and nickel complex species which were discussed in detail by Sabine Rode *et al.*<sup>7</sup> On the cathode surface, on the other hand, those copper and nickel complex species are reduced and deposited. For the copper redox process, at the beginning, copper ions are released from the copper anode and copper complex species are formed in the bath; therefore the concentration of the copper complex species in the bath tends to increase. Meanwhile, these copper complex species are consumed at the cathode, and the rate of the consumption is determined by the concentrations of these complexes in the bath as well as cathode current density. If, for example, because of the high current ratio of the copper anode, the amount of copper ions added into the solution is higher than that being reduced on the cathode, the copper complexes will accumulate in the bath and their concentration will increase. This will in turn enhance the reduction rate of these copper complex species and increase the copper content in the coating. As the process continues, an equilibrium condition will be eventually established and the copper partial reduction current at the cathode will be equal to the current on the copper anode.

The nickel redox process, however, is different from that of copper due to the much higher nickel content in the bath. In the process of achieving equilibrium, the nickel content changes much more slowly than the copper content. Therefore when the equilibrium has been established, the nickel content in the bath remains almost unchanged. As a result, at the equilibrium state, the concentrations of the complex species in the bath as well as the composition in the coating are constant, and this equilibrium coating composition is determined only by the current ratio between the nickel and copper anodes. From Faraday's

law and the values of atomic weight of copper and nickel elements, the copper content in the coating can be deduced as:

$$Cu \text{ wt}\% = \frac{64 * R}{64 * R + 59} \quad (3-6)$$

Where  $R$  is the current ratio between the Cu anode and Ni anode, i.e.,  $I_{Cu}/I_{Ni}$ .

In reality, however, the current efficiencies of cathodic and anodic reactions have never been 100% and Equation (3-6) represents only an idealized situation.

For non-idealized situations, we assume that the anode current efficiencies for the copper anode and nickel anode are  $\eta_{an}$  and  $\eta_{ac}$ , respectively; the currents on the nickel anode and copper anode are  $I_{Ni}$  and  $I_{Cu}$ ; and the current resulting from oxygen development on two anodes is assumed to be  $I_{aO2}$ . On the cathode, the reduction current is assumed to be  $I_c$ , which can be divided into three parts: the nickel, copper and hydrogen partial reduction current. Suppose that the fractions of these three currents in the total reduction current  $I_c$  are  $X_{Ni}$ ,  $X_{Cu}$ , and  $X_H$ , and

$$X_{Ni} + X_{Cu} + X_H = 1 \quad (3-7)$$

Since the total current on cathode equals that on the two anodes, we have,

$$I_{aO2} + \eta_{an} * I_{Ni} + \eta_{ac} * I_{Cu} = (X_{Ni} + X_{Cu} + X_H) * I_c \quad (3-8)$$

And let

$$X_H * I_c - I_{aO2} = I_p \quad (3-9)$$

If the solution pH is constant or varies slightly,  $I_p$  should be zero or a small quantity. And if pH increases,  $I_p$  is positive.

Combining Equation (3-8) and (3-9) yields

$$\eta_{an} * I_{Ni} + \eta_{ac} * I_{Cu} = X_{Ni} * I_C + X_{Cu} * I_C + I_P \quad (3-10)$$

It is well known that the copper species is much more easily to be reduced than the nickel species due to copper's higher reduction potential. It is therefore reasonable to assume that when the stable stage shown in Figure 3-6 is established, all the copper species generated from the copper anode are consumed in the cathodic reaction, i.e., are deposited into the alloy coating, so that

$$\eta_{ac} * I_{Cu} = X_{Cu} * I_C \quad (3-11)$$

Incorporating Equation (3-11) with (3-10) gives

$$\eta_{an} * I_{Ni} = X_{Ni} * I_C + I_P \quad (3-12)$$

Dividing Equation (3-11) by (3-12), we obtain

$$\frac{I_{Cu}}{I_{Ni}} = \frac{\eta_{an}}{\eta_{ac}} \frac{X_{Cu} * I_C}{X_{Ni} * I_C + I_P} \quad (3-13)$$

And assume

$$I_P = \delta * I_C \quad (3-14)$$

Equation (3-13) then becomes

$$\frac{I_{Cu}}{I_{Ni}} = \frac{\eta_{an}}{\eta_{ac}} \frac{X_{Cu}}{X_{Ni} + \delta} \quad (3-15)$$

At 100% current efficiencies of the anode and cathode,  $\eta_{an} = \eta_{ac} = 100\%$  and  $\delta = 0$ , Equation (3-15) reduces to  $I_{Cu}/I_{Ni} = X_{Cu}/X_{Ni}$ , which can be transformed into Equation (3-6).

If the copper and nickel anode areas can be controlled to maintain a stable pH value and anodic passivation can be avoided,  $\delta$  should be a small quantity, both  $\eta_{an}$  and  $\eta_{ac}$  can be close to 100% and approximately equal to each other, with  $\eta_{an}$  being slightly bigger than  $\eta_{ac}$  due to the noble character of copper.

Equation (3-15) can be re-arranged into

$$\frac{X_{Cu}}{X_{Ni}} = \left(1 + \frac{\delta}{X_{Ni}}\right) \frac{\eta_{ac}}{\eta_{an}} \frac{I_{Cu}}{I_{Ni}} \quad (3-16)$$

Where the term  $(1 + \delta/X_{Ni})$  is close to unit, and the term  $\eta_{ac}/\eta_{an}$ , according to Fig. 3-2, is less than but close to unit. As a whole the value on the right side of Equation (3-16) is nearly equal to  $I_{Cu}/I_{Ni}$ , i.e.,  $X_{Cu}/X_{Ni} \approx I_{Cu}/I_{Ni}$ , which can be transformed into Equation (3-6). This means that Equation (3-6), which is correct for the ideal case of 100% current efficiency, is also approximately valid for non-ideal cases of electroplating. This conclusion is consistent with the experimental results obtained.

### 3.3.2.2 The composition dependence on the bath temperature and the coating current density

Fig. 3-7 shows the curves of the copper content in the Ni-Cu coating versus the copper anode current ratio, R, at different temperatures and cathode current densities in beaker setup plating. The data shown in Fig. 3-7 are listed in Table 3-1.

Both Table 3-1 and Fig 3-7 show that the composition of the coating from actual plating is close to the theoretical values calculated from Equation (3-6). It also shows that the copper content in the coating deviates more from the ideal value either when the temperature is lower, assuming current density is the same; or when the current density is lower under the same plating temperature. These observations are in agreement with the facts that at a higher temperature, the activities of the nickel complex species in the bath are enhanced; and at a higher cathode current density, the nickel reduction over-potential is decreased. All these will facilitate the nickel reduction and tend to increase the nickel content in the coating. Meanwhile, the copper reduction is almost unaffected because copper is easy to be reduced. Thus the copper content drops at a higher temperature or at a higher plating current density.

Based on the above results, it is certain that the composition of the Ni-Cu alloy coating can be influenced by the plating temperature and the current density. Once these two parameters are chosen, a Cu wt% versus R curve in Fig. 3-7 can be measured experimentally, and the composition of the Ni-Cu coating will follow the measured curve.

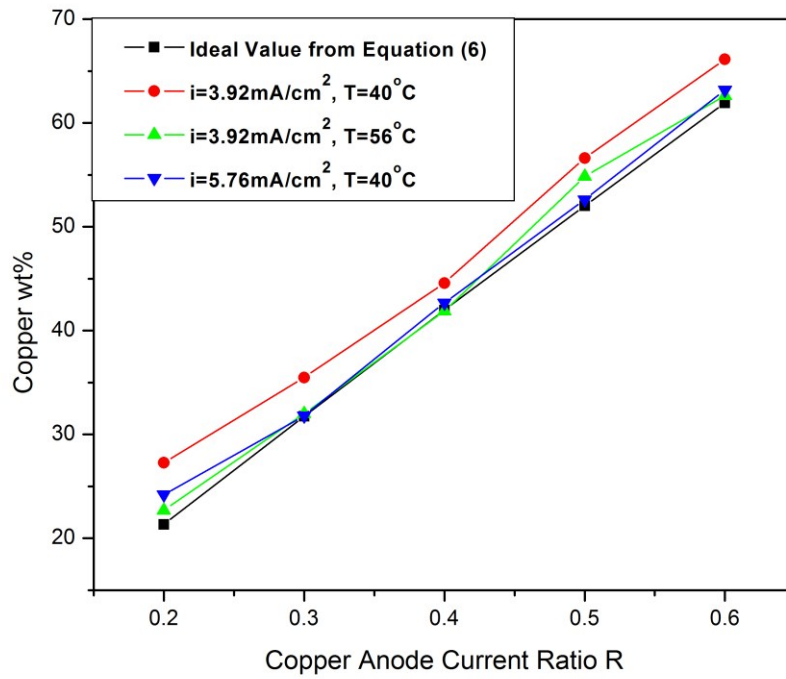


Figure 3-7 Relationship between coating composition and copper anode current ratio at different conditions in beaker setup plating experiments.

**Table 3-1 The copper content in coatings at different conditions**

I(mA/cm <sup>2</sup> )	Temperature(°C)	R	Average Copper wt%**	Ideal Value*	standard deviation
3.92	40	0.2	27.3	21.3	3.2
3.92	40	0.3	35.5	31.7	5.1
3.92	40	0.4	44.6	42.0	6.3
3.92	40	0.5	56.6	52.0	7.5
3.92	40	0.6	66.1	61.9	6.7
3.92	56	0.2	22.7	21.3	4.3
3.92	56	0.3	32.0	31.7	5.0
3.92	56	0.4	41.9	42.0	4.1
3.92	56	0.5	54.8	52.0	5.5
3.92	56	0.6	62.6	61.9	2.0
5.76	40	0.2	24.2	21.3	4.7
5.76	40	0.3	31.8	31.7	5.0
5.76	40	0.4	42.7	42.0	6.9
5.76	40	0.5	52.6	52.0	6.1
5.76	40	0.6	63.2	61.9	6.6

\*: Calculated using Equation (3-6).

\*\* : Determined by averaging 10 data randomly measured on the sample surface after plating at specified conditions for 12 hours.

### **3.3.2.3 The composition consistency of the coating on the sample surface**

The composition distribution of the alloy coating across the sample surface was not highly uniform, especially for the beaker set-up plating, because the current distribution in the bath is not uniform. Apart from adjusting the positions of the anode and cathode, one way to overcome this problem in our experiments is to perform electroplating at relatively higher temperatures. Increasing the plating temperature facilitates thermal motions of the charge carriers in the bath, rendering more uniformity in the current distribution, and resulting in improved compositional consistency across the sample surface.

The standard composition deviations from the beaker setup plating in this investigation are listed in Table 3-1, which shows that the standard composition deviation reduces with increasing temperature, and decreasing current density.

### **3.3.2.4 Application in barrel plating**

We also have conducted barrel plating experiments of Ni-Cu alloy deposition and the results obtained are similar to those acquired from beaker setup plating, except that the copper content in the coating was about 10% higher than that obtained from the beaker setup plating under the same plating temperature and the anode current ratio. This difference may result from the lower reduction current density in the barrel plating experiments. Therefore, all the findings/conclusions from beaker setup plating are applicable to barrel plating.

### 3.3.3 A novel method to control Cu content in Ni/Cu citrate plating bath

The discovery of this new approach to control copper ion concentration in Ni/Cu codeposition was initiated in an attempt to control the Ni/Cu coating composition by connecting a Ni and a Cu anode alternatively to one power supply and adjusting their service time ratio, as was described in Section 3.3.1.1.

In the experiment the plating current was at 17 mA and the cathodic current density was at  $3.92 \text{ mA/cm}^2$ . It turned out that under this anode system arrangement, the free copper ion concentration in the bath increased almost linearly as the electrodeposition proceeded; meanwhile, the copper content across the coating thickness increased quickly and nearly linearly with plating time, from about 20 wt% to 80 wt% in 10 hours, as shown in Fig. 3-8.

If the disconnected anode was taken out of the solution as the other anode was working, the obtained coating composition was stable and equal to the service time ratio of the two anodes.

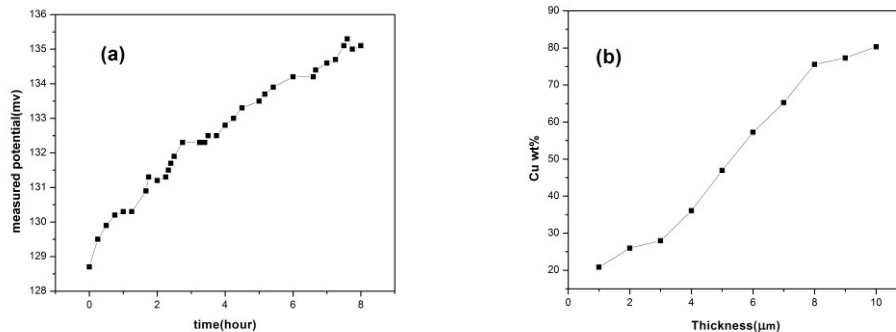


Figure 3- 8 The variation of free copper ion concentration in the bath and the copper content in the coating during Ni/Cu plating in which the service time ratio of the Cu anode and Ni anode was 0.3. (a) the potential change of the electrode for free copper ion measurement, 112.5mV and 135.8mV correspond to  $\text{Cu}^{2+}$  concentrations of  $10^{-6}\text{M}$  and  $10^{-5}\text{M}$ , respectively. The relationship between the

potential  $E$  and  $\text{Cu}^{2+}$  concentration is:  $\log [\text{Cu}^{2+}] = (E - 252.3)/23.3$  (b) Variation of copper content with the coating thickness of the Ni/Cu plating layer.

An electrochemical examination was conducted to reveal the electrode processes both on the anode and cathode. Fig. 3-9 shows the cyclic voltammogram obtained on the copper anode surface in the Ni/Cu citrate plating bath used for beaker plating in this study. Two curve branches were recorded in the cyclic voltammogram. In the anodic branch, the peak is attributed to copper oxidation leading to the formation of  $\text{Cu}^{2+}$  ions, while in the cathodic branch, the increase of the reduction current is from Ni/Cu codeposition.  $\text{Cu}^{2+}$  and  $\text{H}^+$  reduction peaks are not apparent because of the high cathodic current efficiency and the low  $\text{Cu}^{2+}$  concentration shown in Fig. 3-2 and Fig. 3-8, respectively.

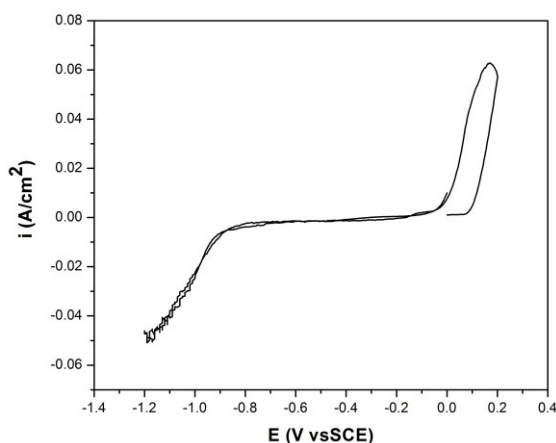


Figure 3-9 Cyclic voltammogram obtained on the copper surface in Ni/Cu citrate plating bath.

Also, when the Ni anode was working and the Cu anode was disconnected from the power supply, the electric potential distribution on the copper anode surface was measured before

and during the electrodeposition experiment. The measured potential distribution is shown in Fig. 3-10.

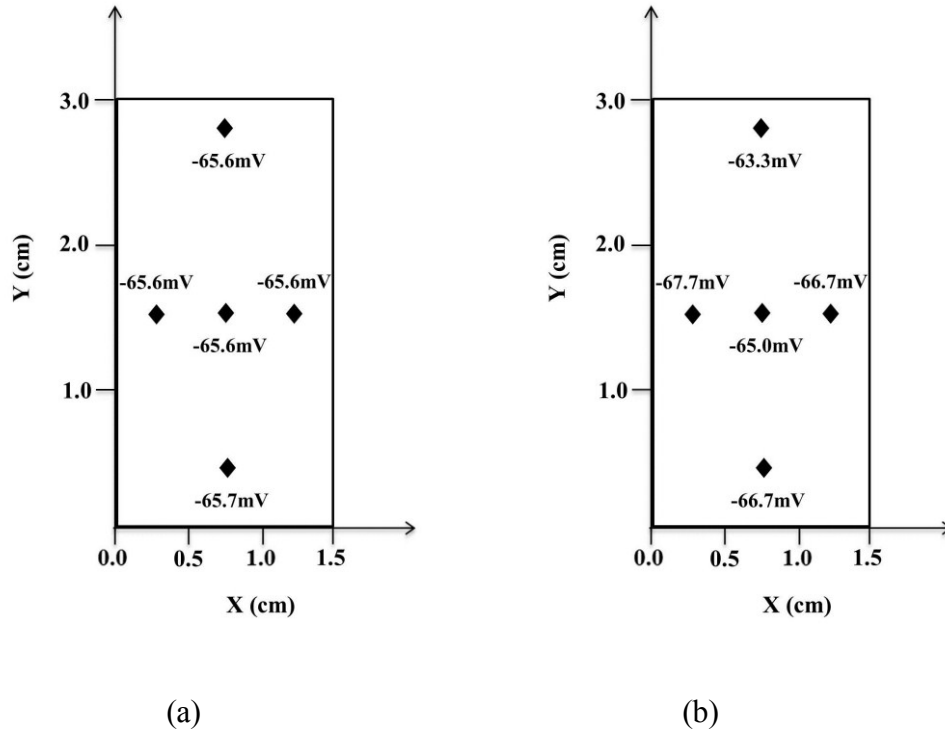


Figure 3-10 Potential distribution on a 15×30 mm copper plate surface in the Ni/Cu citrate bath during electroplating. The potential values are vs SCE. (a): before electroplating, the copper plate is equipotential with a potential of -65.6 mV vs SCE. (b) when copper anode is disconnected from the power supply, a small potential difference occurred across the Cu surface.

Based on the experimental results shown in Fig. 3-8, 3-9 and 3-10, the linear increase of copper content both in the solution and in the coating cross section as recorded in Fig. 3-8 can be explained.

Before electroplating, the copper plate was equipotential, which had a potential of -65.6 mV vs SCE (Fig. 3-10(a)). When electrodeposition was proceeding with the Ni anode

connected to the power supply, the potential of the disconnected Cu anode changed slightly compared to that before plating, as indicated in Fig. 3-10(b). A slight potential difference was also observed across the Cu surface, which can be attributed to the influence of the ionic current in the electrolyte on the measurement.

It is noticeable from Fig. 3-10 that the surface potential of the copper anode varies in a small range around -66 mV vs SCE when disconnected from the power supply. According to the data in Fig. 3-9, this potential value corresponds to the anodic current density of  $2\text{mA}/\text{cm}^2$ , indicating the rate of continuous dissolution of copper metal into the bath during electrodeposition when the Ni anode is working and the Cu anode is disconnected. The source of copper ions during electrodeposition has hence been found.

The origin of the copper anode surface potential can be ascribed to the interaction between the copper metal and the electrolyte. At the interface of copper and the electrolyte, the equilibrium condition requires the equal electrochemical potential for electrons on both sides. This causes the transfer of electrons across the interface. It also changes the surface charge density as well as the electric potential of the Cu metal.

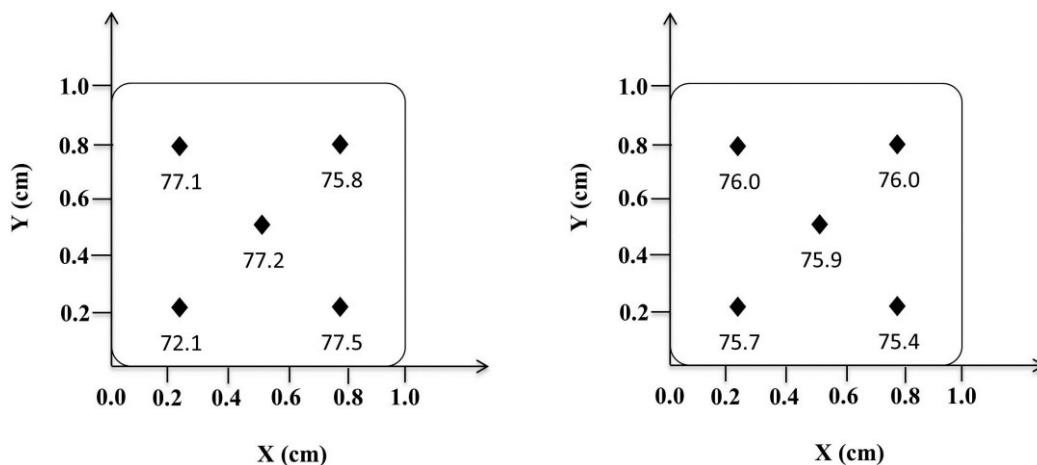
The unusual phenomenon revealed in Fig. 3-8 can be used as a method to increase the Cu content in the Ni/Cu electroplating bath, i.e., placing bulk Cu metal into the bath during electrodeposition can effectively increase the Cu content in the electrolyte.

This simple approach has the advantage of only adding  $\text{Cu}^{2+}$  into the solution without introducing other chemical species like  $\text{SO}_4^{2-}$  which is what happens when adding copper sulfate into the bath.

### **3.3.4 Color control of the Ni/Cu coating**

Two Ni/Cu deposition samples were fabricated from barrel plating for 5 hours at two different pH levels of 4.5 (low pH) and 5.1 (high pH). The coating thickness was about 5 micrometers. The composition of these two coating films was measured by EDX using 5 points measurement as shown in Fig. 3-11, which reveals that their compositions are almost identical. Surprisingly, their colors are not as expected, based on the common knowledge that the color of the alloy depends on the composition; thus, the same composition should yield the same color. As clearly displayed in Fig. 3-12, the colors of the coatings are considerably different when the copper content is over 75 wt%. The color of the coating developed at low pH level is close to that of pure copper, whereas the color of the coating obtained at high pH level is similar to pure nickel.

To exclude the possibility that the color difference between the two samples might be the result of a non-uniform composition distribution (for example, the copper content is relatively high on the surface of the sample obtained from the pH 4.5 bath), an EDX line scanning across coating thickness was performed, which shows excellent composition consistencies, as seen in Fig. 3-13.



(a)

(b)

Figure 3- 11 EDX measurement result of composition distribution of two Ni/Cu samples deposited in citrate bath at pH levels of (a) 4.5 and (b) 5.1. The numbers inside the squares are Cu weight percent values.

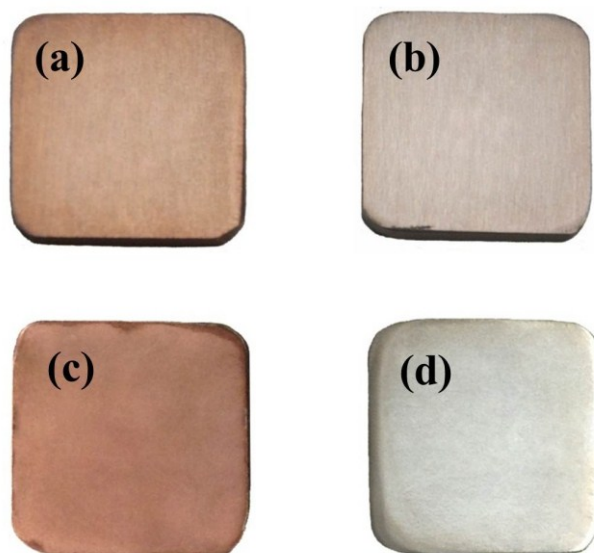


Figure 3-12 Photo of Ni/Cu samples deposited in the citrate bath at pH levels of (a) 4.5 and (b) 5.1. For comparison, pure copper and pure nickel samples are also presented in (c) and (d).

SEM and XRD examinations were carried out to identify the origin of the diverse coating colors caused by altering the pH level in the plating bath. Fig. 3-14 shows the surface morphologies of the two samples, which are strongly influenced by the electrolyte pH. The sample plated at the low pH level has nodular particles of around a few micrometers in size, while the surface of the sample obtained at the high pH level is relatively smoother.

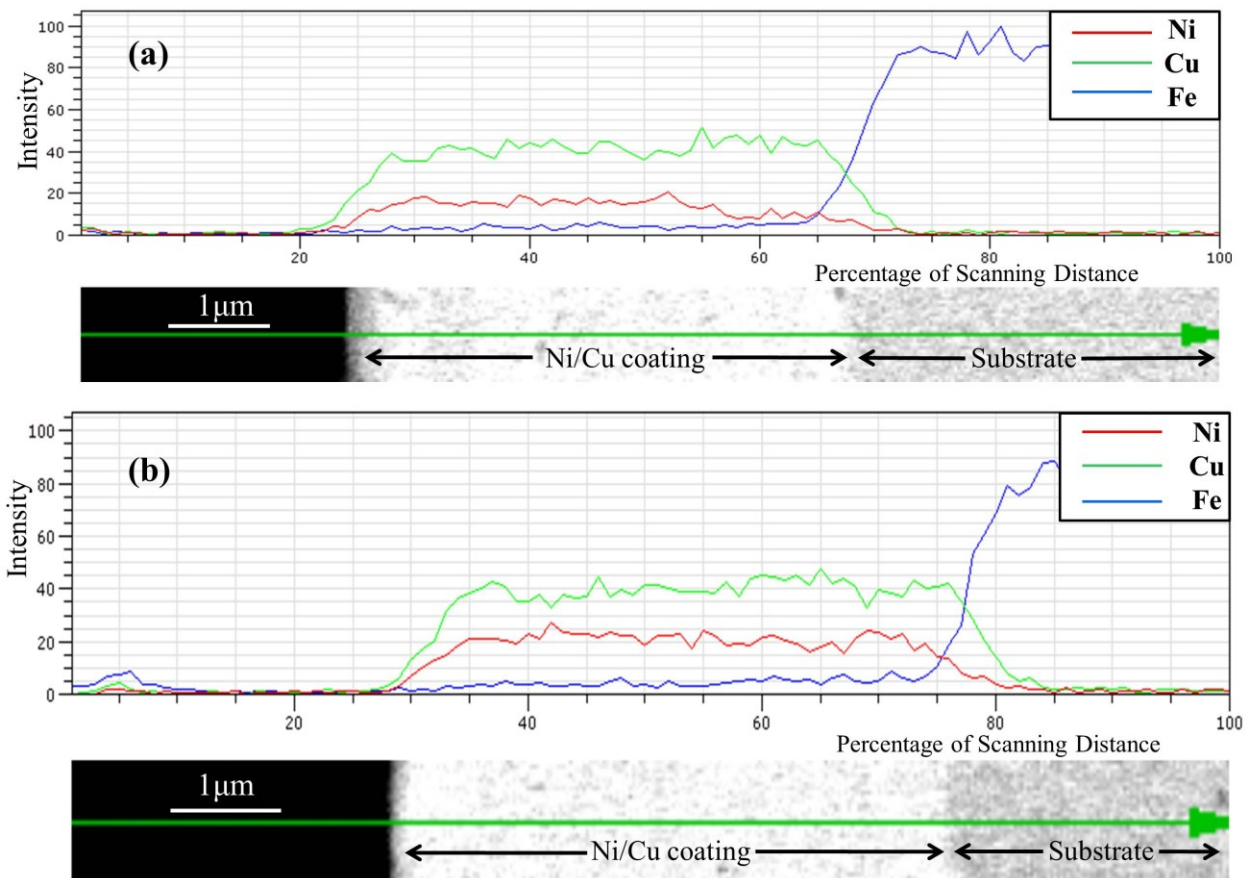


Figure 3-13 EDX line scan result of the cross sections of two Ni/Cu samples electroplated in the citrate bath at pH levels of (a) 4.5 and (b) 5.1.

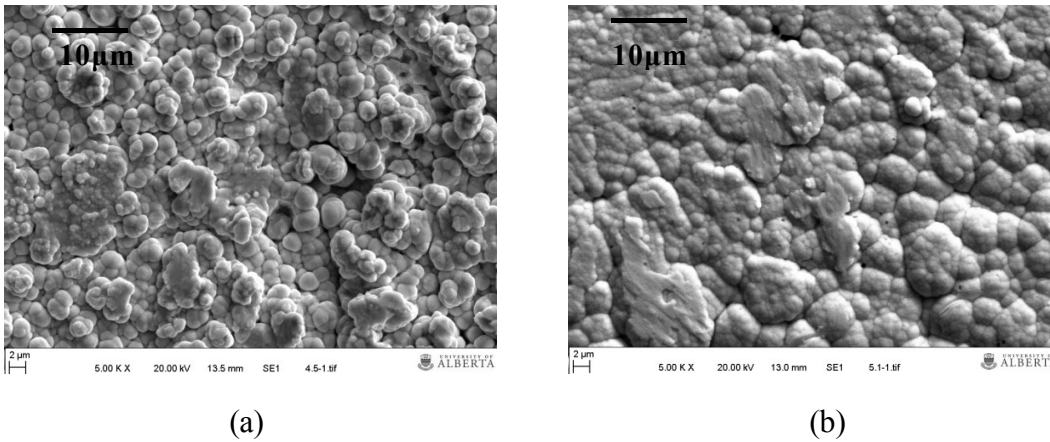


Figure 3-14 Comparison of surface morphologies of Ni/Cu coating samples fabricated at pH levels of (a) 4.5 and (b) 5.1.

The change of the surface morphology with the bath pH can be explained by the hydrogen evolution that occurred at the cathode surface. The lower pH resulted in enhanced hydrogen evolution, which promoted the electrolyte convection and the migration of metal ions in the vicinity of the coating surface, at the existing particles on the surface, where the fluid flow rate of the electrolyte is faster than that of the surrounding area<sup>8</sup>. Consequently, these existing particles grew preferentially at a faster deposition rate. In contrast, the coating film formed in the high pH bath was exposed with less convection and the growth of particles on the coating surface were less accelerated, leading to a smoother surface morphology.

Fig. 3-15 shows the results of X-ray diffraction analysis of the Ni/Cu films grown at two different pH levels. The values were re-scaled such that the intensity of the (111) plane in each diagram was normalized to 100. Table 3-2 shows the diffraction angles of different planes. The XRD peaks of the coating layer produced in the high pH bath are shifted towards higher angles compared with those of the film plated in the low pH bath, and the higher the

diffraction angle, the larger the shift, except for the (222) peak. The grain size estimation in Table 3-2 used Scherrer equation <sup>11</sup> which is given by

$$\chi_s = \frac{0.9\lambda}{FWHM \cos \vartheta} \quad (3-17)$$

Where  $\chi_s$  is the grain size,  $\lambda$  the X-ray wavelength and  $\theta$  the diffraction angle.

Much effort has been made to explore what cause the change in the microstructures of nickel or nickel copper alloy with electrolyte pH <sup>12-14</sup>. It has been suggested that the change is caused by the influence of the inhibiting species such as H<sub>2</sub> and Ni(OH)<sub>2</sub>, which are generated during the deposition in the bath. In a work similar to the present study<sup>14</sup>, the Ni/Cu alloy was codeposited in constant potential mode at 2 different pH levels, and the coating films formed were found to be different in both composition and texture. In contrast, from Fig. 3.15, it is obvious that the two Ni/Cu coatings with the same composition have the identical intensity ratios between different peaks. The latter suggests that the effect of pH on texture formation in the current study is insignificant.

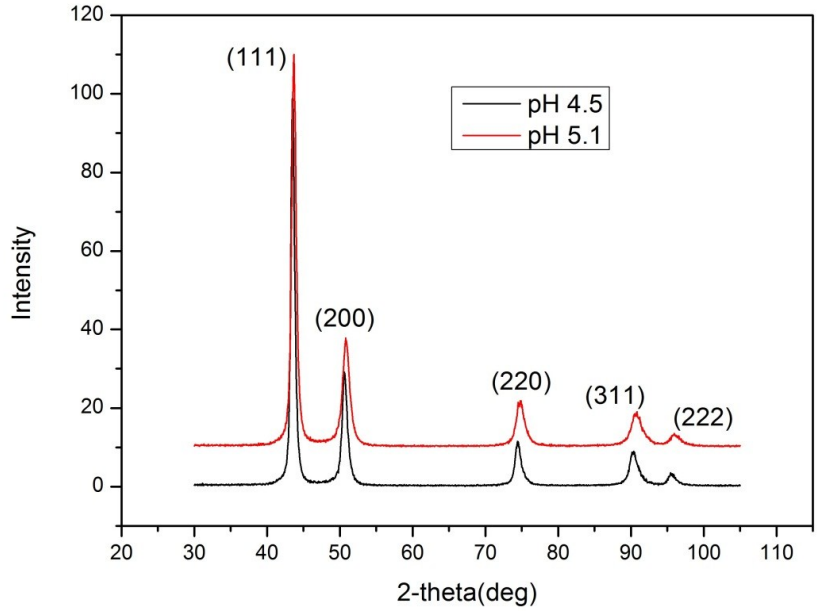


Figure 3-15 patterns of Ni/Cu coating films obtained at pH 4.5 and 5.1 in the citrate bath.

**Table 3-2 Data from XRD patterns of Ni/Cu coating films obtained at different pH levels**

Samples	pH	2-Theta					grain size(nm)*
		(111)	(200)	(220)	(311)	(222)	
Ni-Cu Flms	4.5	43.55	50.65	50.65	90.15	95.45	13.4
	5.1	43.69	50.80	50.80	90.75	95.95	12.0

\* The grain size is the average of the calculating result with Sherrer's formula from the data of (111), (200), (220) and (311) diffraction peaks.

By comparing the results from the two investigations, it can be concluded that the observation of different texture formation in Ref. 14 was due to the difference in the Ni/Cu

alloy composition, and the shift of the X-ray diffraction angle in this investigation originated from pH variation in the plating bath.

The XRD peak shifting is generally related to the macro-strain present in the coating<sup>15</sup>. Using two-dimensional X-ray diffraction technique, the residual stress in the two Ni/Cu samples in this work was quantitatively evaluated by the following equation, as suggested in Ref. 16:

$$\sigma_{\varphi} = \frac{k}{d_{\psi=0}} \cdot \frac{E}{1+\nu} \quad (3-18)$$

In which  $\sigma_{\varphi}$ ,  $E$  and  $\nu$  are residual stress, Young's modulus and Poisson's ratio of the material, respectively;  $k$  is the slope of the  $d$ - $\sin^2\psi$  curve and  $d_{\psi=0}$  denotes the intercept of the curve. The measured  $d$ - $\sin^2\psi$  curves for the Ni/Cu samples developed at pH 4.5 and 5.1 are presented in Fig. 3-16.

The calculation was carried out using Equation (3-18) and the data in Fig. 3-16 and Ref.17 and 18, as presented in Table 3-3.

The calculations demonstrate that both samples have compressive stress. This can be explained with the deposition bath formula which contains saccharin as an additive. In fact, saccharin is typically used to refine grains and reduce stress and may give rise to compressive stress if sufficiently added into the bath<sup>15, 19, 20</sup>.

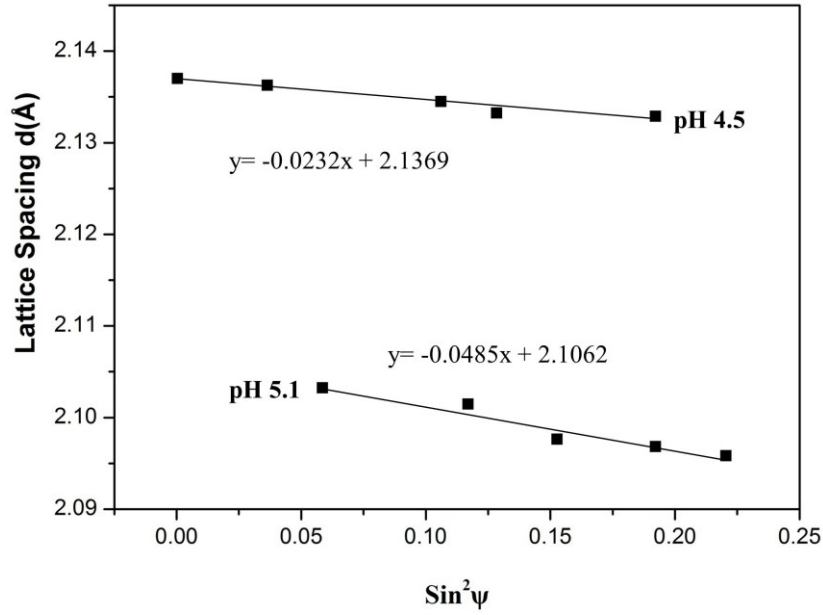


Figure 3-16  $d\text{-sin}^2\psi$  curves and data fitting of XRD2 results for Ni/Cu samples.

**Table 3-3 Calculation of the residual stress of Ni/Cu samples**

	$k(\text{Å})^*$	$d_{\psi=0}(\text{Å})^*$	$E(\text{GPa})^{**}$	$\nu^{***}$	$\sigma_{\varphi}(\text{GPa})$
pH4.5	-0.0232	2.1369	171	0.36	-1.25
pH5.1	-0.04855	2.1062	125	0.36	-2.17

\*  $k$  and  $d_{\psi=0}$  are taken from Fig. 3-15.

\*\* Young's modulus was measured by nanoindenter.

\*\*\* The value of Poisson's ratio of the Ni/Cu alloy is from Ref. 17 and 18.

Tables 3-2 and 3-3 also show that the sample developed at pH 5.1 has higher Bragg diffraction angles which means lower lattice spacing, and correspondingly is subjected to higher compressive stress. The plausible explanation of this phenomenon would be that at lower pH level of 4.5, a more severe hydrogen evolution reaction occurred on the cathode surface and more hydrogen atoms were co-deposited into the Ni/Cu matrix. According to Wei<sup>21</sup>, the co-deposited hydrogen atoms are trapped in the coating film, and release out afterward. This releasing process decreases the occupied volume of the metal, resulting in tensile stress in the deposit. Based on this theory and the stress-reducing effect of saccharin, it is reasonable to deduce that under the combined influence of the saccharin addition and the hydrogen evolution reaction and co-deposition, the sample fabricated at lower pH level would yield lower compressive stress.

Now it is possible to apply the above results to tentatively interpret the color dependence of the Ni/Cu coating film on electrolyte pH.

Generally, the optical properties of a solid are related to the electrons' band structure, lattice vibration and surface morphology<sup>22-24</sup>, which can therefore affect the color of the solid. It is also generally accepted that the residual stress significantly influences thin film's lattice vibration characters<sup>25-27</sup>. A change in the lattice vibration can in turn alter the band structure<sup>28,29</sup> and, hence, the color of the solid. On the other hand, the optical phonon spectrum, which is thought to be related to the absorption and reflection processes of the visible light<sup>22</sup>, is also influenced by the residual stress<sup>25-27</sup>, and consequently the metal color is affected. To understand and quantitatively describe those physical processes of the phonon-electron interactions inside the Ni/Cu alloy require more in-depth experimental and theoretical

work. Because we were conducting an experimental investigation, we present here only a qualitative explanation.

Furthermore, the difference in surface morphology due to the different bath pH as shown in Fig. 3-14 can generate diverse optical properties<sup>23,24</sup>, such as scattering characters of the visible light, which may also affect the surface color of the metal.

### **3.4. Conclusions**

The issues of composition control, color adjustment and temperature selection in Ni/Cu codeposition in the citrate bath with sulfate have been addressed, and some solutions have been provided to facilitate the commercialization of this engineering technique.

It has been demonstrated that maintaining the stability of pH in the citrate bath is a prerequisite for compositional uniformity of the Ni/Cu codeposition layer. Besides adding nickel chloride and a sufficient amount of citrate to the bath, a stable pH can be achieved mainly by connecting nickel and copper anodes to two separate power supplies and by properly choosing their areas. The coating composition is approximately equal to the anode current ratio.

In adjusting the electrolyte content, placing bulk Cu metal into the bath during electrodeposition can effectively increase the Cu content in the electrolyte and prevent the issues that result from adding salt to the bath.

To achieve the utmost sustainability, 60 °C is a desirable selection of the plating temperature. At this temperature, the precipitation of  $\text{Cu}_2\text{H}_1\text{Cit}\cdot 2\text{H}_2\text{O}$  can be effectively avoided from the electrolyte because of its elevated solubility in the plating bath.

The color of the Ni/Cu coating in the citrate bath was found to vary with the electrolyte pH level. Conducting the electroplating at a higher pH level makes the color of the coating film closer to the color of nickel metal.

Meanwhile, the XRD analysis demonstrates that if the alloy coating composition was maintained constant when deposition was performed at different pH levels, the texture remained unchanged but peak positions in the X-ray diffraction spectrum of the Ni/Cu alloy changed; the film obtained from plating at the lower pH level has lower diffraction angles and, thus, higher lattice spacing, as well as lower compressive residual stress inside the coating film. The underlining mechanisms on the bath-pH dependent formation of compressive stress during plating were discussed. The pH-dependence is believed to result from a combined influence of the stress reduction effect of saccharin and the promoted hydrogen evolution reaction at the lower pH level.

The color dependence on the electrolyte pH can be tentatively explained that the residual stress variation in the coating film can influence the electrons' band structure and the lattice vibration characters, specifically, the optical phonon spectrum. As a result, the coating's color is affected.

The morphological change of the coating with the bath pH may also contribute to the color variation.

### 3.5 References

- 1 T. A. Green, A. E. Russell, S. Roy, J. Electrochem. Soc., Vol. **145**, No. 3, March 1998.
- 2 S. Rode, C. Henninot, and M. Matlosz, J. of Electrochem. Soc., 152 (4) C248-C254 (2005).
- 3 B. H. Prescott, Trans. Inst. Met. Finish., **36**, 93 (1959).
- 4 E. Chassaing, K. VU Quang, J. of App. Electrochem. **17** (1987) 1267-1280.
- 5 R. Y. Ying, P. K. Ng, J. Electrochem. Soc. **135**, 2964 (1988).
- 6 E. J. Podlaha, C. Bonhôte, and D. Landolt, Electrochim. Acta, **39**, 2649 (1994).
- 7 A. J. Bard, L. R. Faulkner, Electrochemical Methods, 2nd edition.
- 8 T. Watanabe, Nano Plating - Microstructure Formation Theory of Plated Films and a Database of Plated Films, Elsevier, 1st Edition, 2004.
- 9 K. Murase, T. Honda, T. Hirato, and Y. Awakura, Metallurgical and Materials Transactions B, 29B, Dec. 1998—1197.
- 10 J. O. Bockris, Modern Electrochemistry, 2nd edition, Plenum Press, New York, 1998.
- 11 A. Monshi, M. R. Foroughi, M. R. Monshi, World Journal of Nano Science and Engineering, 2012, 2, 154-160.
- 12 M. Motoyama, Y. Fukunaka, T. Sakka, and Y. H. Ogata, Journal of the Electrochemical Society, 153 (7) C502-C508 (2006).
- 13 K.C. Chan, W.K. Chan, N.S. Qu, Journal of Materials Processing Technology 89-90

- (1999) 447-450.
- 14 M. Alper, H. Kockar, M. Safak, M. C. Baykul, *Journal of Alloys and Compounds* 453 (2008) 15–19.
- 15 E. Pellicer, A. Varea, S. Pané, K.M. Sivaraman, B.J. Nelson, S. Suriñach, M.D. Baró, J. Sort, *Surface & Coatings Technology* 205 (2011) 5285–5293.
- 16 M. Allahkarami, J. C. Hanan, *Powder Diffraction* 29 (2), June 2014.
- 17 P. G. Sanders, J. A. Eastman and J. R. Weertman, *Acta mater.* Vol. 45. No. 10. 4019-4025. 1997.
- 18 K. S. Siow, A. A. O. Tay and P. Oruganti, *Materials Science and Technology* March 2004 Vol. 20, 285.
- 19 Y. Li, X. Huang, J. Yao, and X. Deng, *Advanced Materials Research* Vols. 189-193 (2011) pp 911-914.
- 20 S. R. Brankovic, B. Kagajwala, J. George, G. Majkic, G. Stafford, P. Ruchhoeft, *Electrochimica Acta* 83 (2012) 387–393.
- 21 Wei R, *Plating*, 57, 1231 (1970).
- 22 J. D. Patterson, B. C. Bailey, *Solid-State Physics*, Springer-Verlag, Berlin Heidelberg,

2007.

23 D.S. Martin, N.P. Blanchard, P. Weightman, *Surface Science* 532–535 (2003) 1–7.

24 A. I. Belyaeva, A. A. Galuza, A. A. Savchenko, and K. A. Slatin, *Bulletin of the Russian Academy of Sciences. Physics*, 2011, Vol. 75, No. 5, pp. 721–724.

25 M. F. Doerner and W. D. Nix, *CRC Crit. Rev. Solid State Phys. Mater. Sci.*14, 225 (1988).

26 Li Sun, Yan-Feng Chen, Lei He and Chuan-Zhen Ge, De-Sheng Ding, Tao Yu and Ming-Sheng Zhang, Nai-Ben Ming, *PHYSICAL REVIEW B*, VOLUME 55, NUMBER 18, 1997.

27 D. Chen, Y. Luo, L. Wang, H. Li, G. Xi, Y. Jiang, Z. Hao, C. Sun, and Y. Han, *Journal of Applied Physics*, 101, 053712 (2007).

28 I. Delgado, H. Gollisch and R. Feder, *Solid State Communications*, Vol. 88, No. 10, 789-794, 1993.

29 I. Yu. Sklyadneva, R. Heid, P. M. Echenique, K.-B. Bohnen, and E. V. Chulkov, *PHYSICAL REVIEW B* 85, 155115 (2012).

**Chapter 4 Mechanistic investigation of the magnetic field effects on nickel  
electro-deposition**

## 4.1 Introduction

Superimposing magnetic field in electrodeposition is a promising way to tailor the deposit properties. Numerous studies have been reported in the past years. The magnetic field has been found to play a role in altering the electrolyte properties<sup>1</sup>, affecting electrolytic mass transport<sup>2,3</sup>, and changing the structure and morphology of the deposits<sup>1,4</sup>. However, its effect on electrode kinetics is still a subject of controversy and experimental results tend to prove its inutility<sup>1, 5</sup>.

Considerable effort has been devoted to understanding the mechanisms governing the morphological change in the deposit obtained in the presence of the magnetic field. Various hypotheses have been proposed. Under a homogeneous magnetic field, it is well established that the morphological change originates from the magnetohydrodynamic (MHD) effect, which produces additional convection in the electrolyte. Also, most investigations have been conducted in the two magnetic conditions: a magnetic field parallel or perpendicular to the electrode surface.

The parallel magnetic field is generally believed to reduce the deposit's roughness. The corresponding explanations include the enhanced deposition rate that resulted in finer grains<sup>6</sup>; the enhanced adsorption of additives and inhibitors<sup>7-9</sup>; the removal of the hydrogen bubbles<sup>10</sup>; and the micro-MHD convection in the diffusion layer that blew off the concentration fluctuation<sup>11</sup>.

For the vertical magnetic field, Aogaki *et al.* proposed that the micro-MHD effect could partially suppress the nucleation and lead to a smoother deposit<sup>12,13</sup>. Matsushima *et al.*<sup>14</sup> ascribed this nucleation suppression to the spiraling adatom flux around the nucleus that hindered the adatoms from entering the matrix. However, other investigators<sup>15</sup> found rougher and more diverse coatings in the vertical magnetic field.

In addition, the fine-grained magnetic domains<sup>4</sup> and the induced magnetic dipolar<sup>16</sup> in ferromagnetic metals are also considered to be responsible for the remarkable influence on the deposit morphology.

The fluid flow pattern on the electrode surface also plays an important role in morphology-forming. Its interaction with Lorentz force has been reported to have significantly affected the surface morphologies of the coating<sup>7, 17</sup>.

Although the available mechanisms on surface modification arisen from the MHD effect seem simple, some experimental observations are still not clearly explained. For example, in plating iron or its alloys, the elongated grains were observed in the presence of parallel magnetic field<sup>17-19</sup> and the columnar structures were found to be developed in the vertical magnetic field<sup>15,20</sup>. In these two cases, the detailed perspective of the MHD effect cannot be defined in terms of its role in surface modification.

In contrast to the extensive investigations on the effect of the magnetic field on deposit morphology, there have been relatively fewer studies to date on how the magnetic field affects the structure of the deposits. The relationship between the crystal texture and the other deposit properties, such as surface morphology, is still unclear. In the previous studies, the structure change was ascribed to the easy magnetization axis<sup>21</sup>, the increase of definite inhibiting species which produced Ni(OH)<sub>2</sub> and facilitated specific modes of growth<sup>7, 8</sup>, and the minimization of the system's free energy including the surface energy and the magnetic free energy<sup>22-24</sup>.

In the present work, nickel plating was performed under either the parallel or vertical magnetic fields. The coating surface was characterized by electrochemical analysis, scanning electron microscope (SEM), atomic force microscope (AFM) and X-ray diffraction (XRD). These

characterizations provide new insights on the MHD effect. New intuitive theoretical models have been established to provide distinct patterns of the deposit surface and crystal texture modification that arising from the interaction between the Lorentz force and the fluid flow in the parallel and vertical magnetic fields. These new models are in excellent agreement with the experimental observations from this investigation and in the literature.

## 4.2 Experimental

Nickel was electrodeposited galvanostatically (current density =  $6.7\text{mA/cm}^2$ ) with a 3-electrode system. An  $0.4\times 0.8$  cm nickel foil was employed as the counter electrode. The reference electrode was a standard calomel electrode (SCE). The working electrode (electroplating substrate) was a copper plate with a dimension of  $3\times 3\times 0.7$  mm. The substrate was ground, polished and pre-treated through degreasing and activation processes before plating.

The electroplating experiments were conducted at  $22\pm 2^\circ\text{C}$ , and no agitation was provided except for one experiment that was designed to study the influence of forced convection on the deposit structure and morphology. In the latter experiment, the deposit setup was placed on the table of a drill press rotating at the speed of 9.3Hz which provided a mechanical vibration in the electrolysis system.

The electrolyte solution consisted of 0.05M  $\text{NiSO}_4\cdot 6\text{H}_2\text{O}$ , 0.1M boric acid and 0.1M sodium sulfate anhydrate as the supporting electrolyte. The solution pH was maintained at 4.0. All chemicals were analytical reagent-grade. Deionized water was used in preparing the electroplating solutions.

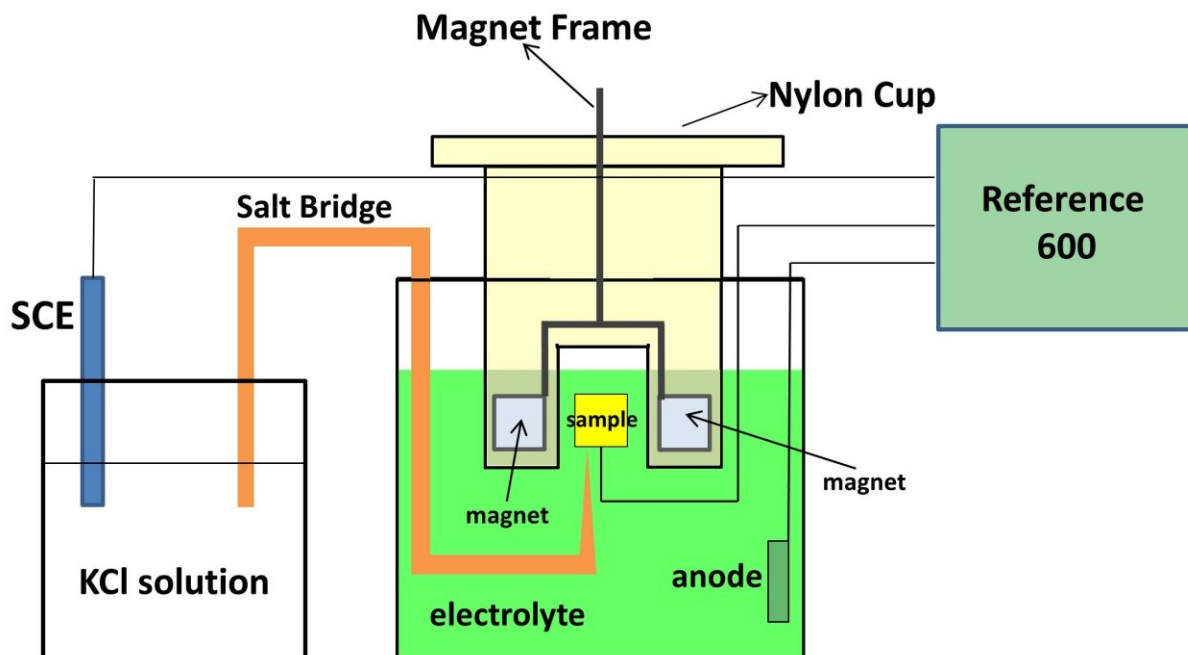


Figure 4-1 Schematic diagram of the electrolysis system in the presence of the magnetic field.

The experimental setup is shown in Fig. 4-1. A specially designed nylon cup was used in the experiment. The sample was placed in the middle of a hole in the nylon cup. A pair of permanent magnet sets was mounted onto an austenitic stainless steel frame, which was installed around the sample and the hole in the nylon cup. The diameter of the hole was 6 mm and the distance between the pair of magnet sets was 15 mm. Each magnet set consisted of four cylindrical magnets which were magnetized parallel to their axes. With such an arrangement, the magnetic field inside the hole where the sample was placed was measured to be 0.18T.

Surface characterization was conducted using JEOL (JSM-6301FXV) field emission scanning electron microscope (SEM) with the operating conditions being denoted in the respective images presented. The atomic force microscope (MFP-3D, Asylum Research) was employed to reveal some detailed features of the coating surfaces. X-ray diffraction measurements were carried out

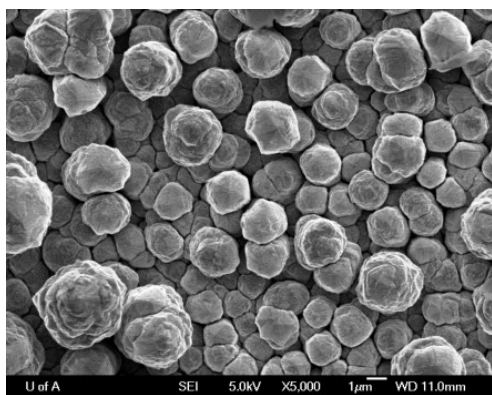
in Rigaku-Ultima IV X-ray diffractometer using Cu K $\alpha$  radiation with a wavelength of 0.1541 nm. The 2 $\theta$  values were from 10 $^\circ$  to 110 $^\circ$ . The electrochemical characterization was done with a Gamry Reference 600 electrochemistry work station.

## 4.3 Results and discussion

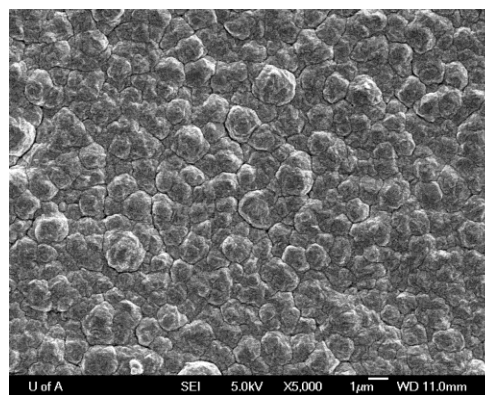
### 4.3.1 Characterization results

#### 4.3.1.1 Morphological characterization

Fig. 4-2 shows the SEM images of the nickel coatings developed in the nickel sulfate bath for 40 minutes. In Fig. 4-2(a), when the magnetic field was absent, the coating consists of stacked nodular particles or “cauliflowers.” These nodules are believed<sup>25</sup> to originate from the pre-existing fine protrusions on the substrate surface, and grow in the process of plating because of the well-known fact that the metal ion discharge occurs preferentially at the pointed sites of the deposit surface, and because the flow rate of the electrolyte at the pointed locations is faster than it is at the surrounding areas, which lead to a higher deposition rate. The rounded appearance of the nodules is attributed to the surface energy minimization during the deposition.



(a)



(b)

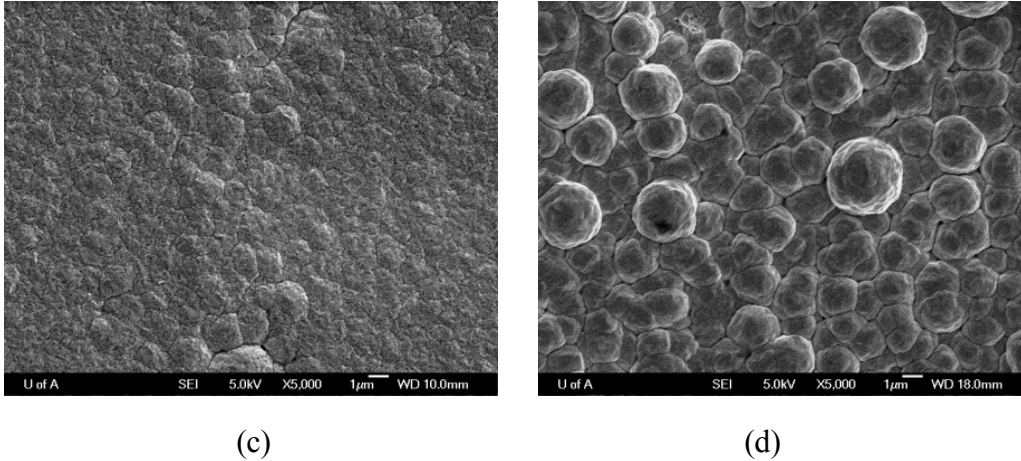


Figure 4-2 SEM images of deposited nickel morphology in sulphate bath under various magnetic field conditions: (a)  $B=0$ ; (b)  $B=0.18\text{T}$ , parallel; (c)  $B=0.18\text{T}$ , vertical; and (d)  $B=0$  with mechanical vibration.

The application of the magnetic field parallel to the cathode surface yielded a smoother deposition, shown in Fig. 4-2(b), which is consistent with many previous observations. However, contrary to some existing results that a vertical magnetic field leads to rough coating<sup>15, 20</sup>, a smoother coating was obtained from the vertical field, as seen in Fig. 4-2(c).

#### 4.3.1.2 Structural characterization

Fig. 4-3 shows the results of X-ray diffraction analysis of nickel deposition. The intensity of the diffraction has been re-scaled such that the intensity of (111) plane in each diagram was normalized to 100. The XRD peak intensities of (200), (220) and (311) for different experiment conditions are further plotted in Fig. 4-4 for coatings obtained under different plating conditions.

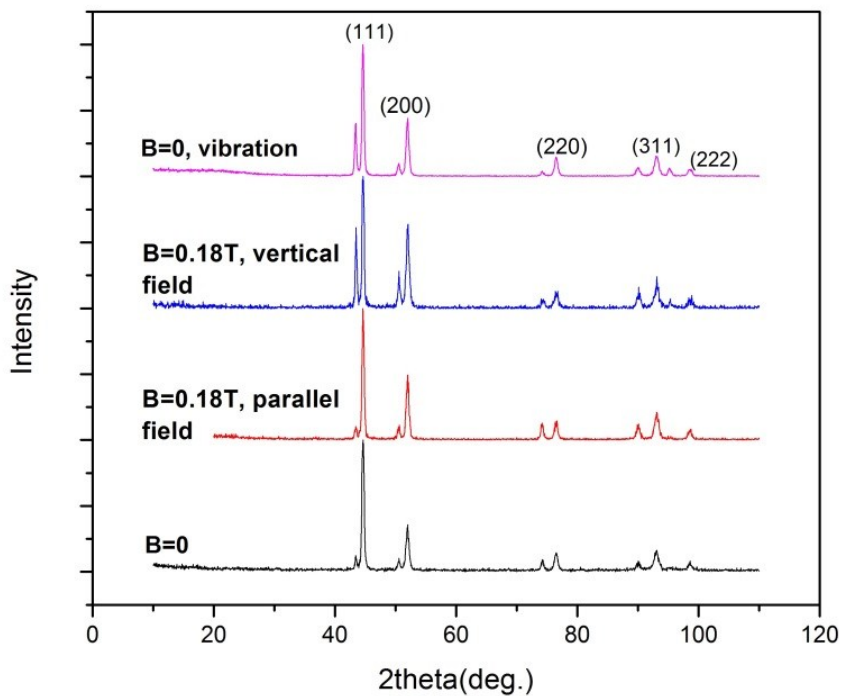


Figure 4-3 XRD spectra of nickel deposited in a sulphate bath under different magnetic field situations. The intensity of (111) peak has been set to 100. All the unmarked peaks are from the Cu substrate.

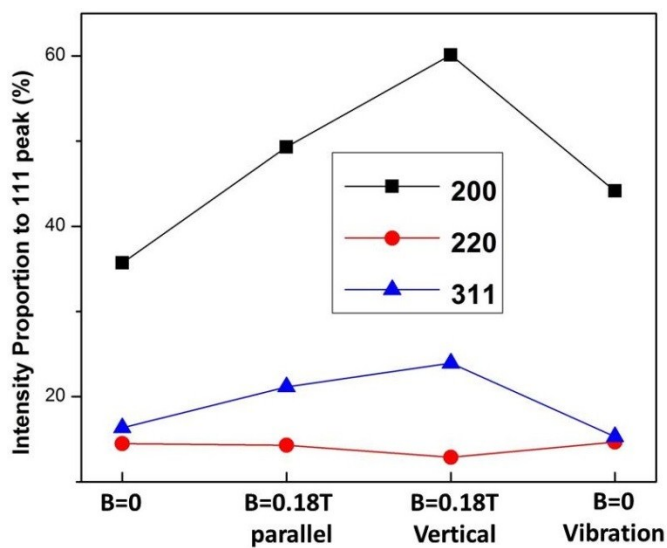


Figure 4-4 XRD peaks intensity comparison diagram for various experimental conditions.

The X-ray diffraction patterns in Fig. 4-3 clearly demonstrate that (111) plane is the predominant plane for all deposition conditions in this investigation, which is in agreement with previous research findings that without magnetic field, the work required to form (111) plane in a face-centered cubic metal was the lowest<sup>26</sup>; and is also similar to the results observed by Brillas *et al.*<sup>27</sup> that (111) plane is dominant for nickel deposited in Watts bath under magnetic fields.

Both Fig. 4-3 and Fig. 4-4 suggest that the application of a parallel magnetic field promotes the (200) plane deposition. This enhanced intensity of the (200) plane is even stronger in the presence of the vertical magnetic field. The (311) plane exhibits similar behaviour to the (200), while the (220) peak intensity appears insensitive to the magnetic fields. These results indicate the higher efficiency of the vertical magnetic field in promoting the (200) and (311) growth. The change in the (200) deposition by the magnetic field will be discussed further in the following sections.

#### **4.3.1.3 Electrochemical characterization**

Fig. 4-5 displays the chronopotentiometry curves. Notably, in Fig. 4-5(a), the vertical magnetic field resulted in the highest chronopotentiometry curve. Because the magnetic field and the electric current are believed to be parallel in this configuration, the MHD stirring is expected to be negligible. The additional ion supply in the present work is believed to be from, first, the MHD stirring in the bulk electrolyte, which resulted from the Lorentz force. The side view of the nickel ions migrating from the anode to the cathode is illustrated in Fig. 4-6. For the special geometry of the electrodeposition cell in this research (the sample was inside a narrow hole of the nylon cup), the migration route of the nickel ions in the bulk electrolyte are perpendicular to the magnetic field due to the hole. This is the case regardless of the direction of the field, either

perpendicular or parallel to the sample surface. It allows for the maximum MHD stirring in the electrolyte, which increases the nickel ion supply around the sample both for the perpendicular and parallel field cases. This result is similar to that reported in Ref. 28, in which it was confirmed that the Lorentz force was still dominant in the vertical magnetic field case. Second, the result is from the MHD convection to the nickel ions moving along the cathode surface. The directions of these moving ions are perpendicular to the magnetic field and thus subjected to the maximum Lorentz force. This effect will also be explained in detail in the following section.

Now a question arises: to what extent do the MHD convection to the bulk electrolyte and the resulting potential increase contribute to the crystal texture formation and morphology change of the deposit?

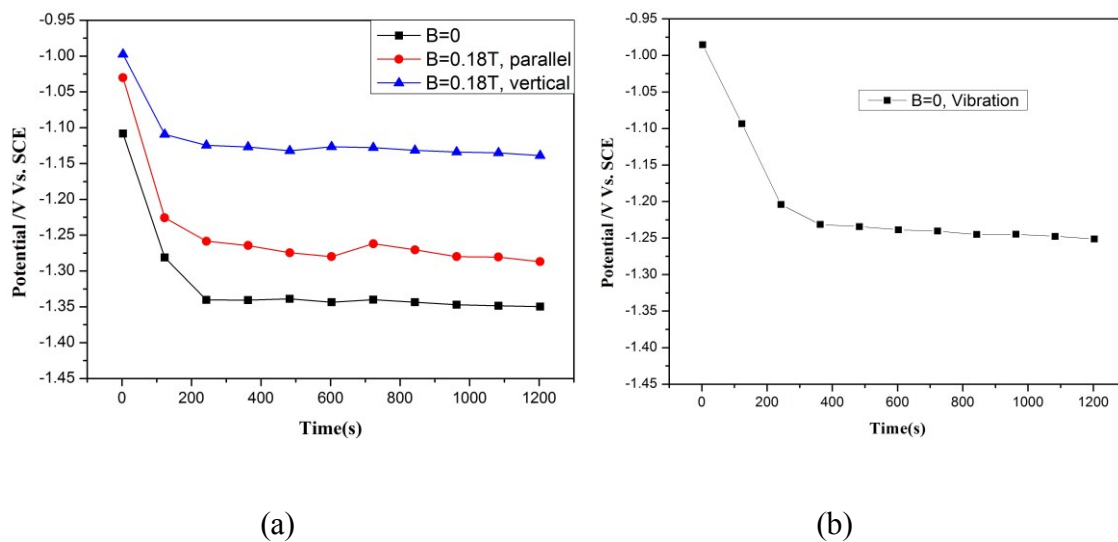


Figure 4-5 Chronopotentiometry curves during Ni deposition in different experimental conditions.

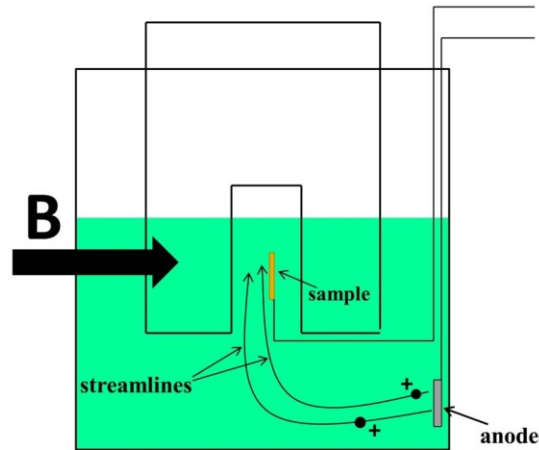


Figure 4-6 Illustration of the migration route of the Ni ions from the anode to the cathode in the cell.

For comparison, an electrodeposition experiment under the same conditions as described in the experimental section was performed without an application of the magnetic field but with mechanical vibration at a frequency of 9.3Hz introduced during the deposition as the source of forced convection. The magnetic stir bar was not used in order to avoid the disturbance from its magnetic field. Fig. 4-5(b) shows the recorded chronopotentiometry curve obtained under the mechanical vibration. Although the electrode potential was elevated by the forced convection to a slightly higher level than that of the parallel magnetic field without agitation in Fig. 4-5(a), the nickel film deposited as seen in Fig. 4-2(d) was smoothed down only to a limited extent as compared to Fig. 4-2(a). The XRD result of this forced convection experiment is shown in Fig. 4-3. Its (200) peak intensity, as shown in Fig. 4-4, was also found to be lower than that of the parallel magnetic field.

Therefore, it can be inferred from these investigation results that the magnetic fields may have played a role beyond the MHD stirring to the bulk electrolyte and the increase of electrode

potential. In fact, the change in the deposit's morphology and texture caused by the MHD effect through increasing convection in the bulk electrolyte and elevating cathode potential has proved to be limited.

### **4.3.2 The mechanisms on the morphological change during deposition in magnetic fields**

#### **4.3.2.1 Mechanisms of electro-deposition under the influence of the parallel magnetic field**

Based on the above characterization and the new insights into the MHD effect, a new mechanism is proposed to rationalize the surface modification occurring during electroplating under a parallel magnetic field. As illustrated in Fig. 4-7, a semi-spherical grain is assumed to be formed on the deposit surface. According to the fluid mechanics<sup>29</sup>, flow around a body generally develops a thin layer along the body surface. This layer is called the hydrodynamic boundary layer. The thickness of the layer was estimated to be about 10 times of the diffusion layer<sup>5,30</sup>. Nickel ions migrating to the cathode enter this boundary layer (the term “boundary layer” in the following sections refers to the hydrodynamic boundary layer) before being reduced and incorporated into the coating film matrix.

For any points on the surface of the semi-sphere, the migrating velocity of the nickel ions in the boundary layer,  $V$ , can be resolved into two components, as shown in Fig. 4-7(a),  $V_1$  and  $V_2$ , which are laid in the planes parallel and perpendicular to the magnetic field, respectively. The perpendicular component  $V_2$  is always subjected to the Lorentz force to the maximum extent equally at any points on the surface, showing no position-related difference to the field, and is inclined to keep the original shape of the grain unchanged while growing in deposition. However,

the component  $V_1$  on the plane parallel to the magnetic field, as shown in Fig. 4-7(b), is affected differently by the magnetic field, depending on its position on the semi-sphere. The component  $V_1$  is almost not affected by the magnetic field in the top region of the semi-sphere (e.g. Point a), as  $V_1$  is nearly parallel to the magnetic field, while an increased impact of the magnetic field on  $V_1$  is expected from Point a to Point b because of the increased intercept angle between  $V_1$  and

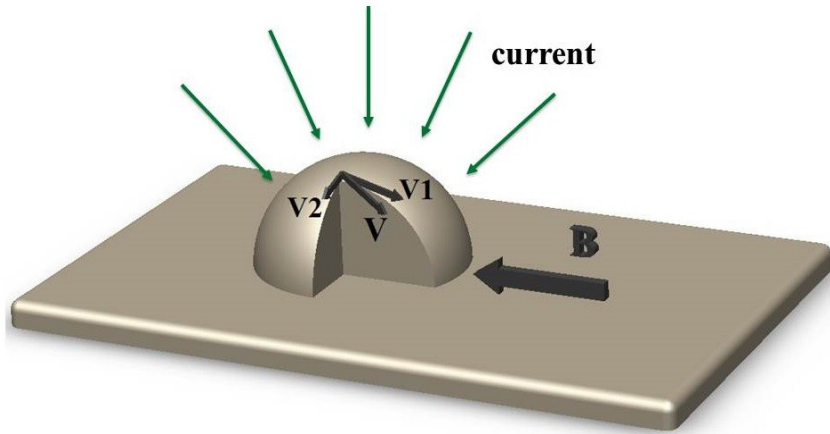


Fig. 4-7 (a)

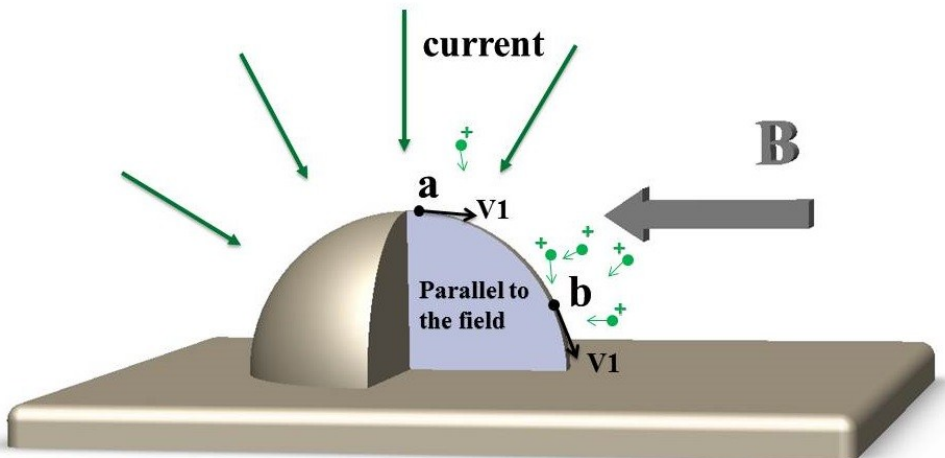


Fig. 4-7(b)

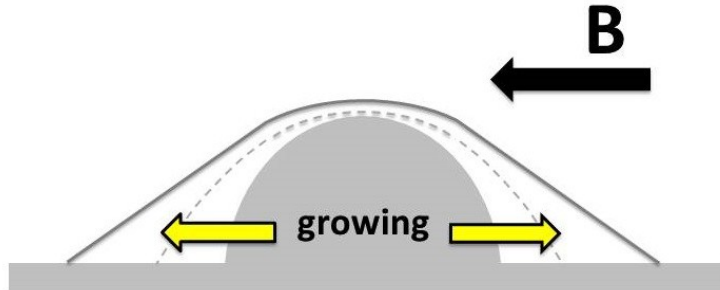


Fig. 4-7(c)

Figure 4-7 Schematics representing the mechanism of the parallel magnetic field affecting the deposit morphology.

the field. As a result, a higher nickel-ion concentration surrounding the side surface, as compared with that in the top region of the grain, can be expected because of the enhanced ion migration from the MHD stirring.

From the above discussion, it is obvious that the semi-sphere will grow preferentially on the side surface where the nickel ions' migration is increased, whereas the growth in the top region of the sphere is suppressed, as schematically illustrated in Fig. 4-7(c).

The model can be applied to predict and control the coating morphology once the local flow pattern on the cathode surface can be designed specifically. As depicted in Fig. 4-8, if the fluid flow is controlled perpendicular to the magnetic field (Fig. 4-8(a)), the  $V_2$  component dominates, and the semi-spherical grain will continue to maintain its shape and grow at a higher speed. This will lead to a film with a rougher surface than that occurring in the absence of the magnetic field owing to the MHD convection. If the streamlines are mainly in the planes parallel to the

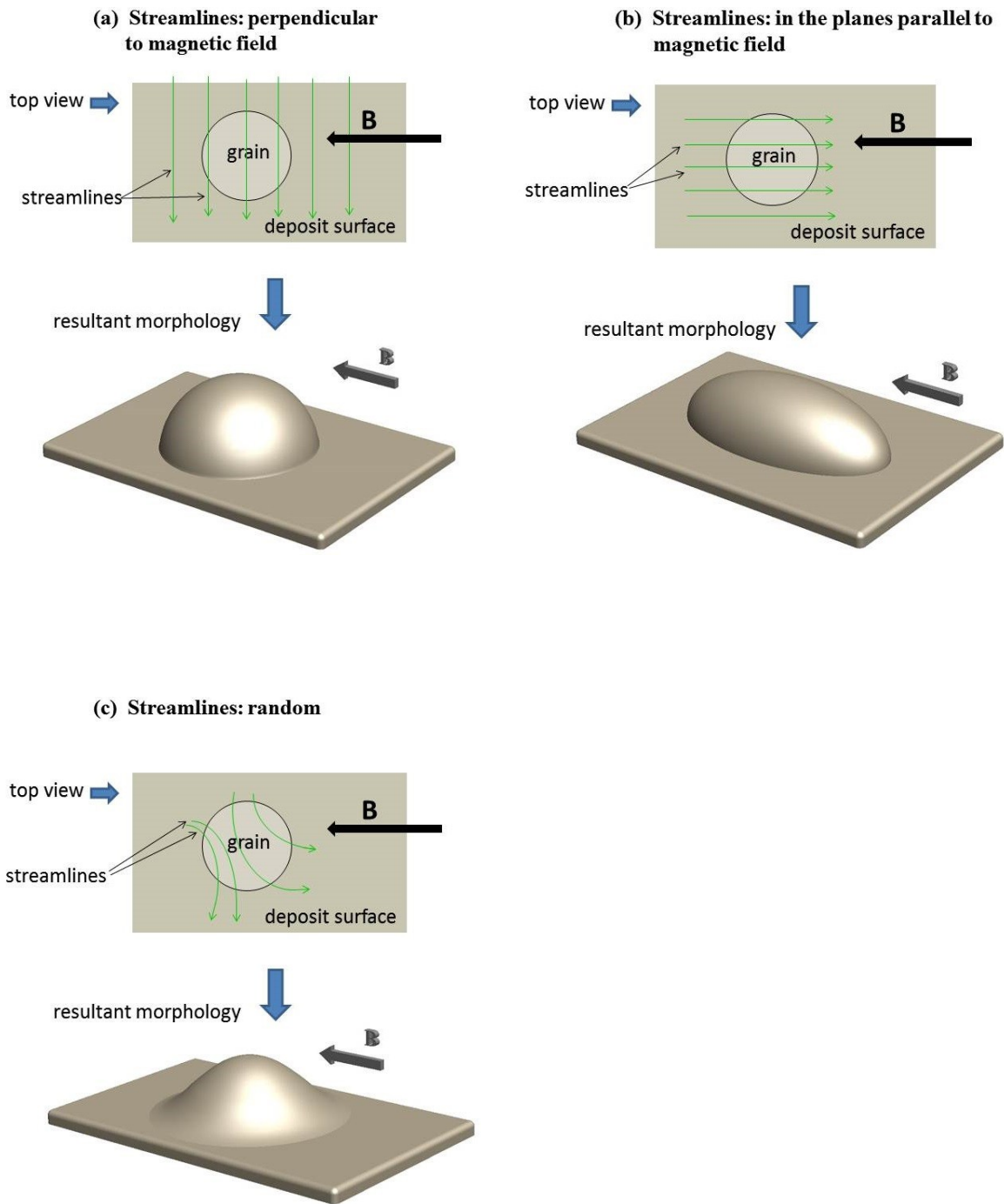


Figure 4-8 Illustration of the morphological variations of the deposit in parallel magnetic field under different flow patterns.

magnetic field (Fig. 4-8(b)), according to the discussion in Fig. 4-7(b) and (c), the V1 component dominates, elongated grains will be formed and aligned with the direction of the magnetic field. If random streamlines are applied (Fig. 4-8(c)), both V1 and V2 components will be in effect and the semi-spherical grain will deform into a dune.

The above model can be used to explain the formation of a rougher surface when Cu was deposited under parallel magnetic field, as compared with the absence of the magnetic field<sup>31</sup>. Although no explanation was given, the difference in surface roughness reported in Ref. 31 could be attributed to the interaction of the MHD effect and the fluid flow as shown in Fig. 4-8 (a).

The model proposed above is also remarkably consistent with the observations of the elongated grain features found during the deposition of iron and its alloys<sup>17-19</sup>. It is well established that those soft magnetic materials such as Fe or Fe alloys have higher permeabilities than other materials<sup>32</sup> and can generate significant magnetization and an additional magnetic field on the coating surface which is aligned in the direction of the superimposed magnetic field. The critical feature of the additional magnetic field from magnetization is that it is not uniform and has a field gradient around a grain. When discharged ferromagnetic adatoms diffuse on the coating surface, the field gradient imposes a force to them which is given as<sup>33</sup>

$$f_m = m\nabla B \quad (4-1)$$

Where  $m$  is the magnetic moment of individual adatom,  $B$  is the total magnetic field flux density and  $f_m$  is the force applied by the field gradient on an adatom.

To estimate the order of magnitude of this force on the adatoms, the adatom density in solution has to be evaluated, which requires the knowledge of the adatom lifetime on the surface.

A great number of studies have focused on the adatom diffusion on the metal surface<sup>34-40</sup>. The results show that there are three mechanisms responsible for the adatom surface diffusion: hopping, atom exchange and step-edge atom exchange. Among these mechanisms the hopping is found to be dominant<sup>39</sup>. The residence time of an adatom between hops has been determined to be on the order of microseconds<sup>40</sup>. Therefore, the average adatoms lifetime can be rationally assumed to be 1 microsecond. Consequently, the adatom density is calculated as:

$$\rho_a = \frac{jN\tau}{nFd_a} \quad (4-2)$$

$\rho_a$  denotes the adatom density in the solution;  $j$  is the deposition current density;  $N$  is the Avogadro constant;  $\tau$  is the average adatom lifetime;  $n$  is the number of electrons involved in the electrochemical reaction;  $F$  is the Faraday constant and  $d_a$  is the dimension of the thickness of the adatom layer on the coating surface.

From Equations (4-1) and (4-2), the body force of the field gradient from surface magnetization on the adatoms can be estimated as

$$f_m \rho_a = \frac{jN\tau m \nabla B}{nFd_a} \quad (4-3)$$

Take the electrodeposition of iron as an example. The related parameters in Equation (4-3) of Fe are listed in Table 4-1.

**Table 4-1 Parameters used for calculating the body force of the field gradient on surface adatoms in Equation (4-3)**

$j$ (A/cm <sup>2</sup> )	$\tau$ (s)	$m$ (A/m)	$\nabla B$ (T/m)	$n$	$d_a$ (m)
100	$10^{-3}$	$2.2 \mu_B^*$	10	2	$10^{-9}^{**}$

\*  $\mu_B = 9.27 \times 10^{-24} \text{ JT}^{-1}$  is the Bohr magneton. The data of  $m$  is from Ref. 33.

\*\*The thickness of the adatom layer on the surface is set to be 1 nm due to the fact that the atomic radius of the Fe atom is  $0.124 \text{ nm}^{33}$ .

The calculation using Equation (4-3) and the data listed in Table 4-1 yields a body force of the field gradient from the coating magnetization on Fe adatoms of  $6 \times 10^3 \text{ N/m}^2$ , which is on the same order of magnitude of the driving force for the natural convection ( $10^3 \text{ N/m}^2$ ) estimated in Ref. 41. Moreover, because of the small size of the adatoms, they move in close vicinity of the film surface that is on the bottom of the boundary layer. The flow speed of fluid in the localized area is expected to be slower than in the bulk electrolyte, leading to more significant dominance of the force in Equation (4-3) over the driving force for the natural convection.

The calculations clearly demonstrate that the magnetization of the Fe coating film resulted in a force on the Fe adatoms diffusing on the film surface. The force was strong enough to overcome the natural convection and to direct the adatoms to move along the direction of external magnetic field. Consequently, the movement of the adatoms changes the fluid streamlines in the boundary layer to the situation described in Fig. 4-8(b), and gives rise to the formation of elongated grains.

In addition, the protruding grains of a soft magnetic material on the film surface can serve as micro magnets in the external magnetic field, producing a significant field gradient force due to strong surface magnetization. This field gradient force allows the protruding grains to attract the paramagnetic ions in the electrolyte<sup>42</sup>. Such an effect can also promote the elongating growth of the grains.

On the other hand, in the current investigation, the electrolyte flow can be considered random because nickel is not a soft magnetic material<sup>32</sup>; thus the induced magnetic field on the nickel surface cannot modulate the streamlines. Accordingly, the deposit shown in Fig. 4-2(b) is composed of multiple dunes, which confirms the prediction in Fig. 4-8(c)

#### **4.3.2.2 Mechanisms of electro-deposition under the influence of vertical magnetic field**

The mechanisms of the morphological formation under the influence of vertical magnetic field are more complex than those found in the presence of parallel magnetic field. Two different influencing mechanisms are proposed below.

First, as schematically illustrated in Fig. 4-9(a), the nickel ions in the boundary layer on a planar surface of the deposit are affected by a maximum Lorentz force and move in circles, as has been described by Aogaki in Ref. 11.

The circular motion of ions is normal to the magnetic field and causes the strongest MHD stirring, whereas those nickel ions in the boundary layer around a semi-sphere are less impacted by Lorentz force, due to the fact that the streamlines surrounding the geometrical profile of the semi-sphere are generally not perpendicular to the magnetic field. Thus, the planar surface tends to grow faster than the upheavals, like the semi-spheres. As a result, the upheavals if present

become merged through the fast upward growth of the planar surface between the upheavals. This would result in a leveled deposit surface.

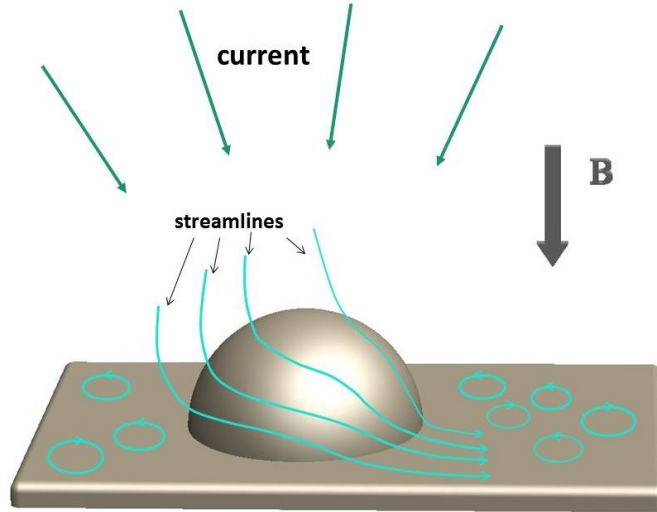


Fig. 4-9(a)

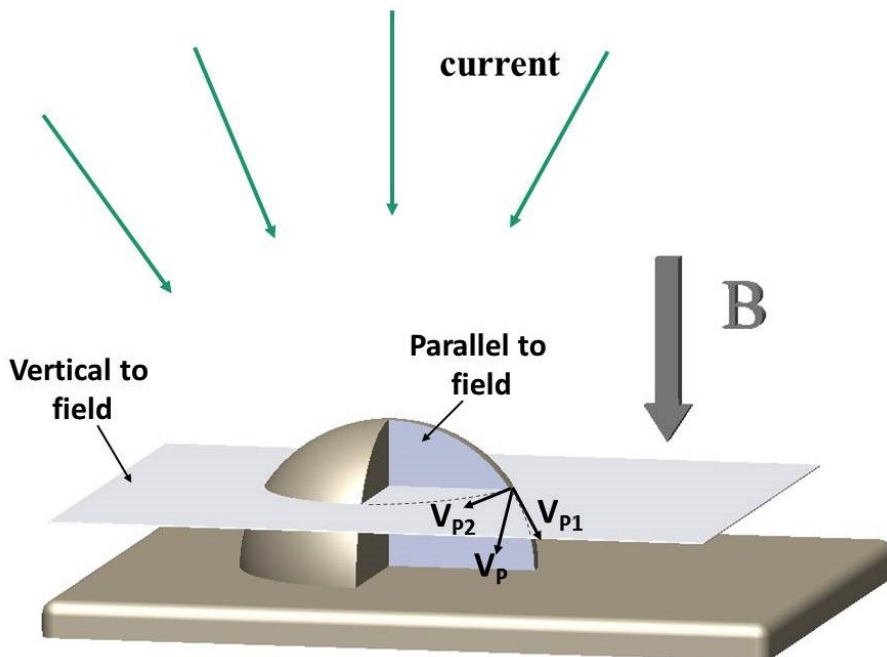


Fig. 4-9(b)

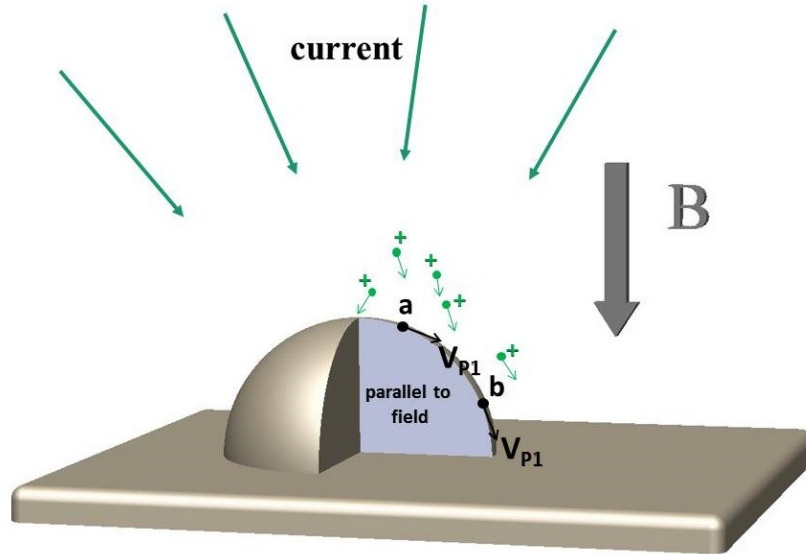


Fig. 4-9(c)

Figure 4-9 Illustration showing the two mechanisms explaining the morphology formation during plating in the vertical magnetic field.

Second, similar to the analysis in Fig. 4-7, the velocity of the ions in the boundary layer on the curved grain surface,  $V_p$ , can be resolved into a component on a plane parallel to the magnetic field,  $V_{p1}$ , and a component on a plane perpendicular to the magnetic field,  $V_{p2}$ , as described in Fig. 4-9(b).  $V_{p2}$  promotes the growth of the grain while maintaining its shape. The effect of  $V_{p1}$  is further shown in Fig. 4-9(c). At Point *a*, the Lorentz force and the MHD effect on  $V_{p1}$  can be stronger than at Point *b* because the local  $V_{p1}$  at Point *a* is more perpendicular to the field. This leads to a higher ion concentration around Point *a*, and the upper part of the grain grows faster than the lower part. Overall, the two components,  $V_{p1}$  and  $V_{p2}$ , tend to act together to increase the surface roughness.

Under the first mechanism, the leveling effect comes from the maximum MHD convection of the metal ions on the planar surface, while the upward growth of the coating under the second mechanism is caused by the different MHD effect due to varied  $V_{p1}$  component. The MHD effect on the flat surface can be stronger than that on an inclined or curved surface. The MHD effect from the two components acts together to produce a deposit with smoother surface, as shown in Fig. 4-2(c). This also explains why the deposit surface is smoother under the vertical magnetic field than under the parallel magnetic field.

However, during the deposition of soft magnetic materials, because of the strong induced magnetic field on the coating surface, the diffusing adatoms are believed to adjust the streamlines on the grain surface to align themselves in the planes parallel to the field, as discussed in the parallel field configuration, and further illustrated in Fig. 4-10(a). The  $V_{p2}$  component is negligible and only component  $V_{p1}$  is in effect. The latter will interact with the vertical field, especially in the top region of the grain where  $V_{p1}$  is nearly perpendicular to the magnetic field and growth will be faster than the side region. In addition, the field gradient effect resulting from the protruding grains also plays a role in the growth of grains along the field direction. This is similar to the case of forming elongated grains in parallel field. These two effects, which are concurrently present, can lead to the formation of a column-like structure, as illustrated in Fig. 4-10(b). Meanwhile, the protruding column that is strongly magnetized by the external magnetic field can produce an additional MHD effect and gather more ions around it, resulting in the sparse supply of the ions in the region with a planar surface and a diverse coating film. The phenomenon of column formation in Fe or its alloys<sup>5, 20</sup> is thus clearly explained.

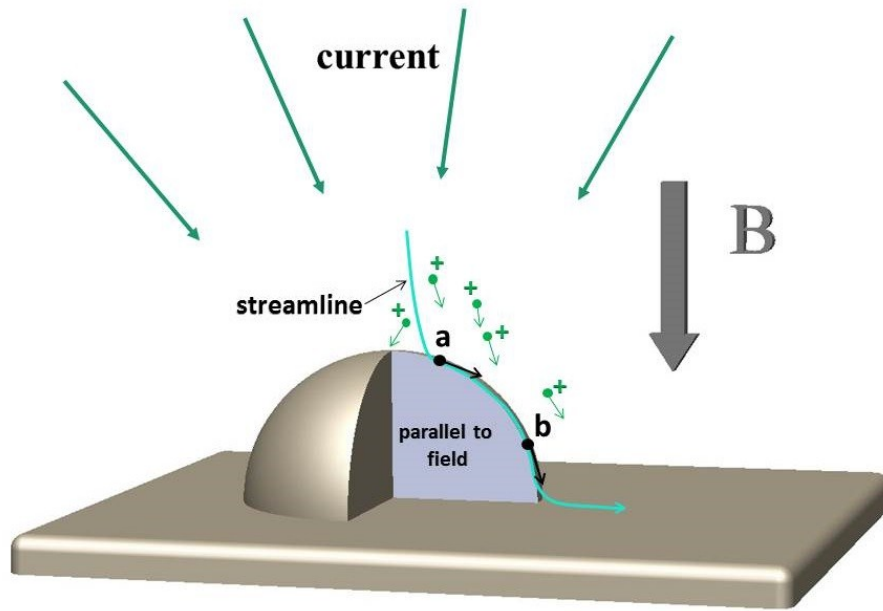


Fig. 4-10(a)

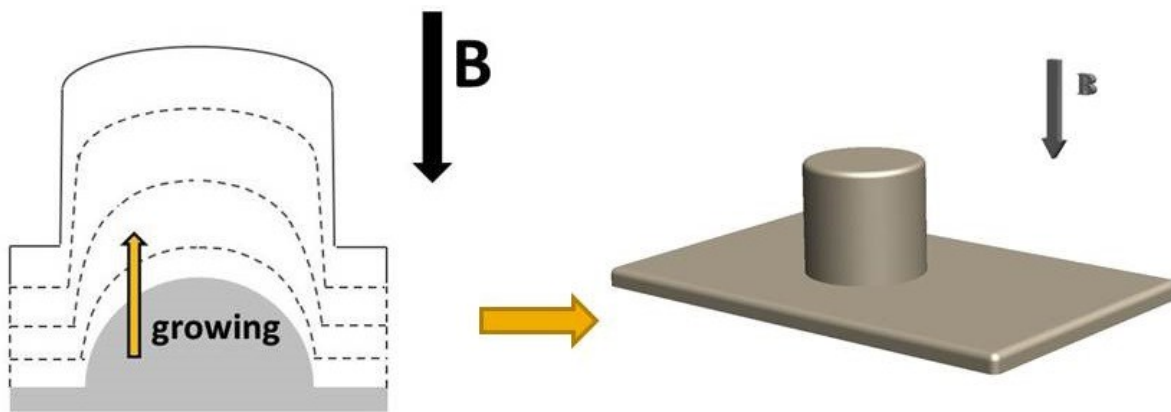


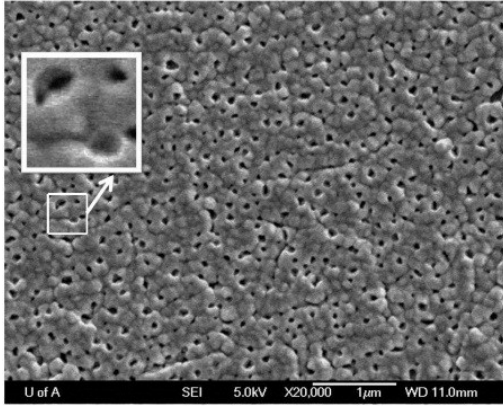
Fig. 4-10(b)

Figure 4-10 Schematic of the soft magnetic material deposited in vertical magnetic field and the resultant columnar morphology.

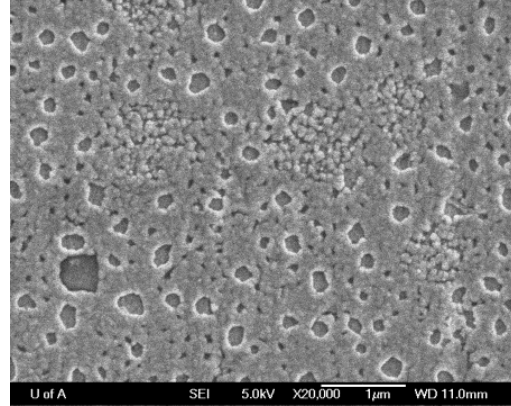
Fig. 4-11 shows the SEM images of nickel deposition for 100 seconds in both the parallel (Fig. 4-11(a)) and vertical (Fig. 4-11(b)) magnetic fields, which further verifies the models illustrated in Fig. 4-7 to Fig. 4-10. There are some holes in the two images, which are caused by either hydrogen bubbles or a heterogeneous nucleation of nickel in the early stage of deposition. In Fig. 4-11(a) the holes are small and have an appearance of erupted volcanoes or craters. The side wall of the holes is featured with an inclined slope and spherical perimeter (see the inset). In Fig. 4-11(b), however, the holes are larger and have a flat bottom. The side surface of the holes in Fig. 4-11(b) is perpendicular to the plating surface, rather than inclined as is the case under the parallel magnetic field in Fig. 4-11(a). In the latter case, the presence of the erupted volcanoes or crater-like surface features indicates the coalescence of the dunes formed through a mechanism illustrated in Fig. 4-8(c). In Fig. 4-11(b) the existence of larger holes and the flat surfaces inside and outside of the holes is consistent with the mechanism presented in Fig. 4-9(a), in which the magnetic field favors the deposition on the planar surface perpendicular to the field. All the planar surfaces are subjected to the same vertical field. The holes, originally formed due to heterogeneous nucleation, are filled in the following deposition because of the unfavorable MHD condition on their walls.

#### **4.3.3 The Mechanism on the nickel texture formation under the influence of magnetic field**

To further reveal the mechanism of texture formation during nickel deposition in the magnetic field, a morphological characterization by AFM has been adopted in this investigation. Such an approach of relating morphological and structural change through AFM observation has never been reported in the field of electroplating. Fig. 4-12 shows the AFM images of the nickel surface after deposition for 50 seconds in different magnetic field conditions. The most striking finding of this characterization is the observation of pyramidal islands together with some



(a)  $B=0.18\text{T}$ , parallel field



(b)  $B=0.18\text{T}$ , vertical field

Figure 4-11 SEM images showing nickel deposition in the parallel and vertical magnetic fields for 100 seconds.

nodular islands on the deposit surface, as seen in Fig. 4-12. The pyramidal islands have two symmetrical elongated facets, as circled in the inset of Fig. 4-12(a) and (b), and some of them are about to merge together. Because the characterization was done at the beginning of the deposition, it clearly demonstrates that the special pyramidal island is a preferred morphology of the nickel deposit nuclei. Fig.4-12 also reveals that the islands in the absence of the magnetic field are the largest in size. The islands turned smaller in the magnetic field due to its leveling effect. The smallest islands are under the vertical magnetic field, and are barely resolvable by AFM (Fig. 4-12c).

The details of nickel nucleation obtained from AFM characterization provide new insights into the texture evolution of nickel deposition under the influence of the magnetic field. First, it has been generally accepted<sup>25</sup> that the deposit film tends to expose the planes with the lowest surface energy as the final growth facet, which would be the  $\{111\}$  planes in fcc crystals. This suggests that the two symmetrical rectangular facets of the pyramidal islands in Fig. 4-12 might

be the two (111) planes. A nickel island with morphology similar to that of the pyramids that have two symmetrical elongated facets in Fig. 4-13 has also been reported. The surface planes of that island were rationalized to be Ni (111)<sup>43</sup>. Therefore, it can be reasonably affirmed that the facets of the pyramids in this research should belong to Ni {111}.

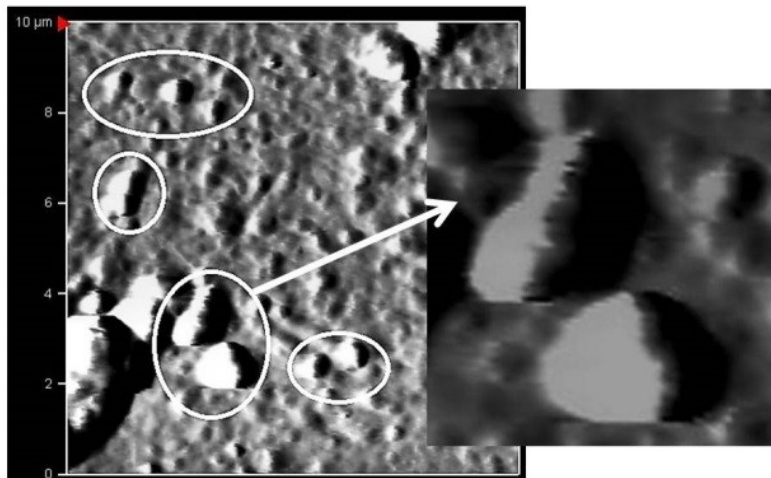


Fig. 4-12(a) B=0

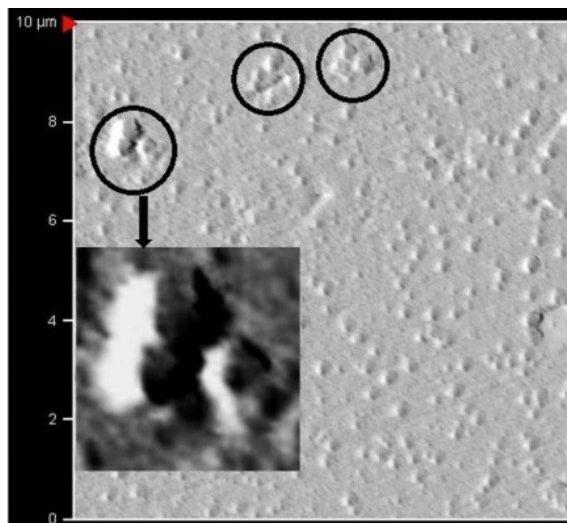


Fig. 4-12(b) B=0.18T, parallel field

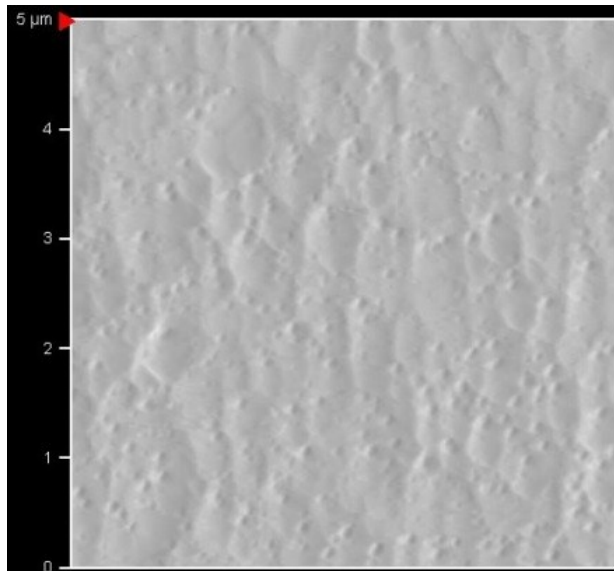


Fig. 4-12(c)  $B=0.18\text{T}$ , vertical field

Figure 4-12 AFM observation of the nickel deposit surface in various magnetic field conditions for 50 seconds.

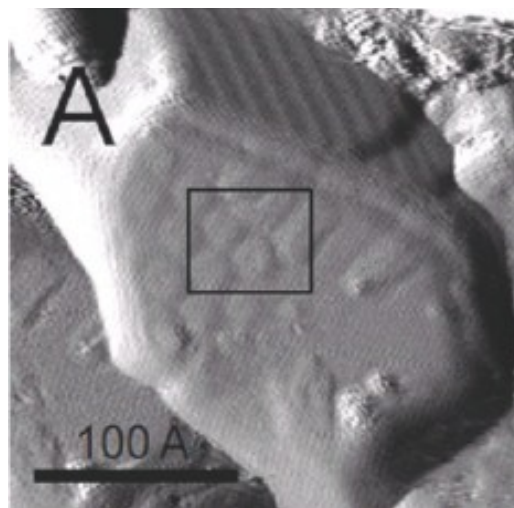


Figure 4-13 STM image of a Ni(111) island. (Fig. 2(A) in Ref.43)

During the leveling process of these nickel islands under the influence of the superimposed magnetic field, the bottom growth of these islands are accelerated. As illustrated in Fig.4-14, if the two exposed pyramid facets are the {111} planes, the bottom of the pyramids is in the direction of (200). Therefore, leveling the pyramidal islands generated in the nucleation stage promotes the growth of the pyramid bottom, producing an increased (200) texture in the coating, as observed in the coating when the magnetic fields were applied.

As has been pointed out previously, the vertical magnetic field is more effective in leveling the nickel deposit surface in this investigation, and consequently further enhances the (200) growth as compared with the parallel magnetic field, resulting in a higher (200) peak intensity in XRD pattern shown in Fig. 4-3.

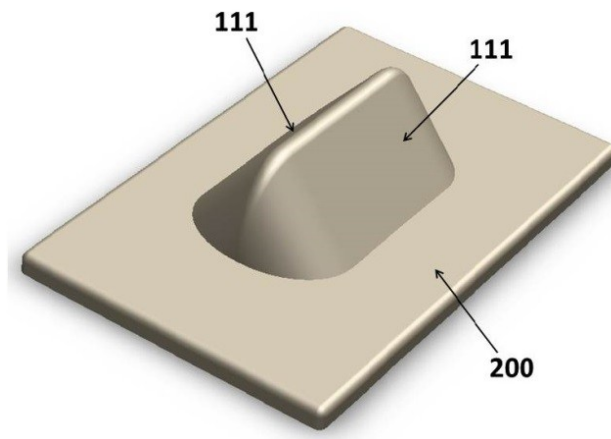


Fig. 4-14(a)

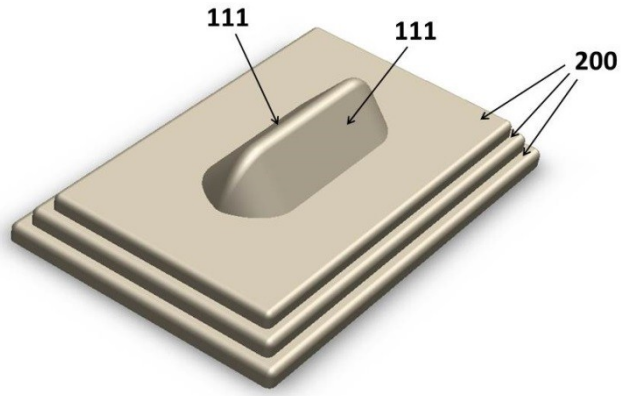


Fig. 4-14(b)

Figure 4- 14 Schematic illustration of the magnetic field changing the nickel crystal texture through levelling the pyramidal island on the deposit surface.

#### 4.4 Conclusions

The influence of the external magnetic field both parallel and perpendicular to the electrode surface on the nickel electrodeposition was investigated and three new models were proposed to provide some new theoretical perspectives of electrodeposition under the influence of magnetic fields.

The experimental findings in this investigation showed that MHD convection in the bulk electrolyte has limited effect on the surface morphologies of the deposits, contradictory to what is generally believed. Therefore, two new models were established to rationalize the role that the MHD effect played in surface morphology formation during electrodeposition.

According to the two new models being proposed, a parallel magnetic field reduces the coating roughness by promoting the lateral growth of the undulation on the deposit surface. This can produce elongated grains in soft magnetic material deposition.

The vertical magnetic field can produce both the leveling and roughening effect. The leveling effect is achieved by accelerating the growth of the flat regions to minimize the absolute height of protrusions on the electrode surface. The roughening occurs on the top of a protrusion where Lorentz force is stronger than on the side surface of the protrusion, which favors the upward growth of the protrusions and therefore increases the roughness. For materials other than the soft magnetic materials, the leveling effect is predominant, leading to the deposit with a smooth surface. For the soft magnetic materials, however, the roughening effect is strengthened, together with a significant field gradient effect that is generated by the strong surface magnetization, leading to the formation of a columnar morphology. Both these models have been found to be consistent with experimental findings obtained in this investigation and in the literature.

In addition, AFM technique was introduced to characterize the surface morphology formed during the initial stage of electrodeposition. It was found that the nickel nuclei had a pyramidal shape with two elongated facets identified to be Ni (111). Based on the characterization, a new model was established to elucidate the texture formation during the nickel film deposition. Through the leveling process the magnetic field facilitated the growth of the base planes of the pyramidal islands, which are in the direction of Ni (200). This has promoted (200) growth, as experimentally observed. Here, the leveling effect resulting from MHD convection in the fluid boundary layer played a key role in the texture formation during nickel plating.

## 4.5 References

- 1 S. Molokov, R. Moreau, H.K. Moffatt (eds.), *Magnetohydrodynamics – Historical Evolution and Trends*, 391-407. 2007 Springer.
- 2 E. Tronel-Peyroz, A. Olivier, *Physico-Chemical Hydrodynamics* (1982), 3: 251-265.
- 3 O. Aaboubi, J. P. Chopart, J. Douglade, A. Olivier, C. Gabrielli and B. Tribollet, *J. Electrochem. Soc.*, Vol. 137, 6(1990) 1796-1804.
- 4 V. Ganesh, D. Vijayaraghavan, V. Lakshminarayanan, *Applied Surface Science* 240 (2005) 286-295.
- 5 G. Hinds, F. E. Spada, J. M. D. Coey, T. R. Ni Mhiochain, and M. E. G. Lyons, *J. Phys. Chem. B* 2001, 105, 9487-9502.
- 6 A. Bund, S. Koehler, H. H. Kuehnlein, W. Plieth, *Electrochim. Acta* 49 (2003) 147.
- 7 O. Devos, A. Olivier, J. P. Chopart, O. Aaboubi, G. Maurin, *J. Electrochem. Soc.*, Vol. 145 (2) 1998, 401.
- 8 O. Devos, O. Aaboubi, J. P. Chopart, E. Merienne, A. Olivier, J. Amblard, *J. Electrochem. Soc.*, Vol. 145 (12) 1998, 4135.
- 9 I. Tabakovic, S. Riemer, V. Vas'ko, V. Sapozhnikov, M. Kief, *J. Electrochem. Soc.*, Vol. 150 (9) 2003, C635-640.

- 10 A. Krause, C. Hamann, M. Uhlemann, A. Gebert, L. Schultz, *Journal of Magnetism and Magnetic Materials* 290–291 (2005) 261–264.
- 11 R. Aogaki, *Magnetohydrodynamics* 37, 143–150 (2001).
- 12 R. Aogaki, *Magnetohydrodynamics* 39, 453–460 (2003).
- 13 A. Sugiyama, M. Hashirideb, R. Morimotob, Y. Nagaib, R. Aogakic, *Electrochimica Acta* 49 (2004) 5115–5124.
- 14 H. Matsushima, A. Ispas, A. Bund, B. Bozzini, *Journal of Electroanalytical Chemistry* 615 (2008) 191–196.
- 15 J. Koza, M. Uhlemann, A. Gebert, L. Schultz, *J. Solid State Electrochem* (2008) 12:181–192.
- 16 S. Bodea, L. Vignon, R. Ballou, P. Molho, *Phys. Rev. Lett.* 83 (1999) 2612.
- 17 A. Ispas, H. Matsushima, W. Plieth, A. Bund, *Electrochim. Acta* 52 (2007) 2785.
- 18 H. Matsushima, T. Nohira, and Y. Ito, *Electrochemical and Solid-State Letters*, 7 (8) C81-C83 (2004).
- 19 H. Matsushima, Y. Fukunaka, Y. Ito, A. Bund, W. Plieth, *Journal of Electroanalytical Chemistry* 587 (2006) 93–98.
- 20 J. A. Koza, F. Karnbach, M. Uhlemann, J. McCord, C. Mickel, A. Gebert, S. Baunack, L. Schultz, *Electrochimica Acta* 55 (2010) 819–831.

- 21 A. Chiba, K. Kitamura, T. Ogawa, Surf. Coat. Technol., 27, 83 (1986).
- 22 D. Y. Li, J. A. Szpunar, J. Matt. Sci. 28 (1993) 5554-5559.
- 23 D. Y. Li, J. A. Szpunar, Electrochim. Acta 42 (1997) 37-45.
- 24 D. Y. Li, J. A. Szpunar, Electrochim. Acta 42 (1997) 47-60.
- 25 T. Watanabe, Nano Plating - Microstructure Formation Theory of Plated Films and a Database of Plated Films, Elsevier, 1st Edition, 2004.
- 26 Rashkov, S., Stoichev, D. S., Tomov, L 1972. Electrochim. Acta 17: 1955.
- 27 E. Brillas, J. Rambla, J. Casado, J. Appl. Electrochem. 29 (1999) 1367.
- 28 C. Cierpka, T. Weier, G. Gerbeth, M. Uhlemann, K. Eckert, J Solid State Electrochem (2007) 11:687–701.
- 29 Y. Nakayama, R. Bouche, Introduction to Fluid Mechanics, Butterworth-Heinemann, 2002.
- 30 Levich, V. G. Physicochemical Hydrodynamics; Prentice-Hall, Englewood Cliffs, NJ, 1962.
- 31 G. Hinds, F. E. Spada, J. M. D. Coey, T. R. Ni Mhiochain, and M. E. G. Lyons, J. Phys. Chem. B 2001, 105, 9487-9502.
- 32 D. Jiles, Introduction to magnetism and magnetic materials, 2nd Edition, 1998.
- 33 Magnetism and Magnetic Materials, J. M. D. Coey, Cambridge University Press 2009.
- 34 J. Krug, P. Politi, T. Michely, Physical Review B, 61, No. 20 14037 (2000).

- 35 J. Tersoff, A. W. Denier van der Gon, and R. M. Tromp, PHYSICAL REVIEW LETTERS 72, No. 2, 266 (1994).
- 36 D. Edström, D.G. Sangiovanni, L. Hultman, V. Chirita, I. Petrov, J.E. Greene, Thin Solid Films 558 (2014) 37–46.
- 37 J. VIGNERON, A. BENAÏSSA,\* I. DERYCKE, A. WIAME, R. SPORKEN, International Journal of Quantum Chemistry, Vol. 70, 1093-1097 1998.
- 38 K. Kyuno and G. Ehrlich, Physical Review B, 81, No. 25 5592 (1998).
- 39 T. Treeratanaphitak, M. D. Pritzker, N. M. Abukhdeir, Electrochimica Acta 121 (2014) 407–414.
- 40 D. D Vvedensky, J. Phys.: Condens. Matter 16 (2004) R1537–R1576.
- 41 G. Hinds, J. M. D. Coey, M. E. G. Lyons, Electrochemistry Communications 3(2001) 215-218.
- 42 K. Tschulik \*, J. A. Koza, M. Uhlemann, A. Gebert, L. Schultz, Electrochemistry Communications 11 (2009) 2241–2244
- 43 Y. Murata, V. Petrova, B. B. Kappes, A. Ebnoussir, I. Petrov, Y Xie, C. V. Ciobanu, and S. Kodambaka, ACS Nano, VOL. 4. No. 11, 6509-6514, 2010.

## **Chapter 5 Effects of rotating magnetic fields on nickel electro-deposition**

## 5.1. Introduction

Numerous studies concerning the electro-deposition of metal or alloy in the presence of the superimposed magnetic field have been published in the past years<sup>1</sup>. The role that the magnetic field played in modifying electrolyte properties as well as in affecting electrolytic mass transport has been reported<sup>2,3</sup>. Although the influence of the magnetic field on the structure and morphology of the deposits has been determined<sup>4</sup>, its effect on electrode kinetics is still subject to controversy and conclusions on the basis of convincing evidences have yet to be established<sup>1, 5</sup>.

As was introduced in Section 4.1, the mechanisms that govern the electrolytic mass transport in the presence of magnetic fields are believed to be related to the convection flow in the vicinity of the electrode produced by Lorentz force. This enhanced convection flow increases the diffusion limiting current of the ions at the electrode, and is referred to as the magneto-hydrodynamic (MHD) effect<sup>6</sup>.

Up to now, much work has been done in an effort to understand the magnetic field effects during electrodeposition. Many explanations have been put forward. For morphological alterations, these explanation include the enhanced deposition rate<sup>7</sup>, the elevated adsorption of additives and inhibitors<sup>8-10</sup>, the removal of hydrogen bubbles<sup>11</sup>, the micro-MHD effect<sup>12</sup>, the fine-grained magnetic domains<sup>4</sup> and the induced magnetic dipolar<sup>13</sup>. For structural modification, the suggested views are the easy magnetization axis<sup>14</sup>, the effect of definite inhibiting species which produced Ni(OH)<sub>2</sub> and facilitated specific modes of growth<sup>8, 9</sup>, and the minimization of the system's free energy including surface energy and magnetic free energy<sup>15-17</sup>.

All these investigations mentioned above are involved in the application of the static magnetic field. So far, little emphasis has been focused on the employment of alternative magnetic field in electro-deposition. Sugiyama A. *et al.*<sup>18</sup> applied an alternative magnetic field to an electrolysis system under diffusion control. The current was measured while the frequency of the magnetic field was swept linearly. A hysteresis effect of the magnetic field and the periodic current response were observed. Devos *et al.*<sup>9</sup> perturbed a static magnetic field superimposed to an electro-deposition process by a small sinusoidal amplitude at a certain potential and measured the MHD transfer function,  $(\Delta I/\Delta B)_E$ , to study the hydrogen evolution mechanism in a Watts bath with and without the organic additive 2-butyne-1,4-diol (BD).

The crucial difference between the alternative magnetic field and the static one in terms of their effects on electro-deposition is the induced electric field, according to the Maxwell equations. The variation of the magnetic field may produce some specific influences on the charged ions in the electrolysis system.

In this chapter, the effects of the alternative magnetic field on nickel electro-deposition were examined. Special attention was paid to the understanding of the relationship between the superimposed alternative magnetic field, and the properties of the nickel deposit, such as the surface morphology and the preferred orientation, and to the development of a new engineering approach of producing high quality nickel deposition with a smooth surface. The investigation was carried out by generating an alternative magnetic field using a pair of spinning permanent magnets. This setup enables the direction of the field to change periodically while keep the magnitude constant. The characterization of the deposited nickel

was conducted by electrochemical tests, scanning electron microscope (SEM), atomic force microscope (AFM), and X-ray diffraction (XRD) techniques.

## **5.2. Experimental**

### **5.2.1. Electrolysis system**

Nickel was electrodeposited galvanostatically with a 3-electrode system. A 4×8 mm nickel foil was employed as the counter electrode. The reference electrode was a standard calomel electrode (SCE). The working electrode (electroplating substrate) was a 3×3×0.7 mm square copper sheet. The substrate was ground using 1200-grit SiC sandpaper and polished on a polishing cloth sprayed with the slurry of 0.05 μm Al<sub>2</sub>O<sub>3</sub> powder. The substrate was further pre-treated through degreasing and activation processes before plating.

In the electroplating experiments, the bath temperature was maintained at 22±2°C, and no agitation was provided. The electrolyte solution was composed of 0.05M NiSO<sub>4</sub>·6H<sub>2</sub>O, 0.1M boric acid and 0.1M sodium sulfate anhydrate acting as the supporting electrolyte. The solution pH was maintained at 4.00 during the electro-deposition tests. All chemicals were analytical reagent-grade. Deionized water was used to prepare the electroplating solutions.

### **5.2.2. Electro-deposition in the presence of an external magnetic field**

The experiment set up is shown in Fig. 5-1. A specially designed nylon cup was used in the experiment. The sample was placed in the middle of a hole in the nylon cup. A pair of permanent magnet sets was mounted onto an austenitic stainless steel frame, which was installed around the sample and the hole in the nylon cup. The diameter of the hole was 6 mm and the distance between the pair of magnet sets was 15 mm. Each magnet set consisted of four cylindrical magnets which were magnetized parallel to their axes. With such an

arrangement, the magnetic field inside the hole where the sample was placed was measured to be 0.18T

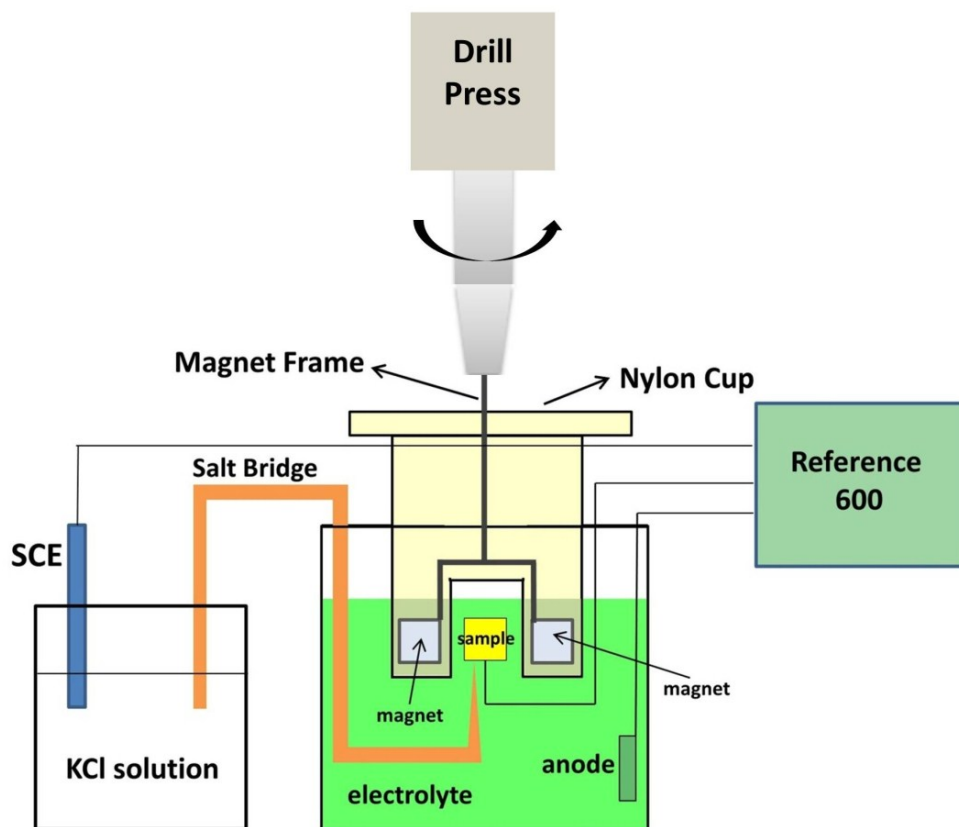


Figure 5-1 Schematic diagram of the electrolysis system in the alternating magnetic field generated from spinning magnets.

To generate an alternative magnetic field, a drill press was used to drive the austenitic stainless steel frame and the magnets to spin around the sample at speeds of 1000, 1500, 2000, 2500 and 3000 rpm. All electro-deposition experiments were performed at the current density of  $6.7 \text{ mA/cm}^2$  for 40 minutes.

### 5.2.3. Characterization of the nickel deposition

Surface characterization was conducted using a JEOL (JSM-6301FXV) field emission scanning electron microscope (SEM) with the measurement parameters denoted in the respective diagrams. The atomic force microscope (AFM) (MFP-3D, Asylum Research) was employed to measure the roughness and to reveal some detailed features of the coating surfaces. X-ray diffraction measurements were carried out in a Rigaku-UltimaIV X-ray diffractometer (XRD) using Cu K $\alpha$  radiation with a wavelength of 1.54Å. The 2 $\theta$  value was from 10° to 110°.

The electrochemical characterization of the electro-deposition process was done with a Gamry Reference 600 electrochemical work station. The chronopotentiometry curves of the nickel deposition were recorded for different magnetic field situations.

## 5.3 Results and discussion

### 5.3.1 Magnetic and electric fields in spinning magnets

The magnets spinning around the sample not only exert a magnetic field, which varies periodically, but also induce an eddy electric field into the electrolysis system.

According to Maxwell equation<sup>19</sup>,

$$\nabla \times \vec{E} = -\frac{\partial \vec{B}}{\partial t} \quad (5-1)$$

Where  $\vec{E}$  denotes the intensity of the induced electric field which is generated by alternative magnetic field, and is illustrated in Fig. 5-2.

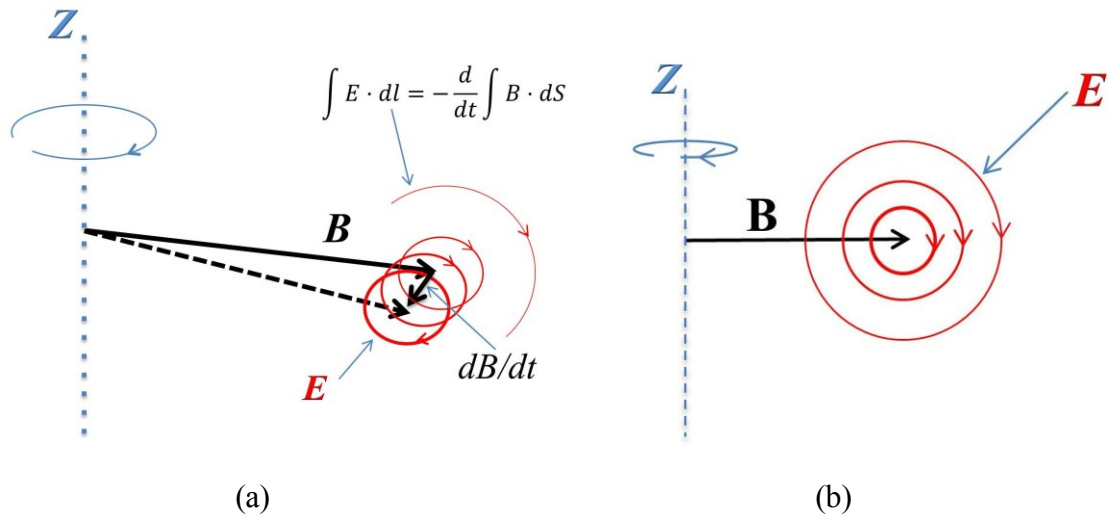
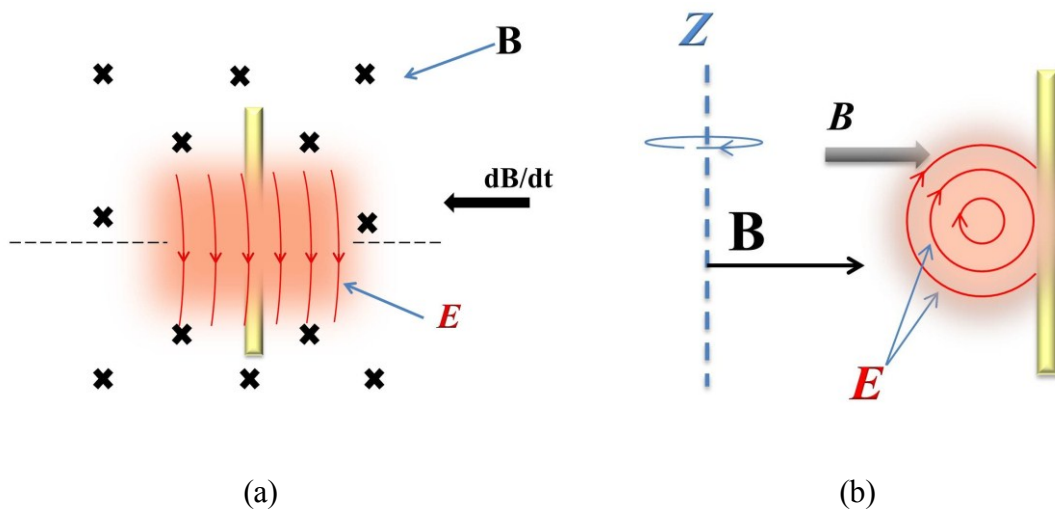
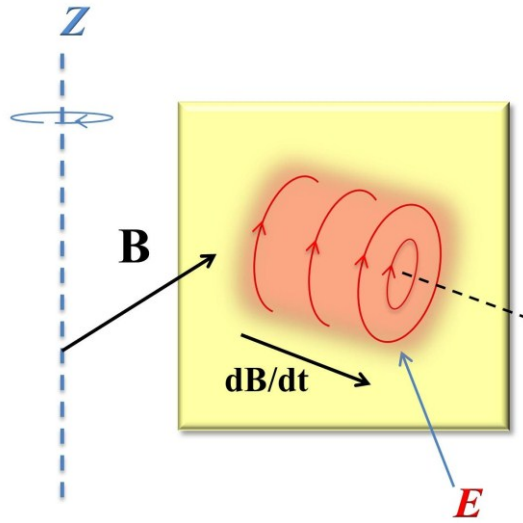


Figure 5-2 Schematic of the changing magnetic field and the induced eddy electric field produced by the spinning magnets. (a) the overall view; (b) the side view.

As depicted in Fig. 5-2, the induced eddy electric field rotates periodically along with the magnetic field. Accordingly, the eddy electric field around the sample varies periodically with the spinning magnets, as shown in Fig. 5-3.





(c)

Figure 5-3 The spinning magnetic field and the induced eddy electric field around the sample.  $B$  is (a) parallel to; (b) perpendicular to; (c) oblique crossing the sample surface.

When the magnetic field,  $B$ , is parallel to the sample surface (Fig. 5-3(a)), the axis of the eddy electric field  $E$ , is perpendicular to the sample surface; when  $B$  is perpendicular to the sample surface, (Fig. 5-3(b)), the axis of  $E$  is parallel to the sample surface; in between the above two states, the axis of  $E$  is inclined to the surface with an intersection angle between  $0^\circ$  and  $90^\circ$  (Fig. 5-3(c)).

Suppose that the component of the eddy electric field along the sample surface is  $E_s$ , Fig. 5-4 describes the response of  $E_s$  to the magnets' spin around the sample. As the magnetic field  $B$  is parallel to the sample surface (Fig. 5-4(a)),  $E_s$  is a series of concentric rings; when  $B$  is perpendicular to the sample surface (Fig. 5-4(c)),  $E_s$  uniformly spreads on the sample surface and is parallel to the direction of the spinning axis; while in the intermediate state between Fig. 5-4(a) and Fig. 5-4(c),  $E_s$  is aligned along the directions of a series of concentric ellipses or oval-shaped lines (Fig. 5-4(b)).

### 5.3.2 Electrochemical characterization

Some detailed features of the electrode behavior are demonstrated in Fig. 5-5 with the chronopotentiometry curves during deposition under spinning magnets. For magnets' spinning rate  $f=1000, 2000$  and  $2500$  rpm, the chronopotentiometry curve shifted to more positive potentials as the spinning rate increased. This can be attributed to the additional convection produced by the induced electric field, because from Equation (5-1), a higher magnets' spinning rate results in a stronger electric field. However, for  $f=1500$  and  $3000$  rpm, the chronopotentiometry curve shifted to more negative potential levels than the other three curves. These are two unusual results which later also occurred in other characterization experiments.

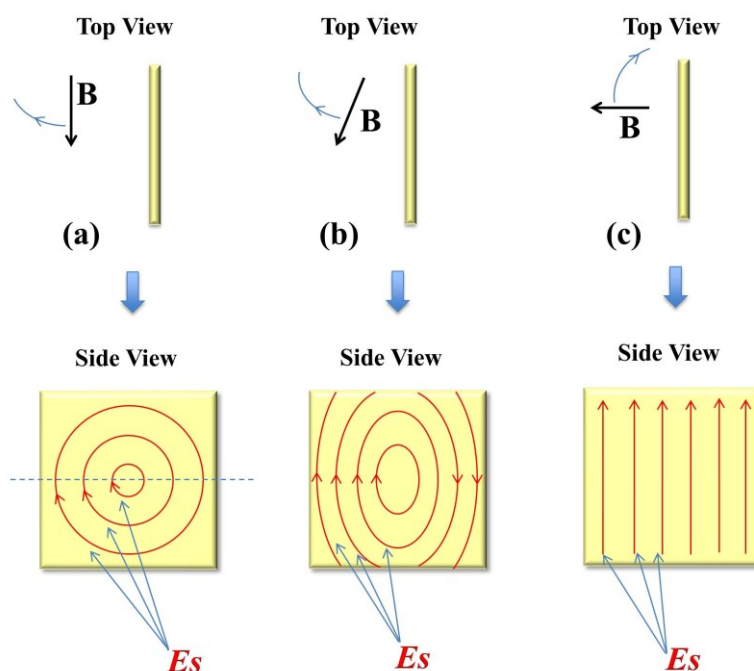


Figure 5-4 Schematic presentation of the changing process of the surface component,  $E_s$ , of the induced electric field : (a)  $B$  is parallel to the electrode; (b)  $B$  is oblique over the electrode; and (c)  $B$  is perpendicular to the electrode.

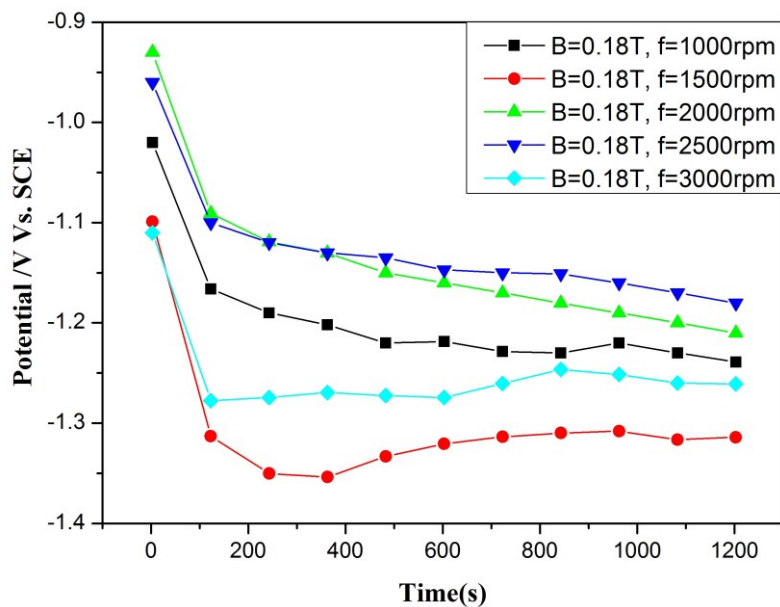


Figure 5-5 Chronopotentiometry curves during Ni deposition under different magnetic field conditions.

### 5.3.3 Morphological examination by SEM and AFM

Fig. 5-6 features the SEM image of the nickel coatings developed in various magnetic field conditions. For comparison, the images of the coating obtained in the absence and presence of static magnetic field which have been shown in Chapter 4 are also presented as Fig. 5-6 (a), (b) and (c).

At  $f=1000$  rpm, 2000 rpm and 2500rpm, the coating surface turned smoother when spinning rate became higher, as shown in Figs. 5-6(d), (f) and (g), respectively. The sample fabricated at  $f=2500$ rpm was the smoothest and had a shiny finish. At  $f=1500$ rpm, the rough spherical morphology appeared, which resembles that when the magnetic field was absent (Fig. 5-6(a)), as shown in Fig. 5-6(e). In addition, when the magnets' spinning rate increased from 2500rpm to 3000rpm, the coating surface became rougher, as seen in Fig. 5-6(h).

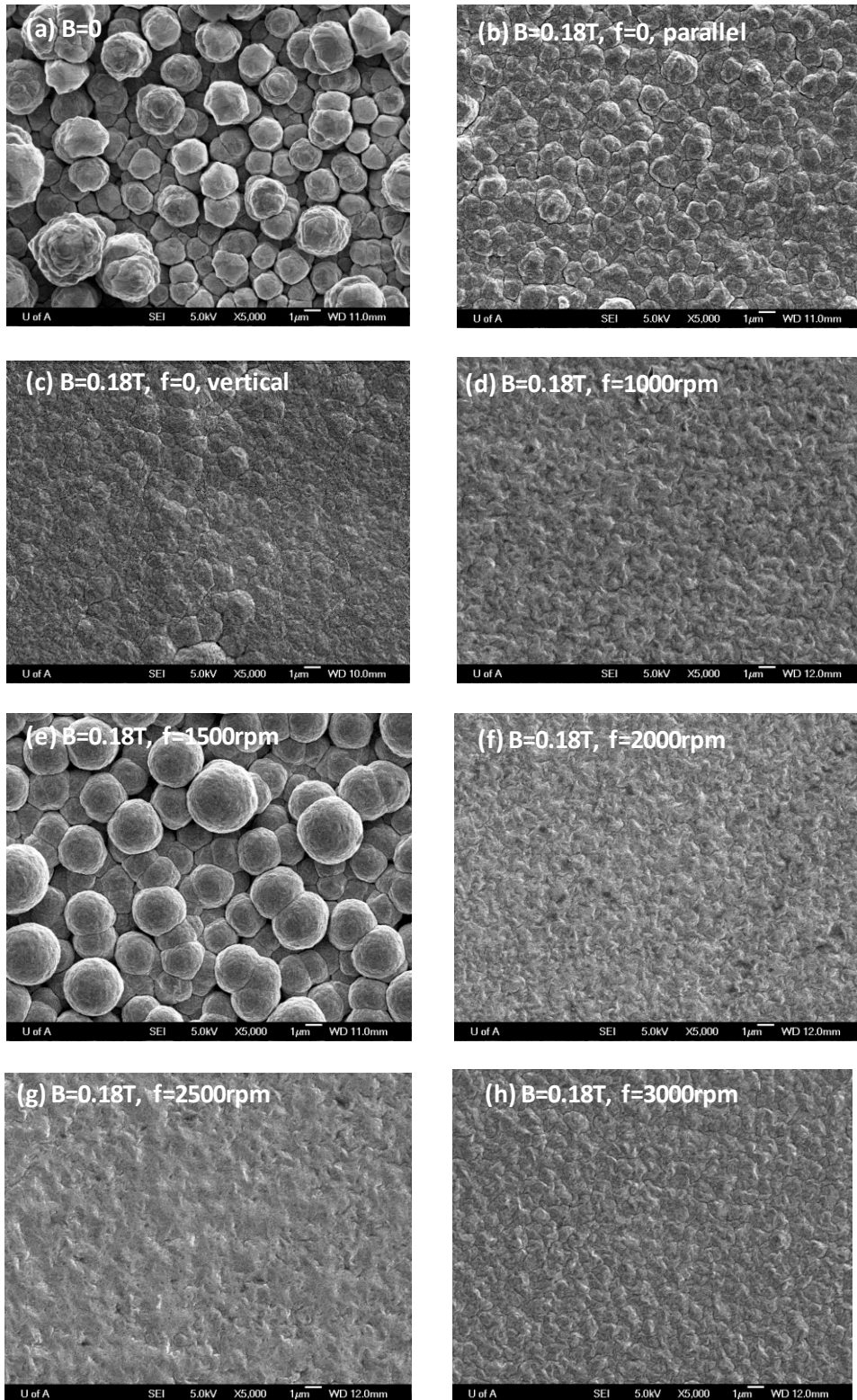


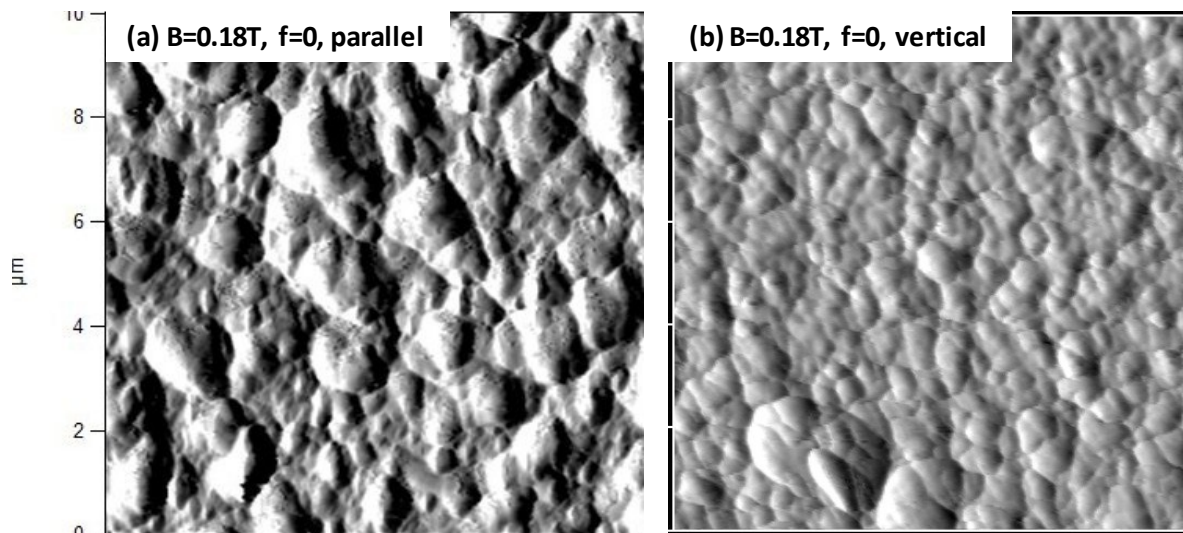
Figure 5-6 SEM images of deposited nickel morphology in the nickel sulphate bath under various magnetic field conditions: absence, static field and spinning magnet at different rates.

The surface roughness was quantitatively determined using AFM. The results obtained are listed in Table 5-1. The morphologies of the coatings were also examined at ambient conditions using AFM under the contact mode, as shown in Fig. 5-7, for the deposits at the following conditions:  $B=0.18T$ ,  $f=0$  (for both parallel and vertical field), 1000 rpm, 2000rpm, 2500 rpm, and 3000 rpm (no clear image was obtained for  $B=0$  and  $B=0.18T$ ,  $f=1500$ rpm, due to the coarse surface).

**Table 5-1 Surface Roughness Test Result with AFM\***

experiment conditions	B=0	B=0.18T, parallel	B=0.18T, vertical	B=0.18T, f=1000rpm
surface roughness RMS (nm)	222.4	74.9	26.8	32.9
experiment conditions	B=0.18T, f=1500rpm	B=0.18T, f=2000rpm	B=0.18T, f=2500rpm	B=0.18T, f=3000rpm
surface roughness RMS (nm)	222.6	27.7	21.3	43.8

\* Each value of RMS in the table is the average of three tests randomly chosen on the sample surface except for  $B=0$  and  $B=0.18T$ ,  $f=1500$  rpm, which have two measurements to average due to the coarse geometric conditions, which broke the cantilever tip several times.



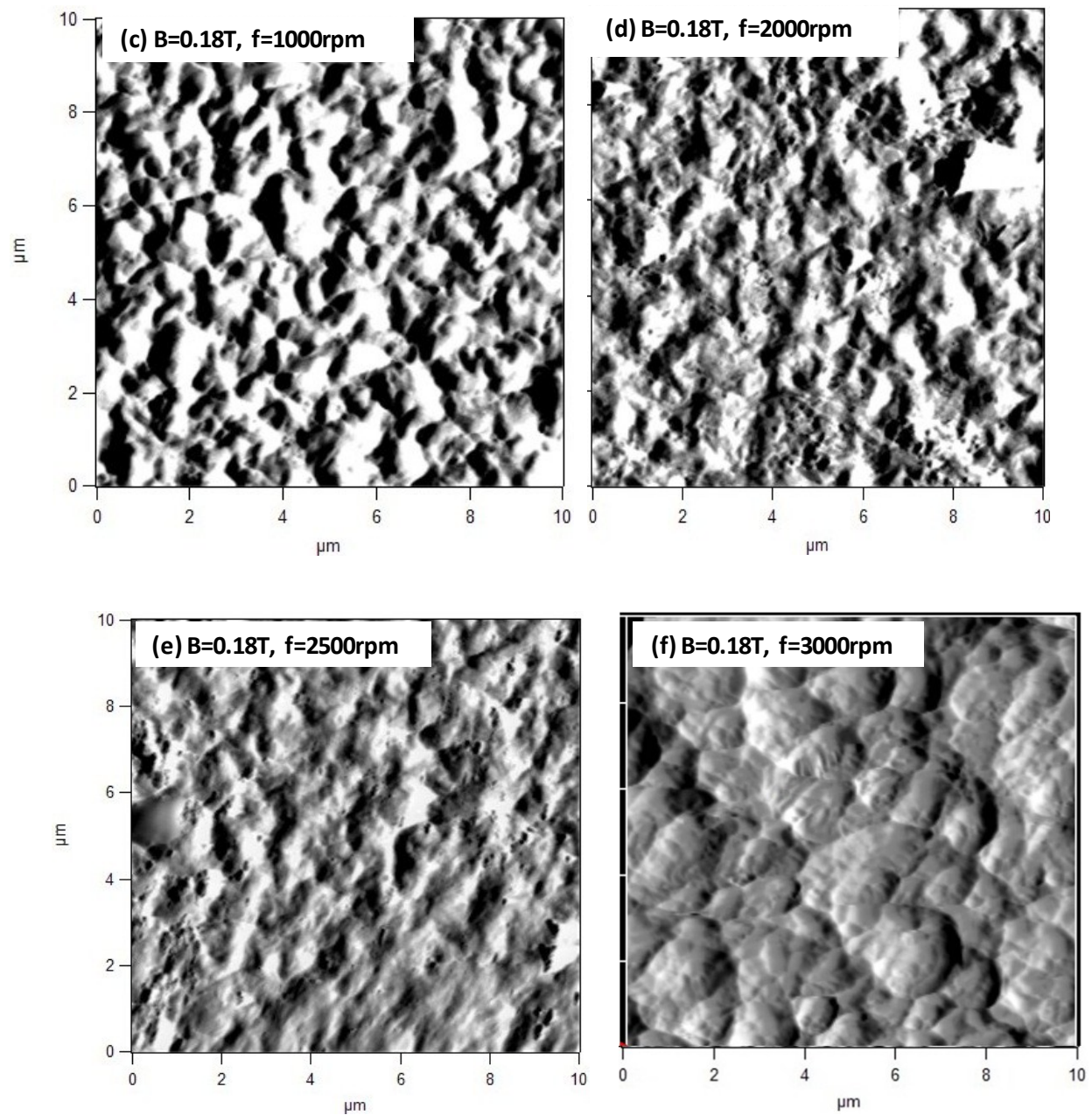
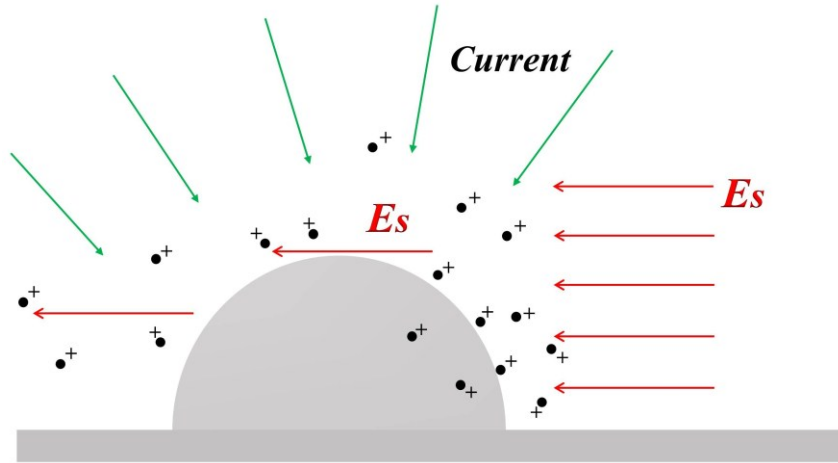
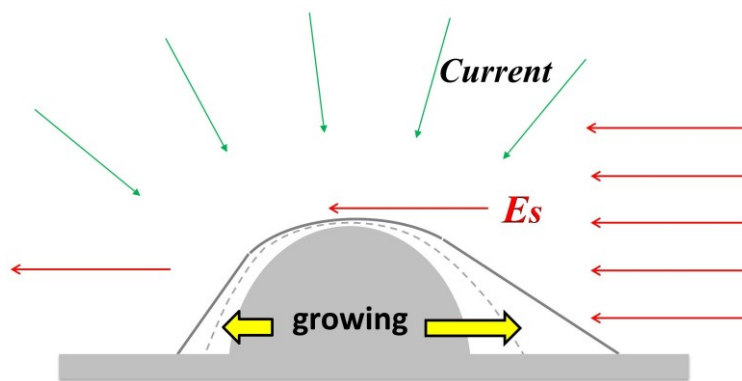


Figure 5-7 AFM images of the detailed features of the nickel deposit surfaces in different conditions.

The occurrence of the outstanding results that the coating surface turned rougher at  $f=1500$  and 3000rpm is consistent with the electrochemical characterization result shown in Fig. 5-5, the reason is still unclear at present. When the spinning frequency  $f$  was at 1000, 2000 and 2500rpm, the nickel deposit turned increasingly smoother, indicating the leveling effect of the induced electric field. To rationalize this electric field effect, the induced electric field is resolved into two components:  $E_n$  and  $E_s$ , which are normal and parallel to the electrode surface, respectively. Because  $E_n$  drives the nickel ions to and from the electrode surface periodically, its influence on the coating morphology can be neglected. The effect of  $E_s$  is illustrated in Fig. 5-8. Suppose there is a semi-spherical nodule on the coating surface that is exposed to  $E_s$  (Fig. 5-8(a)). The nickel ions are driven by the electric field,  $E_s$ , to move towards the side of the nodule facing the electric field (the front surface). The top and the other side of the nodule (the rear surface), however, are exposed to an electrolyte with lower nickel ion concentration because the nickel ions are propelled by the  $E_s$  to pass by the top surface or to migrate away from the rear surface. As a result, the deposition on the front surface is facilitated, while the top and the rear surface it is suppressed (Fig. 5-8(b)). When the magnets spin to the opposite direction, the rear surface becomes the front surface where fast growth is favoured. As the magnet spins around equally in all directions, the circumference of the nodule is leveled by  $E_s$ .



(a)



(b)

Figure 5-8 Illustration of the mechanism of the induced electric field leveling a grain: (a) different influences on various parts of the grain; and (b) the resultant growth.

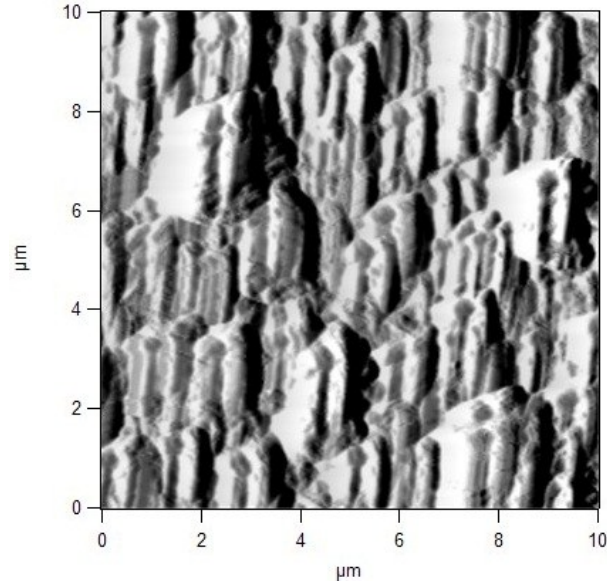


Figure 5-9 AFM image of Ni coating surface under the magnetic field that is spinning at 3000rpm.

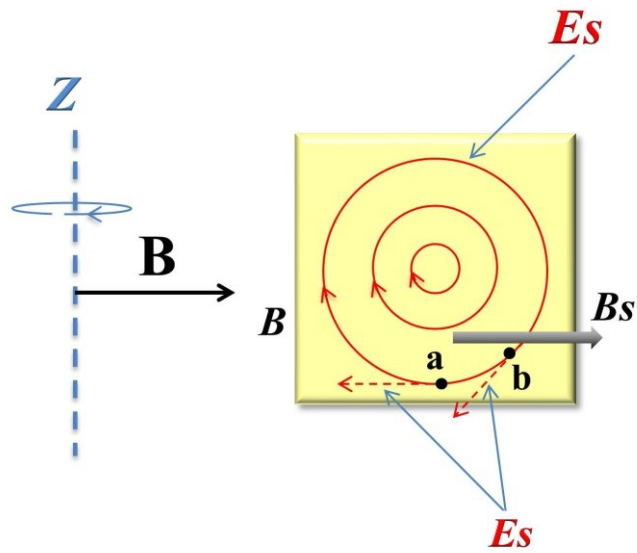


Figure 5-10 Schematic presentation of the surface components of the magnetic field and the induced electric field.

In addition to the levelling effect discussed above, the electric field may have other influences on the coating morphology. As seen in the AFM images shown in Fig. 5-9, at  $f=3000$ rpm, some elongated grains are observed at on the sample surface, which are similar to those reported in the deposition of Fe or its alloys in the parallel magnetic field<sup>20-22</sup>. This kind of morphological feature was found only in AFM images obtained at a scanning range of  $10 \times 10 \mu\text{m}$  and under  $f=3000$  rpm. Two possible mechanisms are put forward below to explain the observations.

First, according to the model illustrated in Fig. 4-8(b) of Section 4.3.2.1, elongated grains in electrodeposition can be formed when the fluid streams in the electrolyte are modulated to align along the direction of the parallel external magnetic field. In the situation of spinning magnets, as depicted in Fig. 5-10, if the component of the magnetic field parallel to the cathode surface is  $B_s$ , the angle between  $B_s$  and  $E_s$  varies across the electrode surface, and at some spots (e.g., points a and b),  $B_s$  is nearly parallel to  $E_s$  (Point a) or has a high component along  $E_s$  (e.g. Point b). Under the circumstances, an elongated grain can be generated under the interaction of  $B_s$  if  $E_s$  is able to modulate the fluid streams in the electrolyte along its direction.

To determine whether  $E_s$  is strong enough to change the convection profile in the bath, the body force generated by  $E_s$  is estimated. According to electromagnetism<sup>23</sup>,  $E_s$  can be derived as

$$E_s = 0.5 r \omega B \cos \vartheta \quad (5-2)$$

Where  $\omega$  is the angular speed of the rotating magnetic field,  $r$  is the distance to the center of the magnetic field region, and  $\vartheta$  is interception angle of the induced electric field and the cathode surface.

The body force of  $E_s$  on the nickel ions,  $F_{ES}$ , is

$$F_{ES} = \frac{cFr\omega B \cos \vartheta}{\varepsilon} \quad (5-3)$$

Where  $c$  is the concentration of the electrolyte,  $F$  is the Faraday constant, and  $\varepsilon$  is the permittivity of water.

To estimate  $F_{ES}$ ,  $c = 0.05$  mol/liter or  $50$  mol/m<sup>3</sup> in this research,  $r$  is taken as 1 mm due to the size of the sample,  $\vartheta$  is set to be 45°, and  $\varepsilon$  equals  $80$ <sup>24</sup>.  $F_{ES}$  is then calculated using Equation (5-3) to be  $2.4 \times 10^3$  N/m<sup>3</sup> for  $f = 3000$  rpm, which is on the same order of magnitude as the natural convection driving force ( $10^3$  N/m<sup>3</sup>) calculated by Hinds *et. al.*<sup>25</sup> The above estimation suggests that  $E_s$  is strong enough to change the natural convection flow to its direction at  $f = 3000$  rpm, making the formation of the elongated grains possible.

Second, around the middle line of the eddy electric field where  $E_s$  is always parallel to one direction (the direction of the axis of the magnets rotation), as shown in Fig. 5-4(a),  $E_s$  may also contribute to the formation of the elongated grains by directly accelerating the lateral growth of the nodules.

The reason for the result that the elongated grains was only found in the coating obtained at 3000rpm is that both the magnetic field and induced electric field have leveling effect and may merge the elongated grains. As seen in Fig. 5-6 and Table 5-1, at 3000rpm, the coating's surface roughness increased to be higher than that for  $f = 1000, 2000$  and  $2500$  rpm, indicating

the leveling ability of the magnetic field and induced electric field declined for some unknown reason. The reduction of the magnetic and electric field's leveling effect made the occurrence of the elongated grains possible.

The combined effects of the magnetic field and the induced electric field in the alternative magnetic field experiment discussed above may have some potential applications. First, while the magnetic field can still take effect in leveling the deposit, the addition of the induced electric field further enhances the coating surface finish. If the magnets can be stronger and spinning at higher rate than in this investigation, smoother films are expected. Second, the deposit's morphology may be tailored in alternative magnetic field. For example, if the magnetic field can be fixed without rotation and only changes its magnitude periodically (using AC electromagnet), either parallel or perpendicular to the electrode,  $E_s$  will be as depicted in Fig. 5-4(a) or (c) and be stable. Then the elongated grains may probably be aligned in straight lines or concentric circles.

### **5.3.4 Structural investigation by XRD**

Fig. 5-11 shows the results of X-ray diffraction analysis of nickel deposition under various experimental conditions. The values of the intensity of the diffraction have been re-scaled such that the intensity of (111) plane in each diagram is normalized to 100. The diffraction intensities of (200), (220) and (311) peaks in Fig. 5-11 after normalization are plotted as a function of magnets spinning rate, as given in Fig. 5-12.

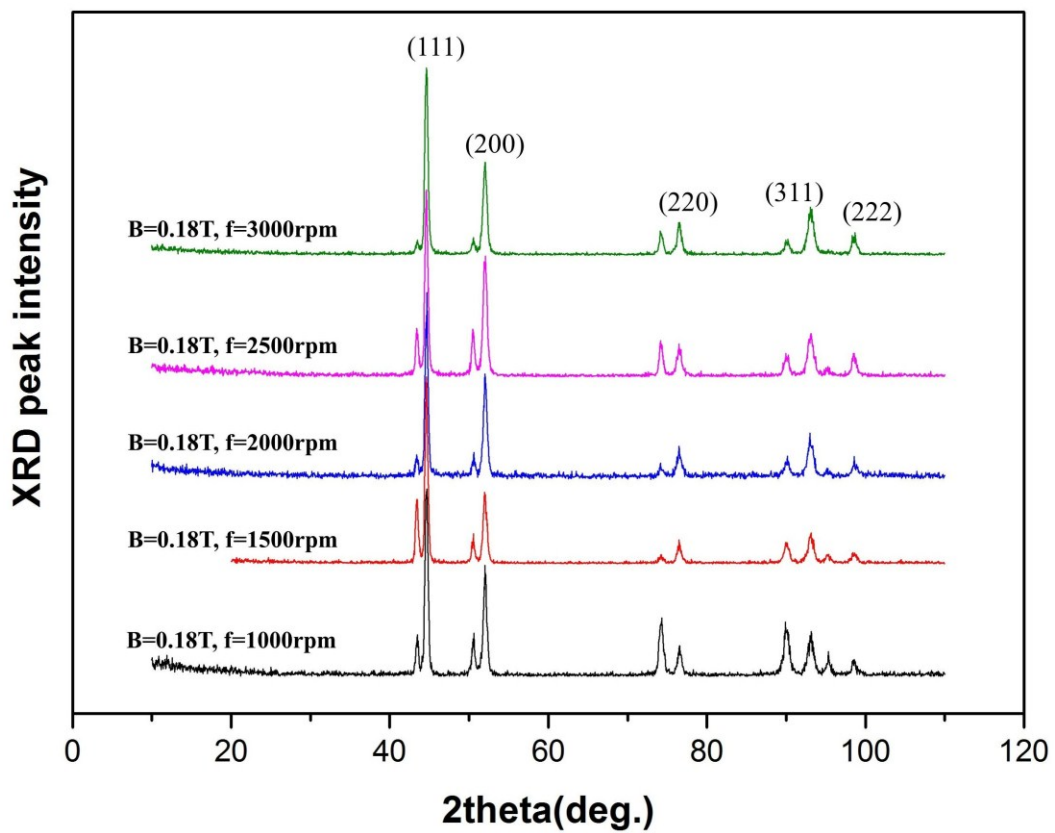


Figure 5-11 XRD spectra of nickel deposited in the nickel sulphate bath under different magnetic field situations. The intensity of (111) peak has been set to 100. All the unmarked peaks are from the Cu substrate.

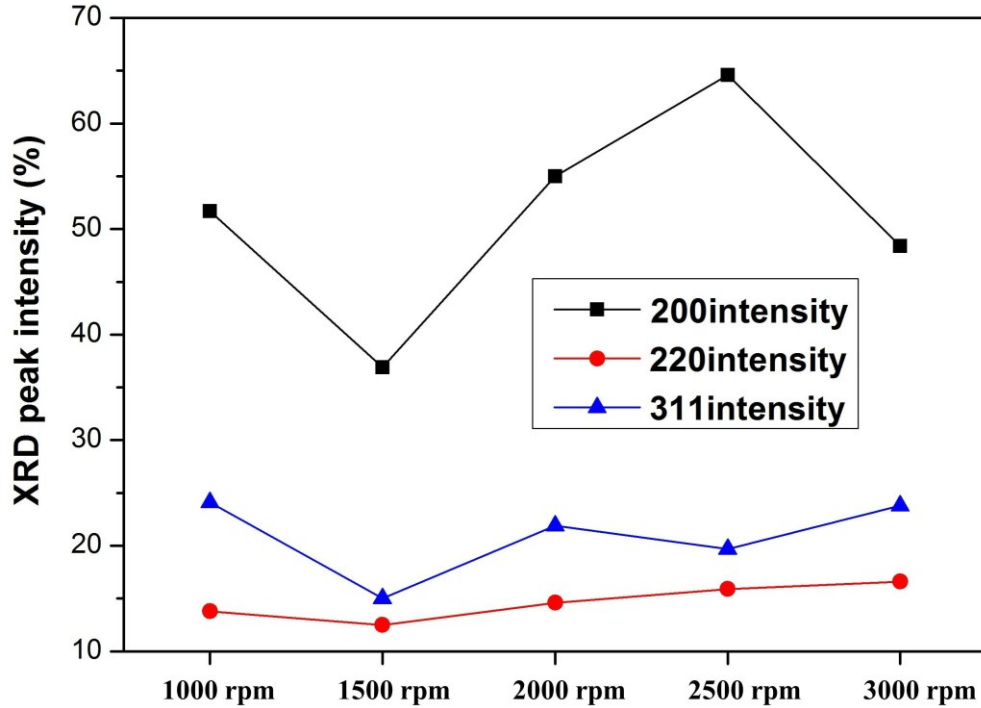


Figure 5-12 XRD peak intensities (proportion to 111 peak) of 200, 220 and 311 peaks obtained in the experiments.

The X-ray diffraction patterns in Fig. 5-11 clearly demonstrate that (111) plane is the predominant plane for all deposition conditions used in this investigation, which is in agreement with the previous result of other researchers that without magnetic field, the work required to form (111) plane in a face-centered cubic metal was the lowest and (111) plane therefore could develop preferentially<sup>26</sup>; and is also similar to the results observed by Brillas *et al.*<sup>27</sup> that (111) plane is dominant for nickel deposited in Watts bath under magnetic fields.

In XRD results in Fig. 5-12, (200) peak intensity shows the similar tendency as the chronopotentiometry curves and SEM images in Fig. 5-5 and Fig. 5-6, that for  $f=1000, 2000$

and 2500rpm, (200) peak intensity turned higher with increasing magnets' spinning rate; and at  $f=1500$  and 3000rpm, (200) peak intensity decreased.

The (311) diffraction plane/peak intensity in Fig. 5-12 fluctuated with the spinning rate increase. The (220) planes/peak intensity showed a weak dependence on the conditions of magnetic fields during the deposition of nickel.

Furthermore, from Fig. 5-9, it is clear that the elongated grains obtained at  $f=3000$  rpm exhibit the two-folded pyramid morphology which is similar to that displayed in Fig. 4-12 in Chapter 4 (in Chapter 4, the two facets of the pyramid were believed to be (111)), indicating that the leveling effect of the magnetic and the electric field decreased when the spinning rate is 3000rpm, which exposed the two-folded pyramids and promoted (111) plane's growth. This might be the reason for that the reduced (200) intensity was observed at  $f=3000$  rpm, as shown in Fig. 512.

In addition, the data in Table 5-1, Fig. 5-6 and Fig. 5-11 are very consistent in terms of morphological and (200) textural changes. This remarkable consistency between morphological and structural variations suggests that the texture formation and the morphological alteration during electro-deposition of Ni in rotating magnetic fields are closely related. In fact, such a consistency can be explained by means of the new model being proposed in Chapter 4, that is, the magnetic field promotes (200) growth in nickel deposition through leveling the pyramidal islands with two (111) facets. Under spinning magnets, there is an additional leveling effect from the induced electric field, which has made the (200) intensity of the sample obtained at  $f=2500$ rpm the highest in Fig. 5-12.

### **5.3.5 About the outstanding results at $f=1500$ and $3000$ rpm**

By comparing the results of this Chapter and Chapter 4, the electrochemical, morphological and structural characteristics were found to be very similar between the deposits made when  $f=1500$  rpm and  $B=0$ , and between those made when  $f=3000$  rpm and a parallel magnetic field was applied. These deposition experiments have been repeated several times and all of them have yielded consistent results.

The origin of these coincidences is unclear at present, even though the foregoing discussion that, at  $f=3000$  rpm, the occurrence of the elongated pyramids may possibly lead to the enhanced (111) texture. In our opinion, these abnormalities could be the result of the combined actions of the superimposed magnetic field, the induced electric field, the properties of the electrolyte, and the plating cell geometry as a boundary condition. Some theoretical calculations might be needed to clarify the interactions and influences of these factors on the migration and reduction of nickel ions in the electroplating process. This will be a subject of future investigations.

### **5.4 Conclusions**

1. The nickel electrodeposition has been carried out using a nickel sulfate bath under various magnets' spinning rates. Electrochemical studies using chronopotentiometry suggest that the spinning magnet allows a positive shift of the electrode potential during electro-deposition.
2. The spinning magnet fields can be adjusted to produce an additional leveling effect to the magnetic field, by the induced electric field on the coating surface. This provides a new

engineering approach to fabricate coatings with enhanced surface smoothness without the use of chemical additives.

3. The alternative magnetic field can induce an eddy electric field that has been identified to modify the morphological geometry of nickel deposition in two ways. One is to accelerate the lateral growth of the bumps on the coating film and reduce the surface roughness; the other is to yield elongated grains at certain spinning rate, which occurs in a way similar to the elongated grains' formation during the deposition of Fe or its alloys in parallel magnetic field.

4. An X-ray diffraction examination has revealed the modulating effect of the spinning magnets, on the nickel coatings' texture formation. There is a significant enhancement in (200) texture during nickel deposition performed at certain spinning rates of the magnetic fields. The modification of the nickel texture is believed to be caused by the levelling effect of both the magnetic field and the induced electric field, according to a new model proposed in Chapter 4.

5. The employment of the spinning magnets during electrodeposition provides a new approach to tailor the morphological and crystallographic properties of the deposits.

6. Abnormalities in morphology and texture were found when the magnetic field was rotated at speeds of 1500 and 3000rpm. Further research is required to rationalize these abnormal observations.

## 5.5 References

- 1 S. Molokov, R. Moreau, H.K. Moffatt (eds.), *Magnetohydrodynamics – Historical Evolution and Trends*, 391-407. 2007 Springer.
- 2 E. Tronel-Peyroz, A. Olivier, *Physico-Chemical Hydrodynamics* (1982), 3, 251-265.
- 3 O. Aaboubi, J. P. Chopart, J. Douglade, A. Olivier, C. Gabrielli and B. Tribollet, *J. Electrochem. Soc.*, Vol. 137, 6(1990) 1796-1804.
- 4 V. Ganesh, D. Vijayaraghavan, V. Lakshminarayanan, *Applied Surface Science* 240 (2005) 286-295.
- 5 A. Olivier, J.P. Chopart, J. Douglade, C. Gabrielli and B. Tribollet, *J. Electrochem. Soc.*, Vol. 227 (1987) 275-279.
- 6 I. Tabakovic, S. Riemer, M. Sun, V. A. Vasko and M. T. Kief, *J. Electrochem. Soc.*, Vol. 152 (12) 2005, C851-860.
- 7 A. Bund, S. Koehler, H. H. Kuehnlein, W. Plieth, *Electrochim. Acta* 49 (2003) 147.
- 8 O. Devos, A. Olivier, J. P. Chopart, O. Aaboubi, G. Maurin, *J. Electrochem. Soc.*, Vol. 145 (2) 1998, 401.
- 9 O. Devos, O. Aaboubi, J. P. Chopart, E. Merienne, A. Olivier, J. Amblard, *J. Electrochem. Soc.*, Vol. 145 (12) 1998, 4135.
- 10 I. Tabakovic, S. Riemer, V. Vas'ko, V. Sapozhnikov, M. Kief, *J. Electrochem. Soc.*, Vol.

- 150 (9) 2003, C635-640.
- 11 A. Krause, C. Hamann, M. Uhlemann, A. Gebert, L. Schultz, *Journal of Magnetism and Magnetic Materials* 290–291 (2005) 261–264.
- 12 R. Aogaki, *Magneto hydrodynamics* 37, 143–150 (2001).
- 13 S. Bodea, L. Vignon, R. Ballou, P. Molho, *Phys. Rev. Lett.* 83 (1999) 2612.
- 14 A. Chiba, K. Kitamura, T. Ogawa, *Surf. Coat. Technol.*, 27, 83 (1986).
- 15 D. Y. Li, J. A. Szpunar, *J. Matt. Sci.* 28 (1993) 5554-5559.
- 16 D. Y. Li, J. A. Szpunar, *Electrochim. Acta* 42 (1997) 37-45.
- 17 D. Y. Li, J. A. Szpunar, *Electrochim. Acta* 42 (1997) 47-60.
- 18 Sugiyama A, Morisake S, Mogi I, Aogaki R, *Electrochemistry* 68 (2000) 771-778.
- 19 J. D. Jackson, *Classical Electrodynamics*, Samizdat Press, 1999.
- 20 A. Ispas, H. Matsushima, W. Plieth, A. Bund, *Electrochim. Acta* 52 (2007) 2785.
- 21 H. Matsushima, T. Nohira, and Y. Ito, *Electrochemical and Solid-State Letters*, 7 (8) C81-C83 (2004).
- 22 H. Matsushima, Y. Fukunaka, Y. Ito, A. Bund, W. Plieth, *Journal of Electroanalytical Chemistry* 587 (2006) 93–98.
- 23 T. Becherrawy, *Electromagnetism*, ISTE Ltd 2012.
- 24 J. O. Bockris, *Modern Electrochemistry*, 2nd edition, Plenum Press, New York, 1998.
- 25 G. Hinds, J. M. D. Coey, M. E. G. Lyons, *Electrochemistry Communications* 3(2001)

215-218.

26 Rashkov. S., Stoichev. D. S., Tomov. L 1972. *Electrochim. Acta* 17: 1955.

27 E. Brillas, J. Rambla, J. Casado, *J. Appl. Electrochem.* 29 (1999) 1367.

**Chapter 6 Microhardness investigation of nickel electrodeposition in magnetic  
field**

## 6.1 Introduction

Hardness is one of the most important mechanical properties of metal deposit<sup>1</sup>. According to the theory of plastic deformation<sup>2</sup>, the hardness of a metallic material can be enhanced through grain size reduction, solid solution, strain and precipitate hardening. In electrodeposition, the hardness of the deposited layer can be affected by the operating conditions and electrolyte composition<sup>3-6</sup>, such as solution pH, current density, temperature, chloride content, surfactant, additives, coating thickness, and electroplating techniques such as pulse plating. For example, Bund and Thiemig<sup>4</sup> observed that the micro-hardness of pure nickel and nickel-Al<sub>2</sub>O<sub>3</sub> composite coatings decreased with increasing current density. Rezaei-Sameti *et al.*<sup>5</sup> reported that the addition of sodium saccharin and SDS into the solution caused the hardness of the Cr-WC nano composite coatings to increase. Nasirpouri *et al.*<sup>7</sup> compared the effect of pulse current (PC) plating, pulsed reverse current plating and direct current (DC) plating on the properties of nickel films and found that the former two techniques yielded coating films with finer grains and higher hardness.

Numerous efforts have been made to investigate the dependence of coating hardness on various operating conditions in electrodeposition and the underlining mechanisms. Apart from the “chemistry” dependent strengthening effects such as solid solution hardening and precipitate hardening, parameters of electrodeposition can be altered to obtain coatings with different grain sizes, surface morphology or microstructure, and texture<sup>4- 17</sup> (e.g., organic additives can significantly level the surface morphology or reduce the grain size). These physical and crystallographic variations can also cause significant strengthening effects. A brief introduction of these strengthening effects is given below.

**a. Grain size:** The grain size has been frequently reported to correlate with coating hardness<sup>7-10</sup>, which can be empirically expressed by the well-known Hall-Petch relation<sup>2</sup>:

$$H = H_0 + Kd^{-1/2} \quad (6-1)$$

Where  $H$  is the hardness,  $H_0$  and  $k$  are constants, and  $d$  is the grain size.

**b. Morphology or microstructure:** In 1962, Weil and Cook<sup>18</sup> investigated the morphology of the nickel deposit from a Watts bath and observed the structures that they referred to as colonies, which were defined as a series of fine grains surrounded by relatively deep crevices. This observation was later confirmed by Banovic *et al.*<sup>11</sup>. The formation of these crevices was suggested to have stemmed from the local absorption of foreign materials, e.g., sulphur and/or carbon containing ions, which hindered the deposition. For instance, Crossley *et al.*<sup>19</sup> studied the absorption of addition agents onto the growing nickel coating and found that the incorporated foreign ions blocked the emerging screw dislocations, and linked to the pyramidal growth of the deposit. Banovic *et al.*<sup>11</sup> also reported that these pyramids disappeared at a low current density owing to the incorporation of the foreign ions into the deposits. They went even further to identify the size of these surface structures or colonies by measuring the width of the structures which appeared as columnar grains in the cross section images, and found a Hall-Petch type relationship between the hardness of the coating and the columnar grain size. The strengthening of the coating samples was thus believed to be caused by the incorporation of the foreign ions that are able to refine the microstructure of the coatings.

**c. Texture:** According to the theory of plastic deformation<sup>2</sup>, a polycrystalline would exhibit higher resistance to plastic deformation than a single-crystal equivalent due to the geometrical constraints imposed by the surrounding grains. Therefore, even though the deformation behavior

of a single grain is highly anisotropic, the hardness of polycrystalline materials such as coating films does not demonstrate a strong dependence on crystal texture.

For highly anisotropic materials, e.g., zinc and CoW, coating textures were found to have an influence on the hardness<sup>8,15,16</sup>. Saber *et al.*<sup>8</sup> evaluated the micro-hardness of zinc deposit films and attributed the change in hardness to three possibilities: the effect of additives, which brought about sulfur content variation in the deposits; effect of grain size; and the effect of preferred crystallographic orientations/texture. The latter was explained in terms of the highly anisotropic deformation behavior of zinc<sup>20</sup>. However, for materials with fcc and bcc crystal structures, like nickel or iron, the impact of texture on hardness was observed to be negligible<sup>21,22</sup>. For instance, Yang *et al.*<sup>22</sup> reported that the preferred orientation had no effect on the hardness of pure nickel coating.

It has been found that superimposing the magnetic field in electrodeposition affects the coating properties<sup>23,24</sup>. Although considerable efforts have been devoted to the effect of magnetic field, most of the attention has been paid to the impact of the external magnetic field on morphology, structure and magnetic properties of the deposits. Very few results<sup>25,26</sup> have been reported concerning the effect of the magnetic field on the mechanical properties.

The present study evaluated the micro-hardness of the pure nickel deposit developed in the presence of both the static and alternative magnetic fields. The investigation was carried out by generating an alternative magnetic field using a pair of spinning permanent magnet groups. This setup makes it possible to periodically change the direction of the field.

## 6.2 Experimental

Nickel was electrodeposited galvanostatically by a 3-electrode system. The deposition experiments were conducted in the absence of the magnetic field, the static parallel and vertical magnetic field, and under the spinning magnets at rotating rates of 1000, 1500, 2000, 2500 and 3000rpm, respectively.

The electrodeposition experiment, including the experimental setup, electrolyte composition, deposition parameters and operation procedures, is the same as what was introduced in Chapter 5.

Surface characterization was conducted using JEOL (JSM-6301FXV) field emission scanning electron microscope (SEM) for morphological features, ZEISS (EVO –MA15) SEM with an energy dispersive x-ray spectroscopy (EDX) attachment for determining chemical composition, (MFP-3D, Asylum Research) atomic force microscope for measuring the surface roughness and revealing some detailed features of the coating surfaces. X-ray diffraction (XRD) measurements were carried out in Rigaku-UltimaIV X-ray diffractometer using Cu K $\alpha$  radiation with a wavelength of 1.54Å. The 2 $\theta$  value was from 10° to 110°.

The micro-hardness of the deposited nickel was measured on a BUEHLER IndentaMet 1100 Series Hardness tester under a loading of 50 grams for 15 s.

## 6.3 Results and discussion

### 6.3.1 Micro-hardness test result

Fig. 6-1 shows the result of the Vickers hardness measurement under a loading of 50 grams (HV50) of the nickel coatings obtained in this investigation.

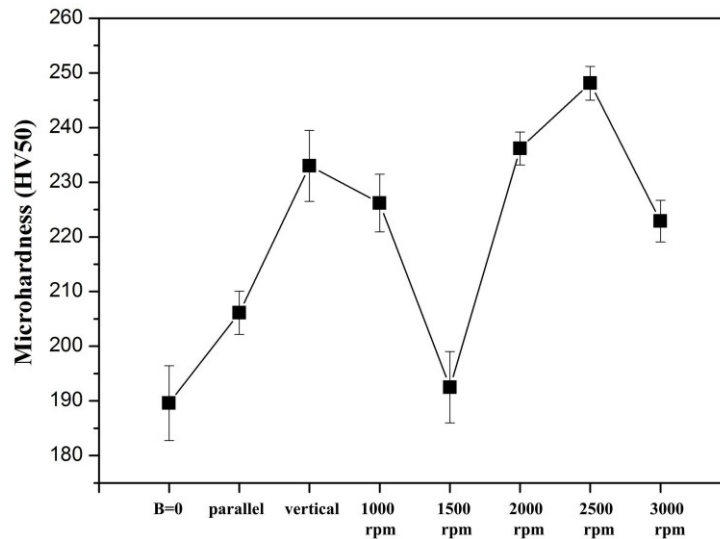


Figure 6-1 Vickers hardness of the deposited nickel in various magnetic field conditions.

The softest coating, with a HV50 value lower than 200, was observed when the magnetic field was not applied. The superimposition of the static parallel and vertical magnetic fields enhanced the hardness of the coating over 230. A further increase of the coating hardness was achieved under spinning magnets. At the spinning rate  $f = 2500$  rpm, the coating hardness reached the highest value, about 250HV. Again, abnormal hardness values appeared. At  $f = 1500$  rpm, the HV value was similar to that when  $B=0$ ; at  $f = 3000$  rpm, the hardness dropped.

### 6.3.2 Effect of grain size on micro-hardness

Based on the XRD analyses of the nickel coatings shown in Fig. 5-11 and 5-12 in Chapter 5, the grain size of the nickel coatings was calculated by Sherrer's equation as in Ref. 27-29.

$$\chi_s = \frac{0.9\lambda}{FWHM \cos \vartheta} \quad (6-2)$$

Where  $\chi_s$  denotes the grain size,  $\lambda$  the X-ray wavelength and  $\theta$  the diffraction angle. The calculating results are in Table 6-1. The grain size of a similar material was also estimated by X. Cui *et al.*<sup>30</sup> with TEM and the result is similar to this investigation.

For comparison, the grain size values and the corresponding micro-hardness data are shown in Fig. 6-2.

**Table 6-1 Grain size values of the coatings from different conditions\***

Conditions	B=0	B=0.18T, f=0, parallel	B=0.18T, f=0, vertical	B=0.18T, f=1000rpm	B=0.18T, f=1500rpm	B=0.18T, f=2000rpm	B=0.18T, f=2500rpm	B=0.18T, f=3000rpm
<b>Grain Size(nm)</b>	21.7	24.6	25.1	22.0	25.3	24.6	22.5	21.1

\*The grain size calculation was performed using data from (111) diffraction peaks.

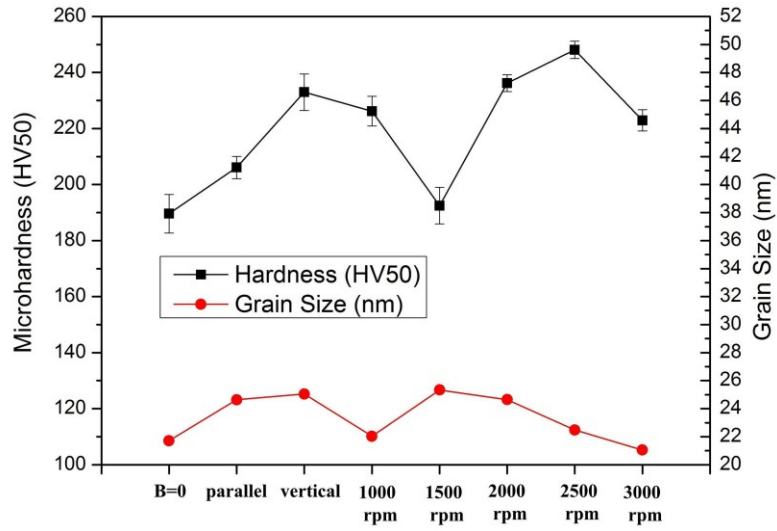


Figure 6-2 The variations of microhardness and grain size of the coating with experimental conditions.

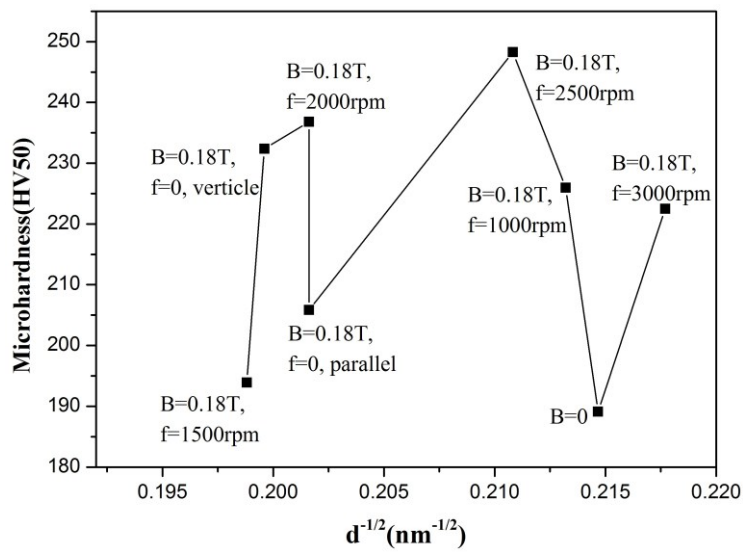


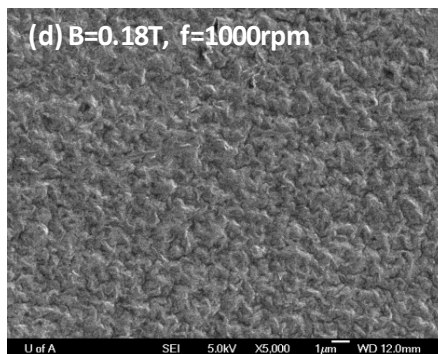
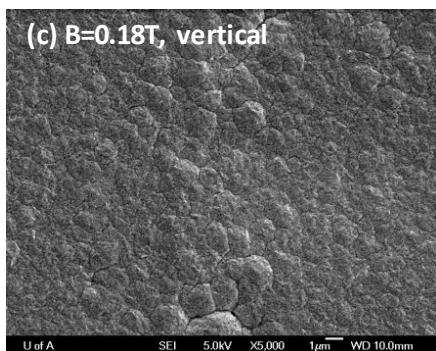
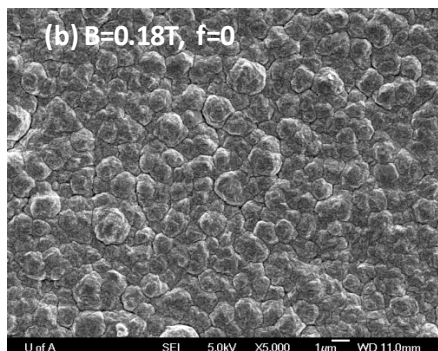
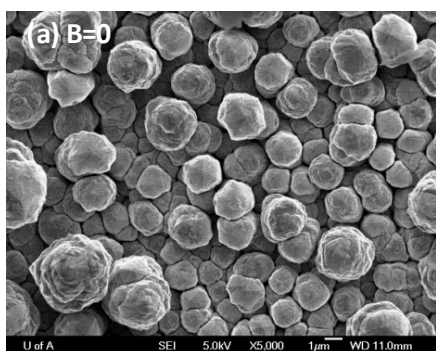
Figure 6-3 Variations of microhardness with  $d^{-1/2}$  (d is the grain size).

It is clearly seen from Fig. 6-2 that the grain size fluctuates within a very narrow range, from 21 nm to about 25 nm. In order to demonstrate the relationship between the micro-hardness and the grain size, the hardness is plotted as a function of  $d^{1/2}$  in accordance with Eq. 6-1, the Hall-Petch relation. As shown in Fig. 6-3, the micro-hardness is poorly related to  $1/\sqrt{d}$ , and there is no sign of the dependence of the hardness on grain size described by the Hall-Petch relation.

The rather minor variation of the grain size with the plating conditions can be explained by the chronopotentiometry data (Fig. 5-5) and the electric field induced by the spinning magnets, both of which are discussed in Chapter 5. First, in Fig. 5-5, the different cathodic potential measured at different deposition conditions leads to a varied reduction overpotentials that is responsible for the grain size variation in the coatings. Second, as pointed out in Chapter 5, the spinning magnets generate an eddy electric field that has a component along the electrode surface:  $E_s$ .  $E_s$  exerts an electric field force on the nickel ions in the solution and drives the ions to move along its direction. This can help their reduction and certainly increase the reduction driving force of these ions and reduce the grain size of the deposit. The combination of these two effects makes the coating grain size change slightly. For example, in the absence of the magnetic field, there is no induced electric field and  $E_s$  component to refine the grains of the coating. However, the electrode potential in this case is the lowest, which increases the reduction overpotential and reduces the gain size. Consequently, the corresponding grain size is still lower than the grain sizes of some plating conditions like the static magnetic field.

### 6.3.3 Effect of morphology on micro-hardness

The surface morphologies of the nickel coatings are displayed in Figs. 5-6 and 5-7. For convenience, these SEM and AFM images are shown again in Figs. 6-4 and 6-5.



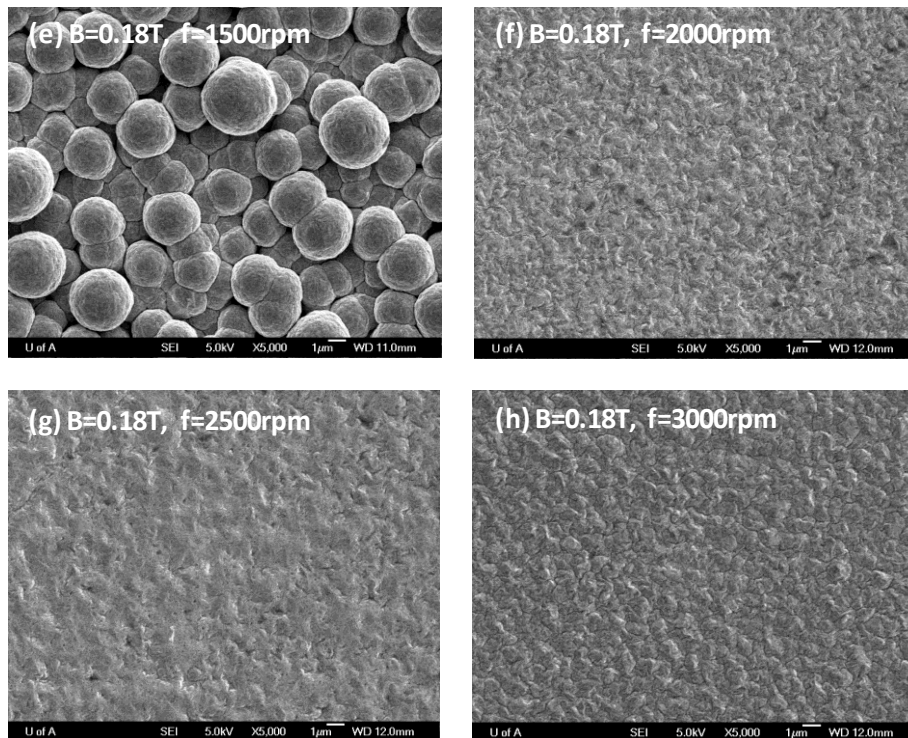
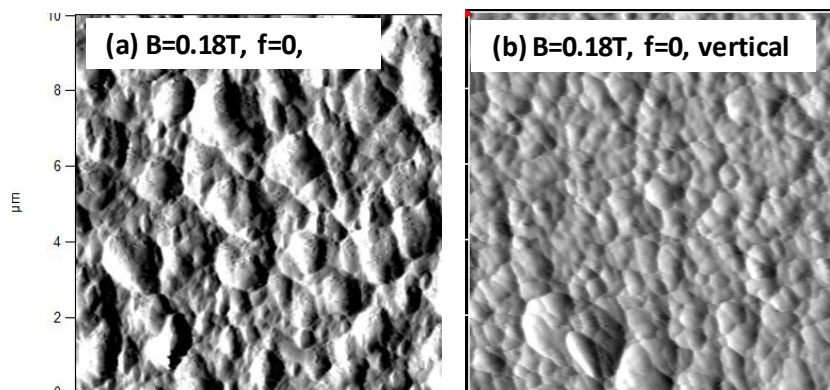


Figure 6-4 SEM images of deposited nickel morphology in the nickel sulphate bath under various magnetic field conditions: absence, static field and spinning magnet at different rates.



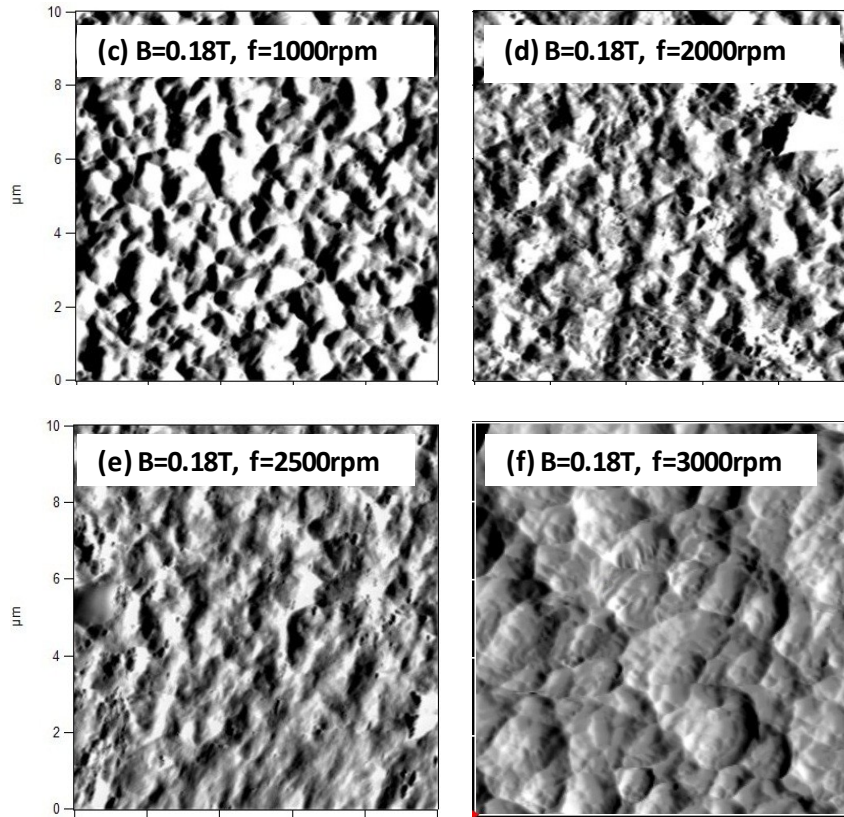


Figure 6-5 AFM images of the detailed features of the nickel deposit surfaces under different conditions. The scanning range is  $10 \times 10 \mu\text{m}$ . Due to the coarse surface of the coatings at  $B=0$  and  $B=0.18\text{T}$ ,  $f=1500\text{rpm}$ , no clear image is available for these two conditions.

It is clearly seen from Figs. 6-4 and 6-5 that the films deposited at  $B = 0$  and  $f = 1500\text{rpm}$  have the roughest surfaces, with stacked nodular particles that are widely separated. For other experimental conditions, the coating films are smoother with different surface roughness. The surface roughness of the coating films are measured and presented in Table 5-1.

Furthermore, from Fig. 6-4, similar to the observations in Ref. 11 and 18, the coating morphologies in this investigation exhibit colony-like features with colonies separated by crevices. The size of these colonies can be expressed by the surface roughness measurement results, the RMS values. Fig. 6.6 compares the hardness and RMS values to reveal their

correlation, which is clearly displayed, i.e., a rougher coating film corresponds to a lower hardness value.

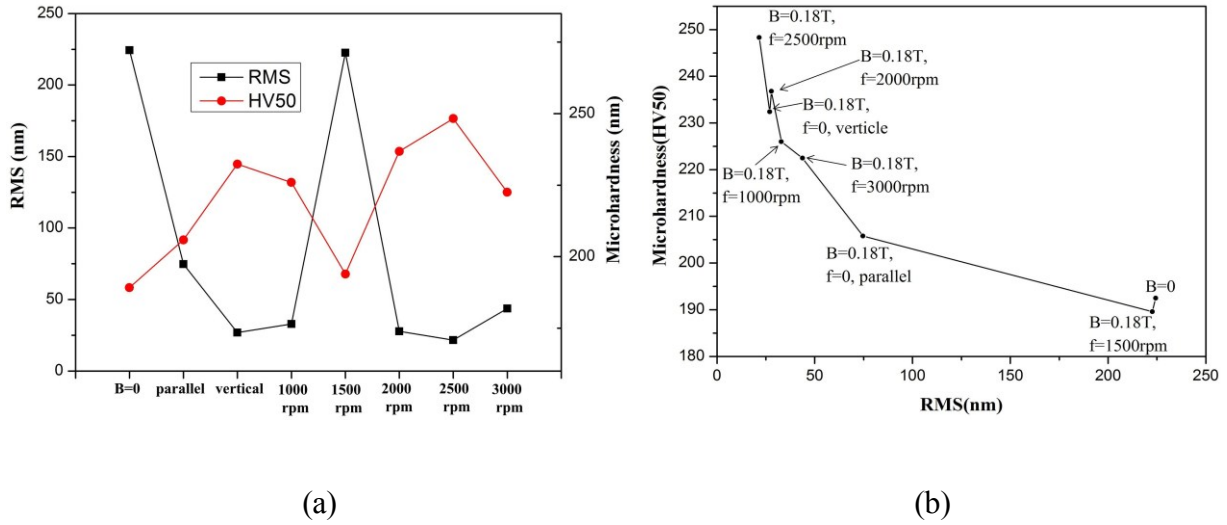


Figure 6-6 Schematic diagram of correlation of coating hardness with surface roughness measurement values. (a): RMS and hardness change with the operation conditions; (b) the trend of hardness varies with RMS.

### 6.3.4 Effect of crystal texture on micro-hardness

The preferred orientations of the deposits were determined with Muresan's method to calculate the texture coefficient using the fomula<sup>31</sup>:

$$T_c = \frac{I(hkl)}{\sum I(hkl)} \frac{\sum I_0(hkl)}{I_0(hkl)} \times 100 \quad (6-2)$$

Where  $I(hkl)$  is the peak intensity. The index 0 refers to the intensities of the standard nickel powder specimen<sup>32</sup>. The calculating result is presented in Fig. 6-7.

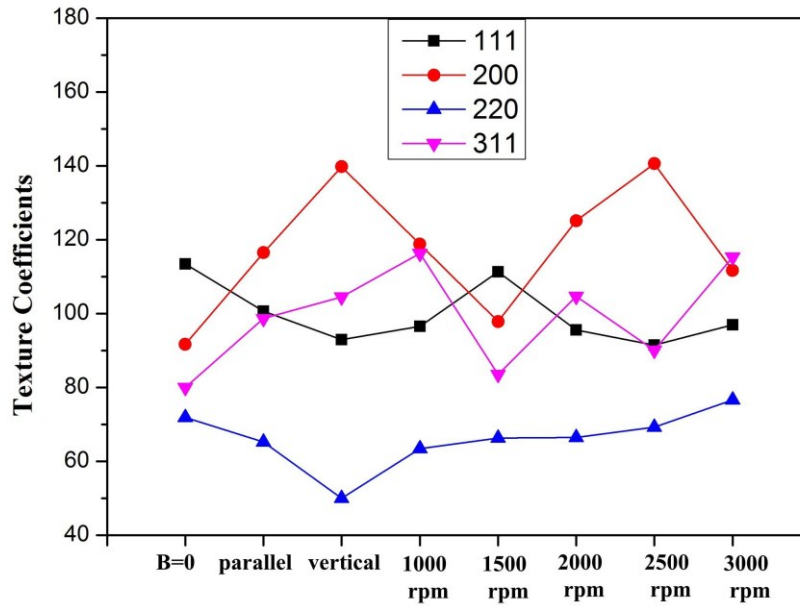


Figure 6-7 Texture coefficients of the nickel deposits from different magnetic field conditions.

Fig. 6-7 clearly shows that when  $B = 0$ , (111) is the preferred orientation of the nickel deposit; when the magnetic field is applied to the electrodeposition system, (200) becomes the preferred orientation except when the spinning rate is  $f = 1500$  and  $3000$  rpm. Therefore, the microhardness values of the deposits are compared with the (200) coefficients in Fig. 6.8, which indicates that on the whole the two variables have a positive correlation (except for the cases of static parallel and vertical magnetic fields).

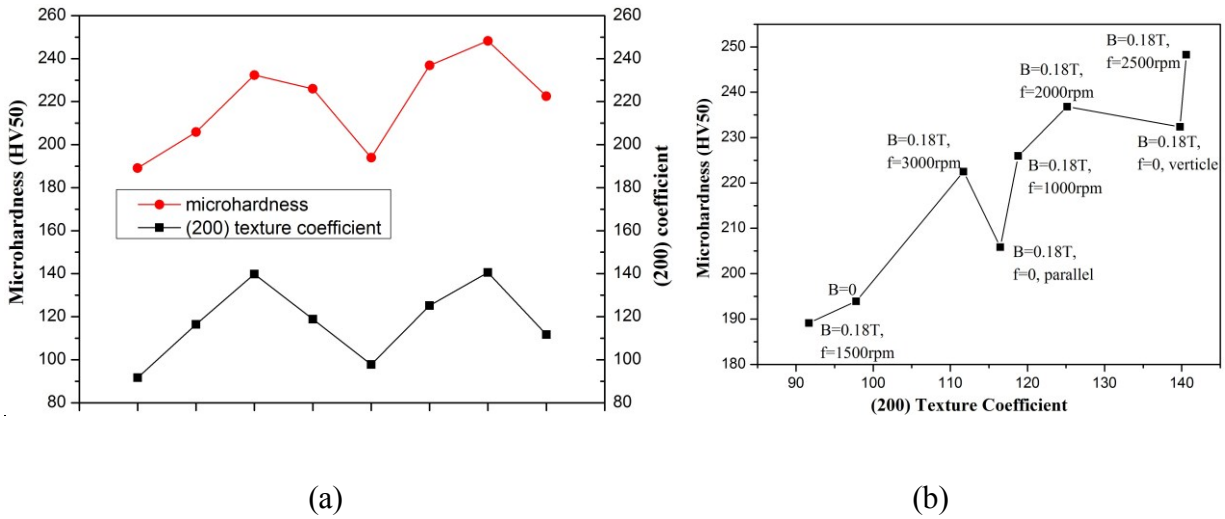


Figure 6-8 Comparison of microhardness and (200) texture coefficient (Tc 200). (a): hardness and Tc 200 change with the operation conditions; (b) the trend of hardness varies with Tc 200.

### 6.3.5 Identifying the dominant reason for coating strengthening

From the discussion above, it seems that the change of coating hardness could be correlated to both the surface roughness and the deposit texture. From the models established in Chapter 4, surface leveling from the magnetohydrodynamic (MHD) effect of the superimposed magnetic field leads to the (200) texture to increase. Therefore, in this investigation, the change of surface roughness and the (200) texture occur concurrently, making it difficult to determine the major influence between these two factors.

Theoretically, the fcc nickel has slip systems along  $\{111\}\langle 110\rangle$  directions<sup>2</sup>. Accordingly, a (111) textured single crystal would have a lower hardness than a (200) textured one. However, for a polycrystalline (especially nanostructured) sample, the multiple grain boundaries hinder the dislocation motion so that although a single grain may be favorably oriented with the applied stress for slipping, the deformation will not happen until the adjacent and less favorably

oriented grains are capable of slip. In this sense, the impact of the crystal texture of the nanostructured nickel deposit on the hardness should be negligible.

As mentioned in the introduction to this chapter, deposit hardness can be affected by the crystal texture<sup>8,15,16</sup>, and surface roughness<sup>15,16</sup>. In Ref. 8, the hardness of an hcp structured coating film was correlated to the preferred orientation. In that study, however, the grain size of the hcp structured sample was about 1  $\mu\text{m}$ , and such a coarse grain structure has far fewer grain boundaries than a nanocrystalline counterpart in terms of hindering the dislocation motions. In the case of materials with large grain sizes, the texture difference in the highly anisotropic hcp-structured materials could significantly alter the hardness.

Because the nickel deposit in this work has an fcc structure and is nanostructured, according to the above discussion, it is reasonable to believe that the crystal texture plays only a minor role in determining the coating hardness.

As a result, the morphology or the surface roughness is considered to be the major factor that affects the hardness of the nickel coating in this study. Similar to the effect of the grain boundaries, the boundaries of the colonies can serve as the obstacles to the dislocation motions, resulting in a higher hardness for the coatings that have a finer surface during plating.

To further confirm this conclusion, the micro-hardness data shown in Fig. 6-1 were re-plotted as a function of the surface roughness (RMS) data in Table 5-1 in a way similar to the Hall-Petch relation for grain boundary strengthening. The new plot is shown in Fig. 6-9, in which the micro-hardness is seen to increase linearly with the inverse square root of the the surface roughness.

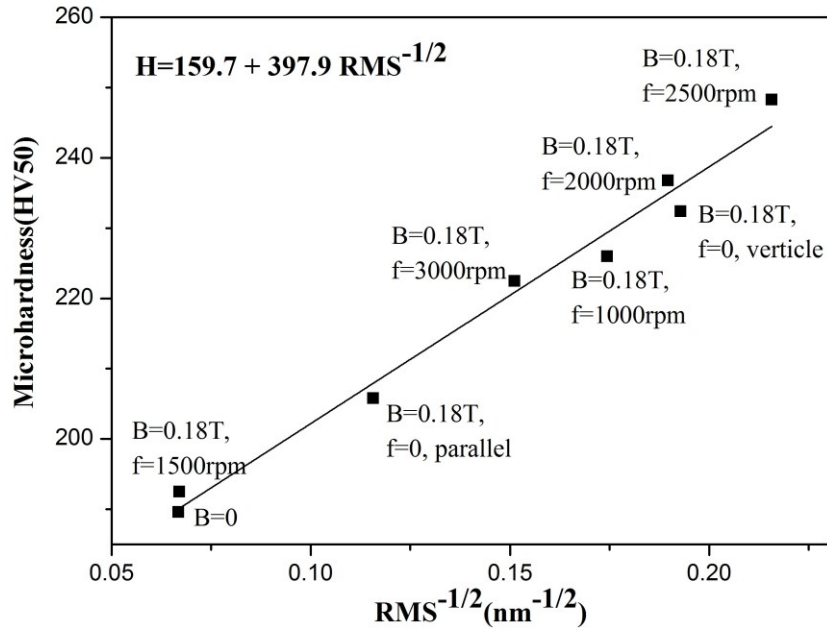


Figure 6-9 Schematic diagram of the relationship between microhardness and the inverse square root of RMS.

#### 6.4 Conclusions

The micro-hardness of the nickel deposits developed using nickel sulfate bath under various magnetic field conditions (absence, static field and spinning magnets) has been measured. Investigation has been performed to identify the dominant factor affecting the coating hardness.

The experimental results showed that the crystal grain size of the nickel coatings varied over a very narrow range. No significant relationship was found between the grain size and the micro-hardness.

The preferred orientation of the nickel deposit is believed to have minor influence on the hardness due to the fact that the samples are nanosturcured polycrystalline which have abundant grain boundaries to constrain the deformations in the individual grains.

The coating's roughness was identified to be a major factor in determining the micro-hardness. The micro-hardness can be well correlated to the surface roughness through a relationship similar to the Hall-Petch formula for the grain boundary strengthening.

## 6.5 References

- 1 Y. D. Gamburg, G. Zangari, Theory and Practice of Metal Electrodeposition, Springer, 2011.
- 2 W. D. Callister, Jr. D. G. Rethwisch, Materials Science and Engineering, 8th Edition, Wiley, 2010.
- 3 ASM hand book, Volume 5, Surface Engineering, ASM International, 1994.
- 4 A. Bund, D. Thiemig, Surface & Coatings Technology 201 (2007) 7092 – 7099.
- 5 M. Rezaei-Sameti, S. Nadali, A. Falahatpisheh, M. Rakhshi, Solid State Communications 159 (2013) 18–21.
- 6 E. A. Pavlatou and N. Spyrellis, Russian Journal of Electrochemistry, 2008, Vol. 44, No. 6, pp. 745–754.
- 7 F. Nasirpour, M.R. Sanaeian, A.S. Samardak, E.V. Sukovatitsina, A.V. Ognev, L.A. Chebotkevich, M.-G. Hosseini, M. Abdolmaleki, Applied Surface Science 292 (2014) 795–805.

- 8 Kh. Saber, C.C. Koch, P.S. Fedkiw, *Materials Science and Engineering A341* (2003) 174-181.
- 9 J. A.D. Jensen, P. O.A. Persson, K. Pantleon, M. Oden, L. Hultman, M. J. Somers, *Surface and Coatings Technology* 172 (2003) 79–89.
- 10 F. Su, C. Liu, Q. Zuo, P. Huang, M. Miao, *Materials Chemistry and Physics* 139 (2013) 663-673.
- 11 S. W. Banovic, K. Barmak, A. R. Marder, *Journal of Materials Science* 33 (1998) 639-645.
- 12 C.K. Chung, W.T. Chang, C.F. Chen, M.W. Liao, *Materials Letters* 65 (2011) 416–419.
- 13 D. E. Rusu, A. Ispas, A. Bund, C. Gheorghies, G. Carac, *J. Coat. Technol. Res.*, 9 (1) 87–95, 2012.
- 14 N. A. Badarulzaman, A. A. Mohamad, S. Puwadaria, Z. A. Ahmad, *J. Coat. Technol. Res.*, 7 (6) 815–820, 2010.
- 15 F. Su, C. Liu, P. Huang, *Journal of Alloys and Compounds* 557 (2013) 228–238.
- 16 K. O. Nayana and T. V. Venkatesha, *B. Mater. Sci.*, Vol. 37, No. 5, August 2014, pp. 1137-1146.
- 17 W. Shao, D. Nabb, N. Renevier, I. Sherrington, Y. Fu, and J. Luo, *Journal of the Electrochemical Society*, 159 (11) D671-D676 (2012).
- 18 R. Weil and H. C. Cook, *J. Electrochem. Soc.* 109 (1964) 295.
- 19 J. A. CROSSLEY, P. A. BROOK and J. W. CUTHBERTSON, *Electrochimica Acta*. 1966. Vol. 11, pp. 1153 to 1161.
- 20 R.W.K. Honeycombe, *The Plastic Deformation of Metals*, second ed., Edward Arnold, London, 1984.
- 21 T. Miura, K. Fujii, K. Fukuya, K. Takashima, *Journal of Nuclear Materials* 417 (2011)

- 984–987.
- 22 F. Yang, W. Tian, H. Nakano, H. Tsuji, S. Oue and H. Fukushima, *Materials Transactions*, Vol. 51, No. 5 (2010) pp. 948 to 956.
- 23 S. Molokov, R. Moreau, H.K. Moffatt (eds.), *Magnetohydrodynamics – Historical Evolution and Trends*, 391-407. 2007 Springer.
- 24 V. Ganesh, D. Vijayaraghavan, V. Lakshminarayanan, *Applied Surface Science* 240 (2005) 286-295.
- 25 D. Thiemig, C. Kubeil, C. P. Gräf, A. Bund, *Thin Solid Films* 517 (2009) 1636–1644.
- 26 M. Weinmann & A. Jung & H. Natter, *J Solid State Electrochem* (2013) 17:2721 – 2729.
- 27 A. Monshi, M. R. Foroughi, M. R. Monshi, *World Journal of Nano Science and Engineering*, 2012, 2, 154-160.
- 28 V. Ganesh, D. Vijayaraghavan, V. Lakshminarayanan, *Applied Surface Science* 240 (2005) 286-295.
- 29 C. Hammond, *The Basics of Crystallography and Diffraction*, Oxford University Press, Oxford, 1997.
- 30 X. Cui, W. Chen *J. Electrochem. Soc.*, 155 (9) K133-K139 (2008).
- 31 L. MURESAN, L. ONICIU, M. FROMENT, G. MAURIN, *Electrochim. Acta*, 37 (1992) 2249.
- 32 S. Tatge, N. Bur, *Stand. (U.S.), Circ. 539*, VI p13 (1953).

## **Chapter 7 Conclusions and Future Work Recommendations**

## **7.1 Conclusions**

The present study is aimed at developing new electroplating techniques on the basis of a better understanding of the electrodeposition process and mechanisms. The investigation is composed of two parts: 1) developing a set of methods to electroplate Ni/Cu alloy films with uniform composition, and at the same time achieving the highest concentration of Cu in Cu/Ni films with an apparent color close to Ni metal; and 2) Studying the underlying mechanisms of the magnetoelectrolysis process during nickel plating, in particular, the role of the magnetohydrodynamic (MHD) effect in morphology modification and texture formation. Some concluding remarks of this research are summarized below.

### **7.1.1 Electrodeposition of Ni/Cu alloy**

In this study, sodium citrate was selected as the complex agent in the codeposition not only for its cost effectiveness and environmental friendliness, but also for its buffering and leveling effects. The following challenges were encountered after this choice had been made and have been solved:

#### **(a) Solution stability**

The precipitation of the citric complex with low insolubility is a major problem of solution instability for a nickel-copper citrate bath. This problem has been solved in this research by carefully adjusting the bath formula, in particular, by controlling the concentrations of sodium citrate as well as metal sulfate ingredients; by maintaining a stable solution pH within a certain region; and by controlling the bath temperature at a suitable value to maximize the solubility of the citrate complex that may otherwise yield precipitate. The sustainability of the plating was thus ensured.

### (b) Composition control

A stable composition during plating is crucial for the coating quality. Our extensive investigations have found that keeping the bath pH stable is a prerequisite to the stabilization of coating composition. The approach that we developed to achieve a stable pH includes using two copper and nickel anodes and using numerical calculation to ensure that their areas are correctly selected. Through these efforts, the composition along the cross section of the sample was found to be uniform over a long period of plating.

### (c) Color adjustment

The apparent color of the Ni/Cu coating is also an important feature in practical use. For example, for coin application, it is desirable that the Ni/Cu coating with a high copper content exhibits the color of nickel. This investigation found that apart from the dominant reason of the alloy composition, the solution pH can also affect the color of the deposits. The underpinning mechanism has been identified that a different pH can change the residual stress in the deposit, which in turn may alter the electrons' band structures and the lattice vibration modes to affect the deposit's optical properties. The experimental result shows that increasing the bath pH tends to make the coating achieve a color closer to that of nickel.

## **7.1.2 Modeling on the mechanism of the morphological and structural change of magneto-electrolytic deposition**

Based on the results of electrochemical measurements, scanning electron microscope (SEM) examinations and X-ray diffraction (XRD) analyses, it has been determined that MHD convection in the bulk solution has a limited effect on the surface morphology and crystal texture

of the nickel deposits. However, the MHD effect in the fluid boundary layer can substantially modify the morphology and texture of the deposits.

Two new models were established to rationalize the MHD effect in the boundary layer under parallel and vertical magnetic fields, respectively.

It is hypothesized in the new models that the parallel magnetic field interacts with the convection flow to reduce the deposit surface roughness by accelerating the lateral growth of the bumps on the deposit surface. In the plating of soft magnetic material, it has been proved that magnetization on the deposit surface can exert a strong influence on the reduced adatoms and modulate the convection flow along the magnetic field direction. Consequently, elongated grains are predicted to occur.

On the other hand, the vertical magnetic field can cause both levelling and roughening of the coating surface. The levelling effect is produced by the stronger MHD stirring on the flat regions than on the undulations of the electrode surface, which levels these protrusions; the roughening effect occurs at the tip positions of the protrusions where the Lorentz force is stronger than on the side surface, which facilitates the upward growth and promotes the surface roughness. For materials other than the soft magnetic materials, the leveling effect is more prominent. Therefore, the obtained coating is smooth. For soft magnetic materials, the roughening effect is strengthened by the alignment of the convection flow from the surface magnetization, and by the field gradient effect resulting from the strong and non-uniform surface magnetization. The columnar morphologies are therefore formed.

The prediction of the occurrence of elongated grains in the parallel magnetic field and columnar grains in the vertical field remarkably agrees with the experimental results in literature, which have not so far been clearly explained.

Furthermore, the combination of the AFM observation and XRD characterization led to the finding that some of the nickel nuclei possessed a pyramidal shape with two elongated facets identified as Ni (111). A new model was established based on this new result to elucidate the texture formation during nickel film deposition in the magnetic field. That is, by leveling the pyramidal islands, the magnetic field promoted (200) texture growth, as experimentally observed in XRD tests.

### **7.1.3 Rotating magnetic field effects on nickel electrodeposition**

The theoretical analysis of the electrodeposition system under the spinning magnets condition shows that an eddy electric field is generated. The field exerts an electric force on the ions in the electrolyte. The deduction was confirmed by the results of a chronopotentiometry test, in which the electrode potential under the spinning magnets had an additional positive shift compared with the case of the static parallel magnetic field and the shift increased with higher spinning rates.

The induced electric field by spinning magnets can modify the deposition surface in two ways. First, it can promote the lateral growth of the bumps and enhance the surface smoothness; second, it can yield elongated grains when the spinning rate increases even though the deposit film is not composed of a soft magnetic material. The results of SEM and AFM characterization indicate that the smoothest deposit surface was achieved when the spinning rate was at 2500 rpm.

A significant increase in (200) texture was found under spinning magnets, which can be attributed to the levelling effect caused by the induced electric field.

At  $f=1500$  rpm, the effect of the spinning magnets on the electrolysis system was found to be similar to that in the absence of the magnetic field; and at  $f=3000$  rpm, the characteristics of the

deposit was were also found to resemble those observed under the static parallel magnetic field. Further fundamental study is required to explain these abnormal phenomena.

#### **7.1.4 Magnetic field effect on the microhardness of nickel deposit**

The experiment results demonstrated that the micro-hardness of the nickel deposit was enhanced in both the static magnetic field and in the spinning magnets, and the hardness reached its peak when the spinning rate was at 2500 rpm.

The grain size of the nickel deposit under various magnetic conditions was found to vary in a very narrow range. This insignificant change in grain size is believed to be caused by the counter-effect of the following two factors: the electrode potential and the induced electric field, which were found to affect the grain size in opposite ways.

The hardness variation under different plating conditions can be well related to the roughness of the deposits. The correlation was in a good agreement with the Hall-Petch relationship.

## **7.2 Future work recommendations**

### **7.2.1 Nickel-copper codeposition**

The Ni/Cu codeposition has been studied in the present investigation using a citrate bath, in which saccharin was employed as the only additive. An examination of other additives is necessary to further improve the coating quality. For example, it is well known that saccharin is normally used as a leveling agent<sup>1</sup> in electroplating to give a smooth coating surface. However, it cannot provide a shiny finish. To achieve this, additives such as brighteners have to be added into the bath, (e.g., 1,4-butyne 2-diol, thiourea, etc<sup>1</sup>). The addition of another additive might be

able to affect other properties of the coating, such as the color, because it can change the residual stress of the deposit, according to the conclusion in Chapter 3.

Also, as mentioned in Section 3.3.1.2, the current density in barrel plating experiments was less than  $2\text{mA}/\text{cm}^2$ , which is relatively low and may compromise the plating speed. Methods that can increase the plating current, thus accelerating the deposition process in the citrate bath, need to be developed.

### **7.2.2 magneto-electrolytic deposition**

In Chapter 4 and Chapter 5 of this thesis, the nickel deposition in the presence of the magnetic field has been investigated, and a relationship between the morphological and structural change of the coating film has been found. This new finding is only for the materials with an fcc structure. A corresponding relationship with other crystal structures of the materials (e.g., bcc, hcp) should be explored as well.

Employing stronger magnets that rotate at higher rates might yield coating films with new features, e.g., smoother surface, higher hardness, etc.

Adopting an alternative current electromagnet can better control the coating surface morphology by adjusting the position and orientation of the cathode in the magnetic field. This could generate, for special use, specific featured samples with fine grains aligned in concentric circles or straight lines.

In addition, the size of the sample and the electroplating cell can be changed to alter the boundary conditions in the magnetoelectrolysis system. The difference in nickel deposition results compared with those in chapter 5 might be useful to identify the reasons for the outstanding results obtained when magnets spinning at 1500 and 3000rpm.

### **7.3 References**

- 1 ASM hand book, Volume 5, *Surface Engineering*, ASM International, 1994.

## Bibliography

- 1 M. Schlesinger, M. Paunovic, *Modern Electroplating*, John Wiley & Sons, Inc. 2010.
- 2 R. Orinakova, A. Turonova, D. Kladekova, M. Galova and R. M. Smith, *Journal of Applied Electrochemistry* (2006) 36:957–972.
- 3 E.M. Oliveira, G.A. Finazzi, I.A. Carlos, *Surface & Coatings Technology* 200 (2006) 5978 – 5985.
- 4 M. Moharana, A. Mallik, *Electrochimica Acta* 98 (2013) 1–10.
- 5 L. M. Graham, S. Cho, S. K. Kim, M. N. and S. B. Lee, *Chem. Commun.*, 2014, 50, 527—529.
- 6 N. V. Sotskaya, L. V. Saprionova, and O. V. Dolgikh, *Protection of Metal and Physical Chemistry of Surfaces*, Vol. 50 No. 1 2014.
- 7 S. Hartwig and C. Klages, *Journal of The Electrochemical Society*, 161 (5) D243-D247 (2014).
- 8 E. Tóth-Kádár, L. Péter, T. Becsei, J. Tóth, L. Pogány, T. Tarnóczy, P. Kamasa, I. Bakonyi, G. Láng, Á. Cziráki, and W. Schwarzacher, *Journal of The Electrochemical Society*, 147, (9) 3311-3318 (2000).
- 9 I. Milošev and M. Metikos̃-Hukovic', *J. Appl. Electrochem.* 29 (1999) 393.
- 10 B. H. Prescott, *Trans. Inst. Met. Finish.*, 36, 93 (1959).
- 11 A. Brenner, *Electrodeposition of Alloys I* (Academic Press, New York, 1963).
- 12 J.R. Roos, J.P. Celis, C. Buelens and D. Goris, *Proc. Metall.* 3 (1984) 177.
- 13 K. Vu Quang, E. Chassaing, B. Le Viet, J. P. Celis, J. R. Roos, *Met. Finish*, 10, 25(1985).

- 14 C. Madore, Ph.D. Dissertation, Ecole Polytechnique Federale de Lausanne, Switzerland (1993).
- 15 J. Toth, L.F. Kiss, E. Toth-Kadar, A. Dinia, V. Pierron-Bohnes, I. Bakonyi, *Journal of Magnetism and Magnetic Materials* 198-199 (1999) 243-245.
- 16 E. Chassaing, K. VU Quang, *J. of App. Electrochem.* 17 (1987) 1267-1280.
- 17 R. Y. Ying, P. K. Ng, *J. Electrochem. Soc.* 135, 2964 (1988).
- 18 E. J. Podlaha, C. Bonhôte, and D. Landolt, *Electrochim. Acta*, 39, 2649 (1994).
- 19 S. Rode, C. Heninot, and M. Matlosz, *J. of Electrochem. Soc.*, 152 (4) C248-C254 (2005).
- 20 L. Bonou, Y. Massiani, J. Crousier, *British Corrosion Journal*, 29, 201 (1994).
- 21 L. P. Bicelli, B. B., C. Mele, L. D'Urzo, *Int. J. Electrochem. Sci.*, 3 (2008) 356 – 408.
- 22 S.K. Ghosh, A.K. Grover, G.K. Dey, M.K. Totlani, *Surface & Coatings Technology* 126 2000. 48-63.
- 23 X. Cui, W. Chen *J. Electrochem. Soc.*, 155 (9) K133-K139 (2008).
- 24 T. A. Green, A. E. Russell, S. Roy, *J. Electrochem. Soc.*, Vol. 145, No. 3, March 1998.
- 25 A. J. Bard, L. R. Faulkner, *Electrochemical Methods*, 2nd edition, p45.
- 26 H. D. Hine, W. B. Cooley, *Transactions of the American Electrochemical Society*, 61, 48 (1925).
- 27 P. Bradley, S. Roy, D. Landolt, *Journal of the Chemical Society, Faraday Transactions*, 92, 4015 (1996).
- 28 I. Mizushima, M. Chikazawa and T. Watanabe, *J. Electrochem. Soc.* 143 (1996) 1978.
- 29 R. B. P. Crawford, R. D. Snyder, U.S. Patent Number 1,750,092 (1930).

- 30 L. C. Melo, P. de Lima-Neto, A. N. Correia, DOI 10.1007/s10800-010-0251-2.
- 31 S. K. Pannikar, T. L. Char, *Journal of the Electrochemical Society, Japan*, 25, E121, (1957).
- 32 A. R. Despic, V. D. Jovic, S. Spaic, *Journal of the Electrochemical Society*, 136, 6 (1989).
- 33 M. Ishikawa, H. Enomoto, M. Matsuoaka, C. Iwakura, *Electrochimica Acta*, 40, 1663 (1995).
- 34 M. Pushpavanam, K. Balakrishnan, *Journal of Applied Electrochemistry*, 26, 1065 (1996).
- 35 S. Rode, C. Henninot, and M. Matlosz, *J. of Electrochem. Soc.*, 151 (6) C405-C411 (2004).
- 36 P. G. Daniele, G. Ostacoli, O. Zerbinati, S. Sammartano, and A. D. Robertis, *Trans. Met. Chem.*, 13, 87 (1988).
- 37 B. W. Parry and F. W. Dubois, *J. Am. Chem. Soc.*, 74, 3749 (1952).
- 38 D. Mastropaolo, D. A. Powers, J. A. Potenza, and H. J. Schugar, *Inorg. Chem.*, 15, 1444 (1976).
- 39 S. Roy, M. Matlosz, and P. Landolt, *This Journal*, 141, 1509 (1994).
- 40 K. Murase, T. Honda, T. Hirato, and Y. Awakura, *Metallurgical and Materials Transactions B*, 29B, DECEMBER 1998-1197.
- 41 T.Z. Fahidy, *J. Appl. Electrochem.* 13 (1983) 553.
- 42 T. Z. Fahidy, *Progress in Surface Science* 68 (2001) 155-188.
- 43 H. Matsushima, T. Nohira, I. Mogi, Y. Ito, *Surface and Coatings Technology* 179 (2004) 245–251.

- 44 S. Molokov, R. Moreau, H.K. Moffatt (eds.), *Magnetohydrodynamics – Historical Evolution and Trends*, 391-407. 2007 Springer.
- 45 M. Uhlemann, K. Tschulik, A. Gebert, G. Mutschke, J. Frohlich, A. Bund, X. Yang, and K. Eckert, *Eur. Phys. J. Special Topics* 220, 287–302 (2013).
- 46 G. Hinds, F. E. Spada, J. M. D. Coey, T. R. Ni Mhiochain, and M. E. G. Lyons, *J. Phys. Chem. B* 2001, 105, 9487-9502.
- 47 O. Devos, O. Aaboubi, J.P. Chopart, C. Gabrielli, B. Tribollet, *J. Phys. Chemistry A* 104, 1544 (2000).
- 48 V. Ganesh, D. Vijayaraghavan, V. Lakshminarayanan, *Applied Surface Science* 240 (2005) 286–295.
- 49 G. Hinds, J. M. D. Coey, M. E. G. Lyons, *Electrochemistry Communications* 3(2001) 215-218.
- 50 M. S. Tillack and N. B. Morley, *MAGNETOHYDRODYNAMICS*, McGraw Hill, 14th Edition, 1998.
- 51 D. T. J. Hurle, R. W. Series, in: D. T. J. Hurle (Ed.), *Handbook of Crystal Growth*, North Holland, Amsterdam, vol. 2A, 1994, Chapter 5.
- 52 O. Y. Gorobets, V. Y. Gorobets, D. O. Derecha, and O. M. Brukva, *J. Phys. Chem. C* 2008, 112, 3373 – 3375.
- 53 K. Tschulik, J. A. Koza, M. Uhlemann, A. Gebert, L. Schultz, *Electrochemistry Communications* 11 (2009) 2241–2244.
- 54 K. M. Grant, J. W. Hemmet, H. S. White, *Electrochem. Commun.* 1 (1999) 39.
- 55 Y. Tanimoto, H. Yano, S. Watanabe, A. Katsuki, W. Duan, M. Fujiwara, *Bull. Chem. Soc. Jpn.* 73 (2000) 867.

- 56 M. S. Tillack and N. B. Morley, *Magnetohydrodynamics*, McGraw Hill, 14th Edition, 1998.
- 57 S. Mohanta and T. Z. Fahidy, *Electrochim. Acta* 21 (1976) 25.
- 58 E. Tronel-Peyroz and A. Olivier, *Compt. Rendus Acad. Sci.* 278 (1974) 997.
- 59 E. Tronel-Payroz, Thesis Doctorat d'Etat, Rheims (1978).
- 60 E. Tronel-Payroz, A. Olivier, T. Z. Fahidy and D. Laforgue-Kantzer, *Electrochim. Acta* 25 (1980) 441.
- 61 A. Olivier, Thesis Doctorat d'Etat, Rheims (1979).
- 62 J. Lielmezs and H. Aleman, *Thermochim. Acta* 18 (1977) 315.
- 63 J. Lielmezs, *Techn. Apskats* 79 (1977) 2.
- 64 Idem, *Bioelectrochem. Bioenerg.* 5 (1978) 285.
- 65 O. Lioubashevski, E. Katz, I. Willner, *J. Phys. Chem. B* 108 (2004) 5778.
- 66 M. Uhlemann, A. Krause, J.P. Chopart, A. Gebert, *J. Electrochem. Soc.* 152 (2005) C817.
- 67 T. Z. Fahidy, *Electrochim. Acta* 1973, 18, 607.
- 68 R. Aogaki, K. Fueki, and T. Mukaibo, *Denki Kagaku*, 43, 509 (1975).
- 69 R. Aogaki, K. Fueki, and T. Mukaibo *Denki Kagaku*, 44, 89 (1976).
- 70 A. OLIVIER, J.P. CHOPART and J. DOUGLADE, *J. Electroanal. Chem.*, 217 (1987) 443-452.
- 71 O. Aaboubi, J. P. Chopart, J. Douglade, A. Olivier, C. Gabrielli and B. Tribollet *J. Electrochem. Soc.*, 137, 1796, 1990.
- 72 L. N, Gao *J Phys Chem B* (1999) 103:5832.
- 73 Lioubashevski O, Katz E, Willner I (2004) *J Phys Chem B* 108: 5778.
- 74 Uhlemann M, Krause A, Chopart JP, Gebert A (2005) *J Electro-chem Soc* 152:C817.
- 75 O. Aaboubi & J.-P. Chopart, *ECS Transactions*, 25 (32) 27-34 (2010).

- 76 O. Aaboubi, Jacques Douglade, *Journal of Electroanalytical Chemistry* 693 (2013) 42–50.
- 77 P. Fricoteaux, B. Jonvel, and J.-P. Chopart, *J. Phys. Chem. B* 2003, 107, 9459 – 9464.
- 78 S. Legeai, M. Chatelut, O. Vittori, J. Chopart, O. Aaboubi, *Electrochimica Acta* 50 (2004) 51–57.
- 79 J.-P. Chopart, O. Aaboubi, E. Merienne, A. Olivier, J. Amblard, *Energy Conversion and Management* 43 (2002) 365.
- 80 P. Fricoteaux, A. Olivier and R. Delmas, *J. Electrochem. Soc.* 139 (1992) 1096.
- 81 O. Devos, O. Aaboubi, J.-P. Chopart, E. Merienne, A. Olivier, and J. Amblard, *J. Electrochem. Soc.*, Vol. 145, No.12, 4135, 1998.
- 82 H. Matsushima, T. Nohira and Y. Ito, *Electrochemical and Solid-State Letters*, 7 (8) C81-C83 (2004).
- 83 A. Krause, C. Hamann, M. Uhlemann, A. Gebert, L. Schultz, *Journal of Magnetism and Magnetic Materials* 290–291 (2005) 261–264
- 84 J. A. Koza, F. K., M. Uhlemann, J. McCord, C. Mickel, A. Gebert, S. Baunack, L. Schultz, *Electrochimica Acta* 55 (2010) 819–831.
- 85 A. Chiba, T. Niimi, H. Kitayama and T. Ogawa, *Surf Coat. Tech.* 29 (1986) 347.
- 86 A. Chiba and T. Ogawa, *Chem. Abstr.* 108 (1988) 175888.
- 87 H. Matsushima, Y. Fukunaka, Y. Ito, A. Bund, W. Plieth, *Journal of Electroanalytical Chemistry* 587 (2006) 93-98.
- 88 J. Koza, M. Uhlemann, A. Gebert, L. Schultz, *J Solid State Electrochem* (2008) 12:181-192.
- 89 A. Ispas, H. Matsushima, W. Plieth, A. Bund, *Electrochimica Acta* 52 (2007) 2785-2795.
- 90 A. Bund, S. Koehler, H.H. Kuehnlein, W. Plieth, *Electrochimica Acta* 49 (2003) 147–152.
- 91 M. Paunovic, M. Schlesinger (Eds.), *Fundamentals of Electrochemical Deposition*, Wiley,

New York, 1998.

- 92 O. Devos, A. Olivier, J. P. Chopart, A. Aaboubi and G. Maurin, *J. Electrochem. Soc.*, Vol. 145 (2) 1998, 401.
- 93 I. Tabakovic, S. Riemer, V. Vas'ko, V. Sapozhnikov, and M. Kief, *Journal of The Electrochemical Society*, 150 (9) C635-C640 (2003).
- 94 A. Krause, M. Uhlemann, A. Gebert, L. Schultz, *Electrochimica Acta* 49 (2004) 4127–4134.
- 95 M. Uhlemann, A. Krause, J. P. Chopart, and A. Gebert, *Journal of The Electrochemical Society*, 152 12 C817-C826 2005.
- 96 K. Shinohara, R. Aogaki, *Electrochemistry* 67 (1999) 126.
- 97 S. Bodea, L. Vignon, R. Ballou, P. Molho, *Phys. Rev. Lett.* 83 (1999) 2612.
- 98 M. Yamaguchi, Y. Tamimoto, *Magneto-Science*, Kodansha Ltd. and Springer-Verlag Berlin Heidelberg 2006.
- 99 R. Aogaki, *Magnetohydrodynamics* 37, 143–150 (2001).
- 100 R. Aogaki, *Magnetohydrodynamics* 39, 453–460 (2003).
- 101 I. Mogi, R. Morimoto, R. Aogaki & K. Watanabe, *Scientific Reports* | 3 : 2574 | DOI: 10.1038/srep02574, 2013.
- 102 A. Sugiyama, M. Hashirideb, R. Morimotob, Y. Nagaib, R. Aogakic, *Electrochimica Acta* 49 (2004) 5115–5124.
- 103 H. Matsushima, A. Ispas, A. Bund, B. Bozzini, *Journal of Electroanalytical Chemistry* 615 (2008) 191–196.

- 104 B. D. Cullity, C. D. Graham, Introduction to Magnetic Materials, John Wiley & Sons, 2nd edition, 2009.
- 105 S. Chikazumi, Physics of Ferromagnetism, second edition, Clarendon Press, Oxford, 1997.
- 106 J. M. D. Coey, Magnetism and Magnetic Materials, Cambridge University Press, 2009.
- 107 L. Yang, J. Electrochem. Soc., 101, 456 (1954).
- 108 D. Y. Li, J. A. Szpunar, J. Matt. Sci. 28 (1993) 5554-5559.
- 109 N. A. Pangarov, J. Electroanal. Chem. 9 (1965) 70-85.
- 110 D. Y. Li and J. A. Szpunar, Electrochimica Acta, Vol. 42, No. 1, 37-45, pp. 1997.
- 111 G. C. Ye and D. N. Lee, Plating and Surface Finishing, A, 60 (1981).
- 112 A. K. N. Reddy, J. Electroanal. Chem. 6, 141 (1963).
- 113 J.L. WALTER and C. G. DUNN, Acta. Metall. 8 (1960) 497.
- 114 L. E. Murr, Interfacial Phenomena in Metals and Alloys, Addison-Wesley, 1975.
- 115 J. K. MACKENZIE, A. J. W. MOORE and J. F. NICHOLAS, J. Phys. Chem. Solids 23 (1962) 185.
- 116 D.Y.LI and J. A. SZPUNAR, Electrochimico Acta, Vol. 42, No. 1, 47-60, 1997.
- 117 N. J. Petch, Phil. Mag. 1, 331 (1956).
- 118 G. Okamoto, J. Horiuti and K. Hirota, Sci. Papers Inst. Company, New York (1977). Phys. Chem. Res. (Tokyo) 29, 223 (1936).
- 119 G. J. I. Newbury, D. E. Joy, D. C. Lyman, C. E. Echlin, P. Lifshin, E. Sawyer, L. Michael, J. R. Scanning electron microscopy and X-ray microanalysis, 3rd edition, (Springer, New York, 2007).
- 120 Cullity, B. D.; Stock, S. R. in Elements of X-ray diffraction, 3rd edition, (Prentice Hall, New Jersey, 2001).

- 121 B. B. He, Powder Diffraction 18 (2), June 2003.
- 122 B. B. He, U. Preckwinkel and K. L. Smith, JCPDS-International Centre for Diffraction Data 2000, Advances in X-ray Analysis, Vol.43.
- 123 MFP-3DTM Atomic Force Microscope Installation and Operation Manual from Asylum Research, Inc. 2003-2004.
- 124 T. Watanabe, Nano Plating - Microstructure Formation Theory of Plated Films and a Database of Plated Films, Elsevier, 1st Edition, 2004.
- 125 K. Murase, T. Honda, T. Hirato, and Y. Awakura, Metallurgical and Materials Transactions B, 29B, Dec. 1998—1197.
- 126 J. O. Bockris, Modern Electrochemistry, 2nd edition, Plenum Press, New York, 1998.
- 127 A. Monshi, M. R. Foroughi, M. R. Monshi, World Journal of Nano Science and Engineering, 2012, 2, 154-160.
- 128 M. Motoyama, Y. Fukunaka, T. Sakka, and Y. H. Ogata, Journal of the Electrochemical Society, 153 (7) C502-C508 (2006).
- 129 K.C. Chan, W.K. Chan, N.S. Qu, Journal of Materials Processing Technology 89-90 (1999) 447-450.
- 130 M. Alper, H. Kockar, M. Safak, M. C. Baykul, Journal of Alloys and Compounds 453 (2008) 15–19.
- 131 E. Pellicer, A. Varea, S. Pané, K.M. Sivaraman, B.J. Nelson, S. Suriñach, M.D. Baró, J. Sort, Surface & Coatings Technology 205 (2011) 5285–5293.

- 132 M. Allahkarami, J. C. Hanan, Powder Diffraction 29 (2), June 2014.
- 133 P. G. Sanders, J. A. Eastman and J. R. Weertman, Acta mater. Vol. 45. No. 10. 4019-4025. 1997.
- 134 K. S. Siow, A. A. O. Tay and P. Oruganti, Materials Science and Technology March 2004 Vol. 20, 285.
- 135 Y. Li, X. Huang, J. Yao, and X. Deng, Advanced Materials Research Vols. 189-193 (2011) pp 911-914.
- 136 S. R. Brankovic, B. Kagajwala, J. George, G. Majkic, G. Stafford, P. Ruchhoeft, Electrochimica Acta 83 (2012) 387–393.
- 137 Wei R, Plating, 57, 1231 (1970).
- 138 J. D. Patterson, B. C. Bailey, Solid-State Physics, Springer-Verlag, Berlin Heidelberg, 2007.
- 139 D.S. Martin, N.P. Blanchard, P. Weightman, Surface Science 532–535 (2003) 1–7.
- 140 A. I. Belyaeva, A. A. Galuza, A. A. Savchenko, and K. A. Slatin, Bulletin of the Russian Academy of Sciences. Physics, 2011, Vol. 75, No. 5, pp. 721–724.
- 141 M. F. Doerner and W. D. Nix, CRC Crit. Rev. Solid State Phys. Mater. Sci.14, 225 (1988).

- 142 Li Sun, Yan-Feng Chen, Lei He and Chuan-Zhen Ge, De-Sheng Ding, Tao Yu and Ming-Sheng Zhang, Nai-Ben Ming, PHYSICAL REVIEW B, VOLUME 55, NUMBER 18, 1997.
- 143 D. Chen, Y. Luo, L. Wang, H. Li, G. Xi, Y. Jiang, Z. Hao, C. Sun, and Y. Han, Journal of Applied Physics, 101, 053712 (2007).
- 144 I. Delgadillo, H. Gollisch and R. Feder, Solid State Communications, Vol. 88, No. 10, 789-794, 1993.
- 145 I. Yu. Sklyadneva, R. Heid, P. M. Echenique, K.-B. Bohnen, and E. V. Chulkov, PHYSICAL REVIEW B 85, 155115 (2012).
- 146 J. Koza, M. Uhlemann, A. Gebert, L. Schultz, J. Solid State Electrochem (2008) 12:181–192.
- 147 S. Bodea, L. Vignon, R. Ballou, P. Molho, Phys. Rev. Lett. 83 (1999) 2612.
- 148 J. A. Koza, F. Karnbach, M. Uhlemann, J. McCord, C. Mickel, A. Gebert, S. Baunack, L. Schultz, Electrochimica Acta 55 (2010) 819–831.
- 149 A. Chiba, K. Kitamura, T. Ogawa, Surf. Coat. Technol., 27, 83 (1986).
- 150 T. Watanabe, Nano Plating - Microstructure Formation Theory of Plated Films and a Database of Plated Films, Elsevier, 1st Edition, 2004.
- 151 Rashkov, S., Stoichev, D. S., Tomov, L 1972. Electrochim. Acta 17: 1955.
- 152 E. Brillas, J. Rambla, J. Casado, J. Appl. Electrochem. 29 (1999) 1367.

- 153 C. Cierpka, T. Weier, G. Gerbeth, M. Uhlemann, K. Eckert, *J Solid State Electrochem* (2007) 11:687–701.
- 154 Y. Nakayama, R. Bouche, *Introduction to Fluid Mechanics*, Butterworth-Heinemann, 2002.
- 155 Levich, V. G. *Physicochemical Hydrodynamics*; Prentice-Hall, Englewood Cliffs, NJ, 1962.
- 156 D. Jiles, *Introduction to magnetism and magnetic materials*, 2nd Edition, 1998.
- 157 *Magnetism and Magnetic Materials*, J. M. D. Coey, Cambridge University Press 2009.
- 158 J. Krug, P. Politi, T. Michely, *Physical Review B*, 61, No. 20 14037 (2000).
- 159 J. Tersoff, A. W. Denier van der Gon, and R. M. Tromp, *PHYSICAL REVIEW LETTERS* 72, No. 2, 266 (1994).
- 160 D. Edström, D.G. Sangiovanni, L. Hultman, V. Chirita, I. Petrov, J.E. Greene, *Thin Solid Films* 558 (2014) 37–46.
- 161 J. VIGNERON, A. BENAÏSSA,\* I. DERYCKE, A. WIAME, R. SPORKEN, *International Journal of Quantum Chemistry*, Vol. 70, 1093-1097 1998.
- 162 K. Kyuno and G. Ehrlich, *Physical Review B*, 81, No. 25 5592 (1998).
- 163 T. Treeratanaphitak, M. D. Pritzker, N. M. Abukhdeir, *Electrochimica Acta* 121 (2014) 407–414.
- 164 D. D Vvedensky, *J. Phys.: Condens. Matter* 16 (2004) R1537–R1576.
- 165 K. Tschulik \*, J. A. Koza, M. Uhlemann, A. Gebert, L. Schultz, *Electrochemistry*

Communications 11 (2009) 2241–2244

- 166 Y. Murata, V. Petrova, B. B. Kappes, A. Ebnoumasir, I. Petrov, Y Xie, C. V. Ciobanu, and S. Kodambaka, ACS Nano, VOL. 4. No. 11, 6509-6514, 2010.
- 167 A. Olivier, J.P. Chopart, J. Douglade, C. Gabrielli and B. Tribollet, J. Electrochem. Soc., Vol. 227 (1987) 275-279.
- 168 I. Tabakovic, S. Riemer, M. Sun, V. A.Vasko and M. T. Kief, J. Electrochem.Soc., Vol.152 (12) 2005, C851-860.
- 169 J. D. Jackson, Classical Electrodynamics, Samizdat Press, 1999.
- 170 T. Becherrawy, Electromagnetism, ISTE Ltd 2012.
- 171 J. O. Bockris, Modern Electrochemistry, 2nd edition, Plenum Press, New York, 1998.
- 172 Rashkov. S., Stoichev. D. S., Tomov. L 1972.Electrochim. Acta 17: 1955.
- 173 E. Brillas, J. Rambla, J. Casado, J. Appl. Electrochem. 29 (1999) 1367.
- 174 Y. D. Gamburg, G. Zangari, Theory and Practice of Metal Electrodeposition, Springer, 2011.
- 175 W. D. Callister, Jr. D. G. Rethwisch, Materials Science and Engineering, 8th Edition, Wiley, 2010.
- 176 ASM hand book, Volume 5, Surface Engineering, ASM International, 1994.
- 177 A. Bund, D. Thiemig, Surface & Coatings Technology 201 (2007) 7092 – 7099.
- 178 M. Rezaei-Sameti, S. Nadali, A. Falahatpisheh, M. Rakhshi, Solid State Communications 159 (2013) 18–21.
- 179 E. A. Pavlatou and N. Spyrellis, Russian Journal of Electrochemistry, 2008, Vol. 44, No. 6,

pp. 745–754.

- 180 F. Nasirpouri, M.R. Sanaeian, A.S. Samardak, E.V. Sukovatitsina, A.V. Ognev, L.A. Chebotkevich, M.-G. Hosseini, M. Abdolmaleki, *Applied Surface Science* 292 (2014) 795–805.
- 181 Kh. Saber, C.C. Koch, P.S. Fedkiw, *Materials Science and Engineering A341* (2003) 174–181.
- 182 J. A.D. Jensen, P. O.A. Persson, K. Pantleon, M. Oden, L. Hultman, M. J. Somers, *Surface and Coatings Technology* 172 (2003) 79–89.
- 183 F. Su, C. Liu, Q. Zuo, P. Huang, M. Miao, *Materials Chemistry and Physics* 139 (2013) 663–673.
- 184 S. W. Banovic, K. Barmak, A. R. Marder, *Journal of Materials Science* 33 (1998) 639–645.
- 185 C.K. Chung, W.T. Chang, C.F. Chen, M.W. Liao, *Materials Letters* 65 (2011) 416–419.
- 186 D. E. Rusu, A. Ispas, A. Bund, C. Gheorghies, G. Carac, *J. Coat. Technol. Res.*, 9 (1) 87–95, 2012.
- 187 N. A. Badarulzaman, A. A. Mohamad, S. Puwadaria, Z. A. Ahmad, *J. Coat. Technol. Res.*, 7 (6) 815–820, 2010.
- 188 F. Su, C. Liu, P. Huang, *Journal of Alloys and Compounds* 557 (2013) 228–238.
- 189 K. O. Nayana and T. V. Venkatesha, *B. Mater. Sci.*, Vol. 37, No. 5, August 2014, pp. 1137–1146.
- 190 W. Shao, D. Nabb, N. Renevier, I. Sherrington, Y. Fu, and J. Luo, *Journal of the Electrochemical Society*, 159 (11) D671–D676 (2012).
- 191 R. Weil and H. C. Cook, *J. Electrochem. Soc.* 109 (1964) 295.
- 192 J. A. CROSSLEY, P. A. BROOK and J. W. CUTHBERTSON, *Electrochimica Acta*. 1966.

Vol. 11, pp. 1153 to 1161.

- 193 R.W.K. Honeycombe, *The Plastic Deformation of Metals*, second ed., Edward Arnold, London, 1984.
- 194 T. Miura, K. Fujii, K. Fukuya, K. Takashima, *Journal of Nuclear Materials* 417 (2011) 984–987.
- 195 F. Yang, W. Tian, H. Nakano, H. Tsuji, S. Oue and H. Fukushima, *Materials Transactions*, Vol. 51, No. 5 (2010) pp. 948 to 956.
- 196 S. Molokov, R. Moreau, H.K. Moffatt (eds.), *Magnetohydrodynamics – Historical Evolution and Trends*, 391-407. 2007 Springer.
- 197 D. Thiemig, C. Kubeil, C. P. Gräf, A. Bund, *Thin Solid Films* 517 (2009) 1636–1644.
- 198 M. Weinmann & A. Jung & H. Natter, *J Solid State Electrochem* (2013) 17:2721 – 2729.
- 199 A. Monshi, M. R. Foroughi, M. R. Monshi, *World Journal of Nano Science and Engineering*, 2012, 2, 154-160.
- 200 C. Hammond, *The Basics of Crystallography and Diffraction*, Oxford University Press, Oxford, 1997.
- 201 L. MURESAN, L. ONICIU, M. FROMENT, G. MAURIN, *Electrochim. Acta*, 37 (1992) 2249.
- 202 S. Tatge, N. Bur, *Stand. (U.S.)*, Circ. 539, VI p13 (1953).

